STRUCTURE, DYNAMICS AND HEATING IN MAGNETIZED REGIONS OF SOLAR ATMOSPHERE

A THESIS
SUBMITTED FOR THE DEGREE OF

DOCTOR OF PHILOSOPHY

IN

THE FACULTY OF SCIENCE
MANGALORE UNIVERSITY

BY

G. VIGEESH

INDIAN INSTITUTE OF ASTROPHYSICS
BANGALORE - 560 034, INDIA

JANUARY 2010

To my parents...

At first I did adore a twinkling star,
But now I worship a celestial sun.

The Two Gentlemen of Verona
WILLIAM SHAKESPEARE

DECLARATION

I hereby declare that the matter contained in the thesis entitled **"Structure, dynamics and heating in magnetized regions of solar atmosphere"** is the result of investigations carried out by me at the Indian Institute of Astrophysics under the supervision of Prof. S. S. Hasan. This thesis has not been submitted for the award of any degree, diploma, associateship, fellowship etc. of any University or Institute.

Vigeesh G.
(Candidate)

Indian Institute of Astrophysics
Bangalore-560034, India

CERTIFICATE

This is to certify that the matter contained in the thesis entitled "**Structure, dynamics and heating in magnetized regions of solar atmosphere**" submitted to Mangalore University by **Mr. Vigeesh. G** for the award the degree of Doctor of Philosophy in the Faculty of Science, is based on the results of investigations carried out by him under my supervision and guidance, at the Indian Institute of Astrophysics. This thesis has not been submitted for the award of any degree, diploma, associateship, fellowship etc. of any University or Institute.

Prof. S. S. Hasan
(Supervisor)

Indian Institute of Astrophysics
Bangalore-560034, India

ACKNOWLEDGEMENTS

First and foremost, I would like to thank my advisor, Prof. Siraj Hasan, for his constant support and guidance, without which this thesis would not have been possible. More than anyone else, his encouragement and trust has been a continuous source of inspiration throughout my research.

I owe my deepest gratitude to Dr. Oskar Steiner for giving me a chance to work with him. His childish curiosity and scientific perfectionism has been my driving force. There is no one else with whom I have been so much involved over the last few years. Oski, you have been a wonderful teacher and a great friend. Thank you for entertaining all my silly questions.

I am especially grateful to Dipuda and Rajaguru for their valuable advice and suggestions and for being extremely approachable. My sincere thanks also goes to the faculties at the Indian Institute of Astrophysics, for making me a part of their fraternity. I would also like to thank the faculties at Kiepenheuer-Institut, especially: Dr. Rolf Schlichenmaier, Dr. Reiner Hammer, Dr. Peter Caligari and others for their help and advice.

This work was partly carried out at the Kiepenheuer-Institut für Sonnenphysik (KIS) under the supervision of Dr. Oskar Steiner. I would like to thank the Director of KIS, Prof. Oskar von der Lühe, for supporting me and providing all the facilities I needed during my stay. I gratefully acknowledge the support provided by the Indian Department of Science & Technology (DST) through grant No. DST/INT/DAAD/P146/2006 and the German Academic Exchange Service (DAAD) through grant No. D/05/57687 under the DST-DAAD Project based Personnel Exchange Programme (PPP).

I would like to express my sincere thanks to Mr. Rajan, Ms. Pramila and Ms. Malini for giving me special privileges in Director's office and taking good care of me. I also wish to thank Dr. Baba Verghese and IIA's computer personnels, for their cooperation and support regarding all computer related problems. I also thank Dr. Vagiswari and Dr. Christina Birdie and all the library, administrative, technical and non-technical staff for the help they have given me from time to time.

I am indebted to Dr. Balakrishna and Dr. Dharmaprakash, Chairman of Physics Department and Ms. Soni and Ms. Anita of the administrative section of Mangalore University, for being extremely cooperative in all the formalities related to my PhD.

I thank all my juniors and seniors for the unique and lively environment they provided at Bhaskara. I deliberately avoid mentioning their names in the fear of missing out someone or the other. I also like to thank Morten Franz, Lars Krieger and Reza Rezaei for all the help they provided during my stay in Freiburg.

To the most valuable ones: Blesson, Bharat, Malay, Nagaraju, Ramya, Sreeja, Uday. Thank you for always being there for me. I terribly missed you when you were not around. I also thank my brother and friend, Nimeesh, for his love and support.

I take this occasion to thank all my teachers from whom I have borrowed the building blocks of my knowledge.

I wish to express my thanks to my loving father, mother and my sweet sister, Athira, for their belief in me, for their love and encouragement throughout my life, for eagerly waiting for my arrival every time I left home.

Finally, to my dearest Bhagya - you have been in my every thought.

TABLE OF CONTENTS

ABSTRACT

The solar variability at UV and EUV wavelengths is dominated by emissions from the "magnetic networks". These network elements are thought to be heated by dissipation of magneto-hydrodynamic (MHD) waves, but the MHD processes involved in wave generation, propagation and dissipation are only poorly understood. As part of this thesis work, we carried out an investigation of MHD wave dynamics in magnetic network elements using numerical simulations. The work is performed in the context of a model of magnetic network elements as a collection of smaller flux tubes that merge at some height in the chromosphere. Most small-scale magnetic flux concentrations are visible as bright objects with a magnetic field strength in the order of kilogauss, with a typical size of 100 km and a field that is largely vertically oriented. We have carried out a number of numerical simulations of wave propagation in a two dimensional gravitationally stratified atmosphere consisting of individual magnetic flux concentrations. We have studied MHD wave propagation in these structures in order to understand mode coupling and to estimate the energy transported by these waves. These simulations show that the nature of the modes excited depends on the value of plasma β (the ratio of gas to magnetic pressure) of the region where the excitation takes place. Mode conversions and transmissions occur in the region where $\beta = 1$ and energy is exchanged between various MHD modes. From a rough estimate of the acoustic energy flux generated by such impulsive transverse motions, we conclude that this flux would hardly balance the chromospheric energy requirements in the network. We have also explored the feasibility of developing diagnostic tools for the helioseismic exploration of such atmospheres using numerical simulations. In summary, this thesis aims at contributing to a better understanding of the dynamics of the magnetic network in the solar atmosphere, which has wider implications in the study of solar and stellar activity.

LIST OF FIGURES

LIST OF MOVIES

LIST OF TABLES

LIST OF PUBLICATIONS

Vigeesh, G.; Steiner, O.; Hasan, S. S., *Stokes diagnostics of simulations of wave propagation in the magnetic network on the Sun*, in preparation

Vigeesh, G.; Hasan, S. S. ; Steiner, O., *Wave propagation and energy transport in the magnetic network on the Sun*, 2009, Astronomy & Astrophysics, **508**, 951.

Vigeesh, G.; Hasan, S. S. ; Steiner, O., *Numerical Simulation of Wave Propagation in the Presence a Magnetic Flux Sheet*, 2008, 12th European Solar Physics Meeting.

Vigeesh, G.; Hasan, S. S. ; Steiner, O., *Numerical Simulations of Wave Propagation in Magnetic Network*, 2008, Proceedings of the IAU Symposium 257 on Universal Heliophysical Processes

Steiner, O.; Vigeesh, G.; Krieger, L.; Wedemeyer-Böhm, S.; Schaffenberger, W.; Freytag, B., 2007, *First local helioseismic experiments with CO5BOLD*, Astronomische Nachrichten, **328**, 323.

Hasan, S. S.; Vigeesh, G. and van Ballegooijen, A. A., *Wave Propagation in the Magnetic Network on the Sun*, 2006, Proceedings of the International Astronomical Union Symposium 233 on Solar Activity and its Magnetic Origin, **2**,116

CHAPTER 1

INTRODUCTION

1.1 THE SUN

Sun is our nearest star. It forms the central engine of the solar system. This huge ball of super-hot gas provides us with light and heat to survive in this universe and thereby making us capable to study it in return. It is the only star whose properties can be studied very closely and more accurately. Sun is a main-sequence star of spectral type G2V (a *yellow star*) composed mainly of Hydrogen (~71%), Helium (~27%) and other heavier elements. It is about 108 times the diameter of earth ($\sim 1.4 \times 10^6$ km) and weighs around 333,000 times earth ($\sim 1.99 \times 10^{30}$ kg). Like any other low mass main-sequence star, it generates energy by fusing hydrogen to form helium mainly via the proton-proton (p-p) chain reaction in its deep interior where the temperature is 1.5×10^7 K. Every second, 4.4×10^9 kg of mass is burned here in the dense core (1.48×10^5 kg m^{-3}) within a diameter of about 200 000 km. The energy liberated by this furnace escapes the sun into the outer space in the form of radiation. The Sun is about 4.6 billion years old and it is expected to live for at least another 4.6 billion years, slowly becoming a red giant and then will expel its outer layers, leaving a tiny white dwarf surrounded by a planetary nebula. In the following sections, I give a brief summary of the properties of the Sun, deep from the interior to the exterior.

1.2 SOLAR STRUCTURE

The Sun is a dense ball of plasma held together by gravity with a much rarer gaseous envelope that we shall refer to as the solar atmosphere. The invisible layer below the solar atmosphere that cannot be directly observed is called the solar interior. The phenomena occurring in the interior are directly connected to the properties that we observe in the visible layers. Nevertheless, it is important to separate these two parts of the Sun and study them individually. The interior and the atmosphere can be further separated into different layers depending on the conditions that exist in them, like the mode of energy transport. The different layers of the sun are schematically shown in Fig 1.1. The following section gives a brief outline of these layers of the Sun.

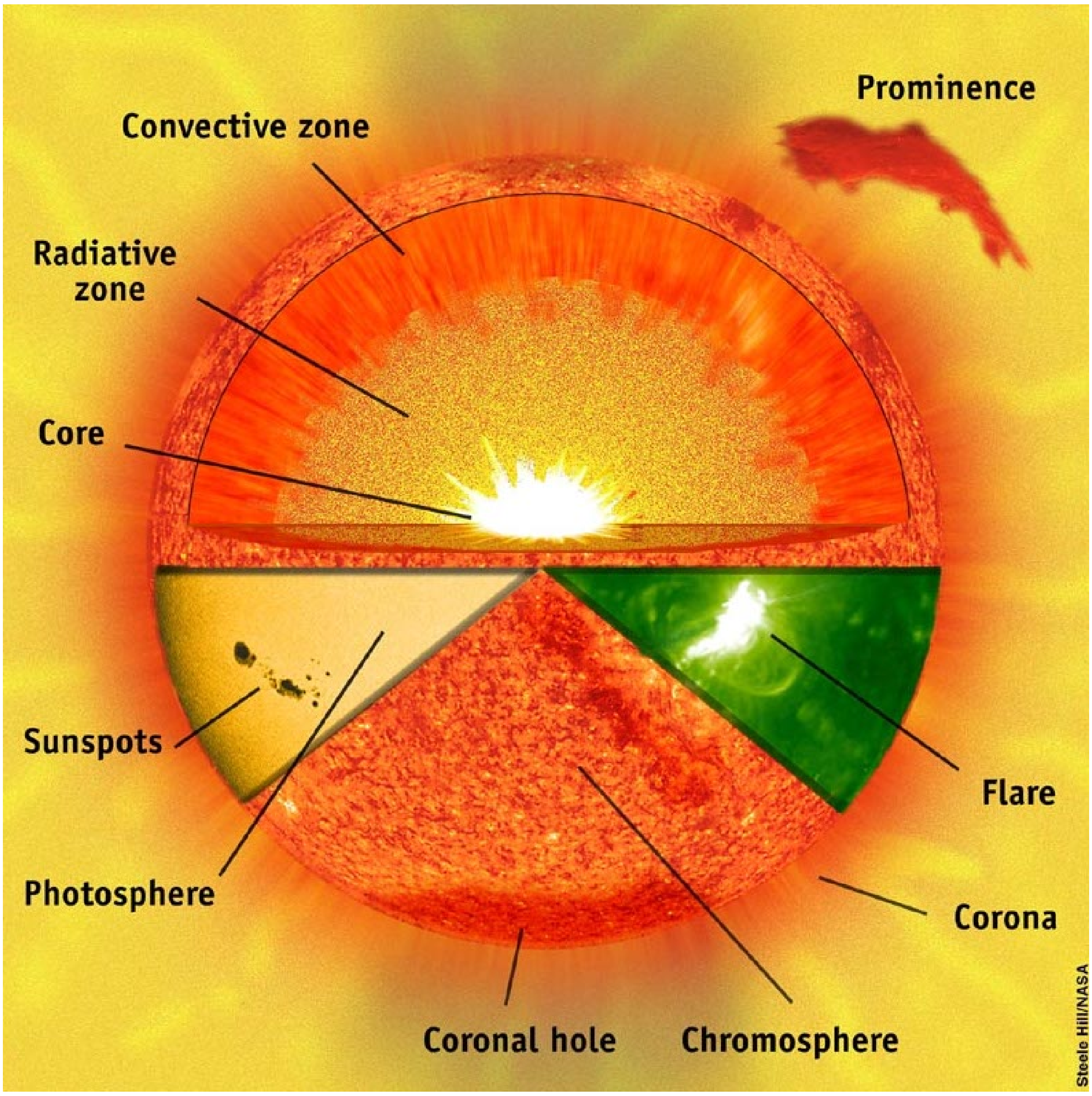

Figure 1.1: Layers of Sun showing the core, radiative zone, convective zone, photosphere, chromosphere, corona and other features like sunspots, prominence and flares. (*Courtesy of NASA*)

SOLAR INTERIOR

The material that makes up the sun is in hydrostatic equilibrium with a perfect balance between the forces of gravity and pressure gradient. As the surface of the sun loses energy by radiating away some heat, it cools down and hence gravitational contraction starts again, increasing the internal heat and building up pressure and to again restore equilibrium. This Kelvin-Helmholtz mechanism was earlier believed to be the source of energy of the Sun. But the Kelvin-Helmholtz time-scale of 20 million years was found to be less than the age of Earth, estimated by geologists to be at least 2 billion years. Sir Arthur Eddington in 1925 concluded that:

> *"The supply of heat replenishing that which the star radiates into space must come from the conversion of other forms of energy; and since the star remains apparently steady for exceedingly long periods of time, the radiation of the star must be just equal to the amount of energy converted in the interior. It is now believed that this conversion process is the liberation of subatomic energy"*
>
> - *The Internal Constitution of the Stars* by ARTHUR EDDINGTON

CORE: The energy that drives the sun comes from the controlled nuclear reactor sitting in the deepest layer called the core. Here the temperature is suitable enough for four protons to overcome the Coulomb barrier and fuse together to form a Helium nucleus via a 3 step nuclear process called the p-p chain reaction ($4p \rightarrow {}^4He + 2e^- + 2\nu_e + 2\gamma$). An equally important fusion reaction by which stars convert hydrogen to helium is the so called CNO cycle. In the Sun, only less than 7.3% of the helium is produced by the CNO cycle (Bahcall et al. 2003). The excess energy in the reaction is released as gamma rays and neutrinos. Neutrinos easily escape through the interior and into the outer space since they weakly interact with matter. They pass through the earth and are detected by neutrino observatories. It was found that, only 1/3rd of the total flux of electronic neutrinos predicted by the solar models were detected (*solar neutrino problem*). This missing neutrino problem was solved after all the three flavours of neutrinos (ν_e, ν_μ, ν_τ) were detected by the Sudbury Neutrino Observatory confirming the theory of "neutrino oscillations" (see Ahmad et al. 2002). This has verified the fundamental predictions of nuclear energy generation in stars. Further studies of the solar neutrinos will help us in fully understanding the processes occurring in the core of the sun and other stars.

RADIATIVE ZONE: The gamma ray photons produced by the nuclear reactions in the core enter the radiative zone. In this region the energy from the core is efficiently transported by radiation in this zone. The radiative zone extends from 0.25 $R_\odot$ to 0.7 $R_\odot$.The gamma ray photons interact with electrons in this region and loose energy. The mean free path of the photon is about 1 cm here and hence they take about a million years to finally reach the edge of the radiative zone. The temperature and density in these region is such that the hydrogen and helium are fully ionized but heavier species such as iron and oxygen and others are partially ionized. This region is characterized by uniform rotation, almost like a rigid body. Techniques of helioseismology and the studies done with GOLF (Global Oscillations at Low Frequency) and MDI (Michelson Doppler Imager) on-board the SoHO mission played a crucial role in our understanding of the radiative zone and establishing a Standard Solar Model. For instance, using these instruments and the inversion techniques of helioseismology, Couvidat et al. (2003) obtained the rotation profiles up to a depth of 0.2 $R_{\odot}$. The solar interior and the developments in the understanding of the rotation profiles has been reviewed by Howe (2009).

TACHOCLINE: The tachocline is a thin ($\lesssim 0.1\ R_{\odot}$) transition layer near 0.7 $R_{\odot}$ between the radiative zone and the convective zone (Spiegel & Zahn 1992), where the internal rotation of the sun changes from nearly uniform to differential. It is believed that owing to the radial shear, this region is the seat of the *solar dynamo*, through which the Sun's magnetic field is generated (e.g. Charbonneau et al. 1999). Helioseismic inversions have revealed the prolate structure of the solar tachocline, showing that it is shallower at higher latitudes than at the equator (for a review, see Howe 2009).

CONVECTIVE ZONE: The convection zone forms the outer envelope of the solar interior and extends from 0.7 $\mathrm{R}_{\odot}$ to 1 $\mathrm{R}_{\odot}$. At the base of the convection zone, the temperature drops to below 2 million K and atomic absorption processes occur, due to the fact that some of the heavier elements are not completely ionized. This makes the gas more opaque, and hence radiation cannot transport energy efficiently. Convection sets in, transporting hot plasma upwards and cooler material flows back down. Due to the combined effect of rotation and convection, this region is no more a rigidly rotating system. Apart from this differential rotation, helioseismic inversions have revealed a *meridional flow* in the poleward direction in the upper part of the convection zone. There is no conclusive evidence yet for the existence of an equator-ward return flow as part of the meridional circulation in the deeper layers of the convection zone. The differential rotation and the meridional circulation are very important ingredients of flux transport dynamo models that generate large scale solar cycle features (for a review see Dikpati & Gilman 2009).

The interior of the Sun is still not understood completely. The advancements in solar neutrinos, helioseismic inversion are yet to reveal more information about this region of the Sun which is less accessible.

SOLAR ATMOSPHERE

The atmosphere of the Sun is the layer which is accessible to study using both ground and space based telescopes. This region of the Sun can be studied using telescopes that cover the entire range of electromagnetic spectrum. A semi-empirical static model of the temperature stratification of solar atmosphere was constructed by Vernazza et al. (1981) from EUV continuum, Lα and other observations for different components of the visible surface. Figure 1.2 shows the temperature and density as functions of height for a model of the average quiet Sun (named as model C). The approximate height intervals where the various continua and line features originate are also indicated.

The atmospheric stratification of the Sun has (i) an outwardly decreasing temperature with height in the photospheric layers which emit radiation at visible wavelengths; (ii) a temperature minimum region where the temperature begins to increase with height; (iii) a chromospheric region where the temperature increases to values at which hydrogen starts to become partially ionized and the atmosphere starts to lose energy by Lyman line radiation; (iv) a narrow transition region separating the chromosphere and the fully ionized corona; and (v) the hot ($T > 10^6$ K) corona where hydrogen is fully ionized. These layers described below are briefly:

PHOTOSPHERE: The photosphere is the visible surface of the Sun. The Sun emits its energy mostly in the visible range of the electromagnetic spectrum; the photospheric surface is generally defined as the surface where the continuum optical depth is unity. The photosphere is around 500 km thick and is a stable layer in which the temperature drops from 5780 K to 4400 K. The drop in density and temperature makes transfer of energy through radiation more efficient once again in this layer whereby convective transport ceases. Its hard to define a sharp boundary between the photosphere and the underlying convection. The convective "overshoots" intrude into the stable layers of photosphere creating patterns on the visible surface called *granulation*. These features are studied by Doppler imaging and correlation tracking methods. The occasional dark patches that appear in these layers are called *sunspots*. The high resolution images from the Swedish 1-m Solar Telescope (SST) on La Palma, with a resolution of $0.12''$ (80 km on the Sun) at 4880 Å reveal in great detail the granulation. More recent observations of the photosphere comes from the *SOT* (Solar Optical Telescope) on-board the *Hinode* satellite.

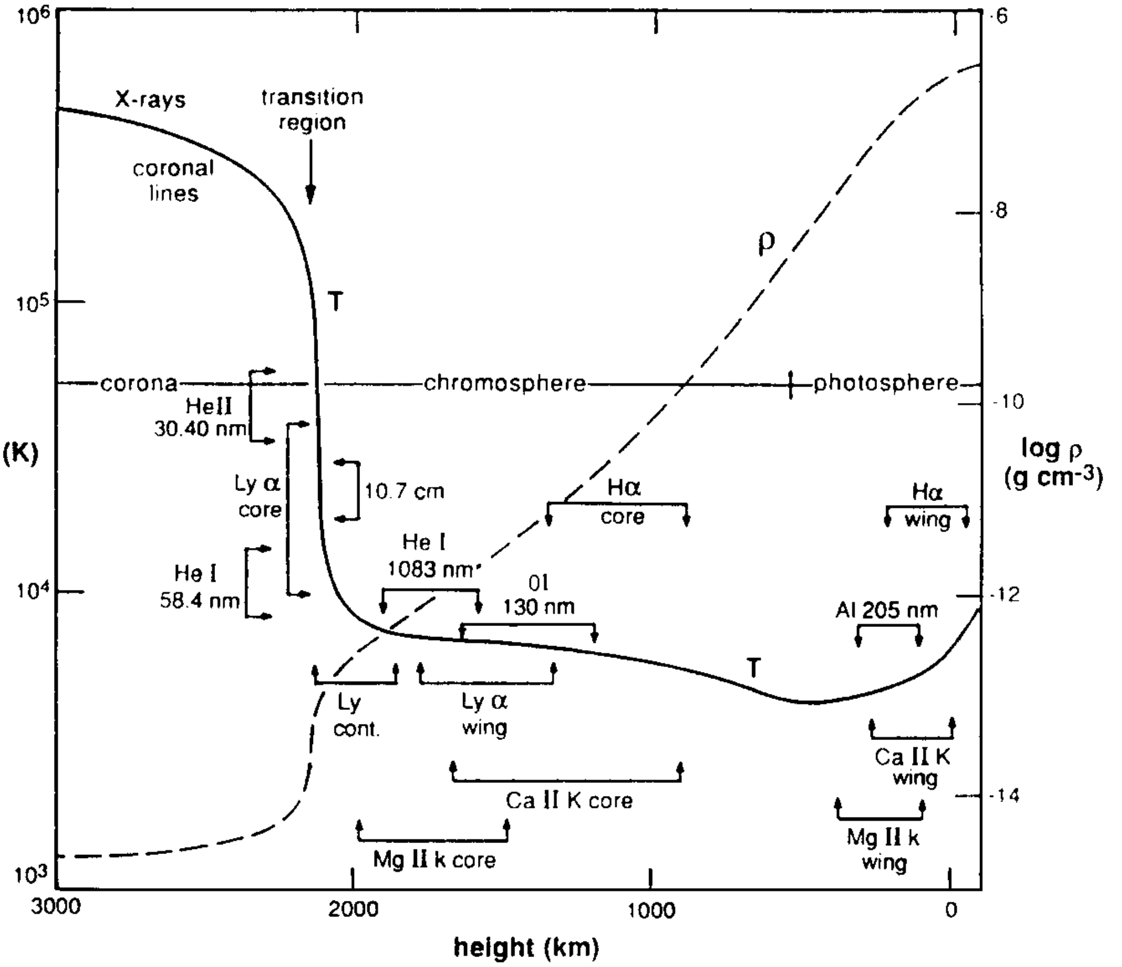

Figure 1.2: Temperature and density as functions of height for a model of the average quiet Sun (named as model C). The approximate height intervals where the various continua and line features originate are also indicated (adapted from Vernazza et al. 1981)

CHROMOSPHERE: The temperature decreases through the photosphere to a minimum value of around 4400K at a height of about 500 km, called the *temperature minimum*. After the temperature minimum region, the temperature no longer decreases but begins to increase with height. Hydrogen is partially ionized and the atmosphere loses energy by Lyman line radiation. The heating of the chromosphere is still not clearly understood. A multitude of various mechanisms have been suggested, but still a comprehensive picture is missing. The chromosphere is a very dynamic region and there are pockets of cooler material in it where molecules like carbon monoxide are present. Chromosphere is studied in various spectral lines of which the most important one are Hα, Ca II H & K, Ca II

8542.09 & 8662.14, etc.

TRANSITION REGION: The transition region is a thin layer where the temperature increases steeply from chromospheric values 2×10^4 K to coronal values of 1×10^6 K. The transition region contains highly ionized Ne VII, O VI, O IV emitting in EUV, have been extensively studied using *SoHO/SUMER* and *TRACE* satellites and more recently by *Hinode/EIS*.

CORONA: The corona is the outermost layer of the Sun, at a temperature of about 10^6 K. In the visible range, we see lines due to the forbidden transition of elements like iron (e.g. Fe XIV λ 5303 Å, Fe X λ 6374 Å) and calcium (e.g. Ca XV λ 5694 Å). The resonance lines of the ions in the coronal region are found in UV and X-ray wavelengths. These regions have been studied by *SoHO/UVCS*, *TRACE* and *Hinode/XRT*.

1.3 SOLAR MAGNETISM

Magnetic fields are present almost everywhere on the Sun. Without these fields the Sun would have been a rather dull object. How important are these magnetic fields is still a frontier field of research. One of the major challenges of solar physics is to understand why magnetic fields are so important.

The history of terrestrial magnetism dates back to 2500 years ago when according to a Greek legend a shepherd in a region called Magnesia discovered a strange attracting object. By 11 A.D. sailors already started using magnetic compasses. But it was William Gilbert who set out the new science of *electricity* and *magnetism* through his famous book *"De Magnete"* published in 1600. About 150 years later Charles-Augustin de Coulomb presented the laws describing the electrostatic attraction between electric charges. These were followed by the pioneering works of Hans Christian Oersted, André-Marie Ampère, Michael Faraday, Hendrik Antoon Lorentz and others. The marriage between *electricity* and *magnetism* discussed in Gilbert's *De Magnete* was finally put on a firm basis by James Clerk Maxwell in his famous book *A Treatise on Electricity and Magnetism* published in 1873, starting the field of *Electromagnetism*. In 1896, Pieter Zeeman discovered[*] the

---

[*] Zeeman, P. (1897). "On the influence of Magnetism on the Nature of the Light emitted by a Substance". Phil. Mag. 43:226.

splitting of certain spectral lines under the influence of a magnetic field.

George Ellery Hale in 1909 gave the first observational evidence[†] of magnetic fields on the Sun. This extraterrestrial magnetism discovered using the Zeeman effect gave a boost to studies related to Sun and its magnetism. It took almost half a decade to come back and confirm this observation (Babcock and Babcock in 1955) using a robust solar magnetograph developed by Babcock in 1953. The magnetograms revealed that magnetic fields existed outside sunspots also, showing that magnetic fields are omnipresent.

The major pursuit of solar physics is to understand the generation of these magnetic fields, the interaction between solar magnetic fields, dynamics, and radiation that makes the solar atmosphere an amazing research laboratory.

GENERATION AND EVOLUTION

Magnetic flux observed in the solar atmosphere is believed to be generated by a dynamo mechanism (*solar dynamo*) taking place somewhere in the lower part of the convection zone. The convection and the differential rotation is an essential ingredient for the solar dynamo. The magnetic field in the convective layers can be split into two components: poloidal (field in the meridional planes) and toroidal (directed east-west). Assuming a pre-existing poloidal field, in the first cycle of the dynamo, differential rotation generates a toroidal magnetic field by wrapping the north-south directed magnetic fields in the east-west direction. This is called the ω-effect. In the subsequent cycle, the convective motions under the influence of Coriolis force generate a poloidal field from the toroidal field by twisting the buoyantly rising east-west directed fields, a process called the α-effect. The full dynamo cycle is closed when a poloidal field has been generated. This mechanism can explain the periodicity of the solar cycle. Due to buoyancy, the generated field rises through the convection zone in the form of magnetic flux tubes. In the solar atmosphere, the emerging magnetic flux forms magnetically bipolar groups. Sunspots, the most conspicuous magnetic phenomena in the visible layers of the solar atmosphere are the manifestations of these bipolar fields. These active regions are responsible for the production of *flares* (intense and violent energy burst) and coronal mass ejections (CMEs). CMEs are events where very large amounts of hot gas, trapped by the magnetic field of the active region, are released from the Sun's atmosphere and into space. Apart from these large scale fields, the atmosphere is inhomogeneously filled with smaller and

---

[†] G.E. Hale, On the probable existence of a magnetic fields in sunspots. Astrophys. J. 28, 315343 (1908)

smaller scales of magnetic flux.

The Sun emits radiation that ranges in wavelength that spans the entire electromagnetic spectrum, from very short-wavelength X-rays, to ultraviolet (UV), visible, infrared (IR) and very long-wavelength radio waves. Solar irradiance gives a measure of this radiation. The Total Solar Irradiance (TSI) gives the total radiant energy per unit time (power) at all wavelengths that the Earth receives on unit area of its surface from the entire solar disk. The spectral irradiance gives the power per unit area in a particular wavelength range. It is seen that the solar irradiance is not constant. The TSI and the spectral irradiance fluctuate depending on the 11 year solar cycle, becoming stronger during the solar maxima and weaker during solar minima. The reason for this solar irradiance variability is still not clear. Magnetic fields are thought to play a very important role in the solar irradiance variability and activity.

MODERN VIEW OF THE SOLAR ATMOSPHERE

High resolution observations and large-scale numerical simulations have revealed the dynamic and inhomogeneous nature of solar atmosphere. Figure 1.3 shows a cartoon of the structure of the quiet Sun atmosphere by Wedemeyer-Böhm et al. (2009) incorporating the new results from observations and simulations. The different layers of the atmosphere is shown along with the magnetic network (thick solid curves) formed at the boundaries of the supergranulation formed due to large scale convective flows. These network fields expand to form the *canopy*, thus separating the atmosphere into two domains: canopy and sub-canopy. The internetwork also is filled with magnetic fields (thin dashed lines) with their foot points in the granulation below. The so called *clapotisphere* or *fluctosphere* is constantly showered with upward propagating shocks which have their origin in the underlying layers. They also show a strange phenomena called *spicules* which are a fundamental and ubiquitous component of the solar chromosphere. They extend all the way from the chromosphere up to the corona thereby connecting the corona with the photosphere. The picture also shows a new type of spicule called the Type II spicule, recently discovered by *Hinode/SOT*. In summary, the solar atmosphere exhibits myriad phenomena that is now slowly being unravelled by modern telescopes. Understanding of the magnetic coupling between the lower atmosphere and the corona is likely to uncover the mysteries concerning the heating of the upper atmosphere.

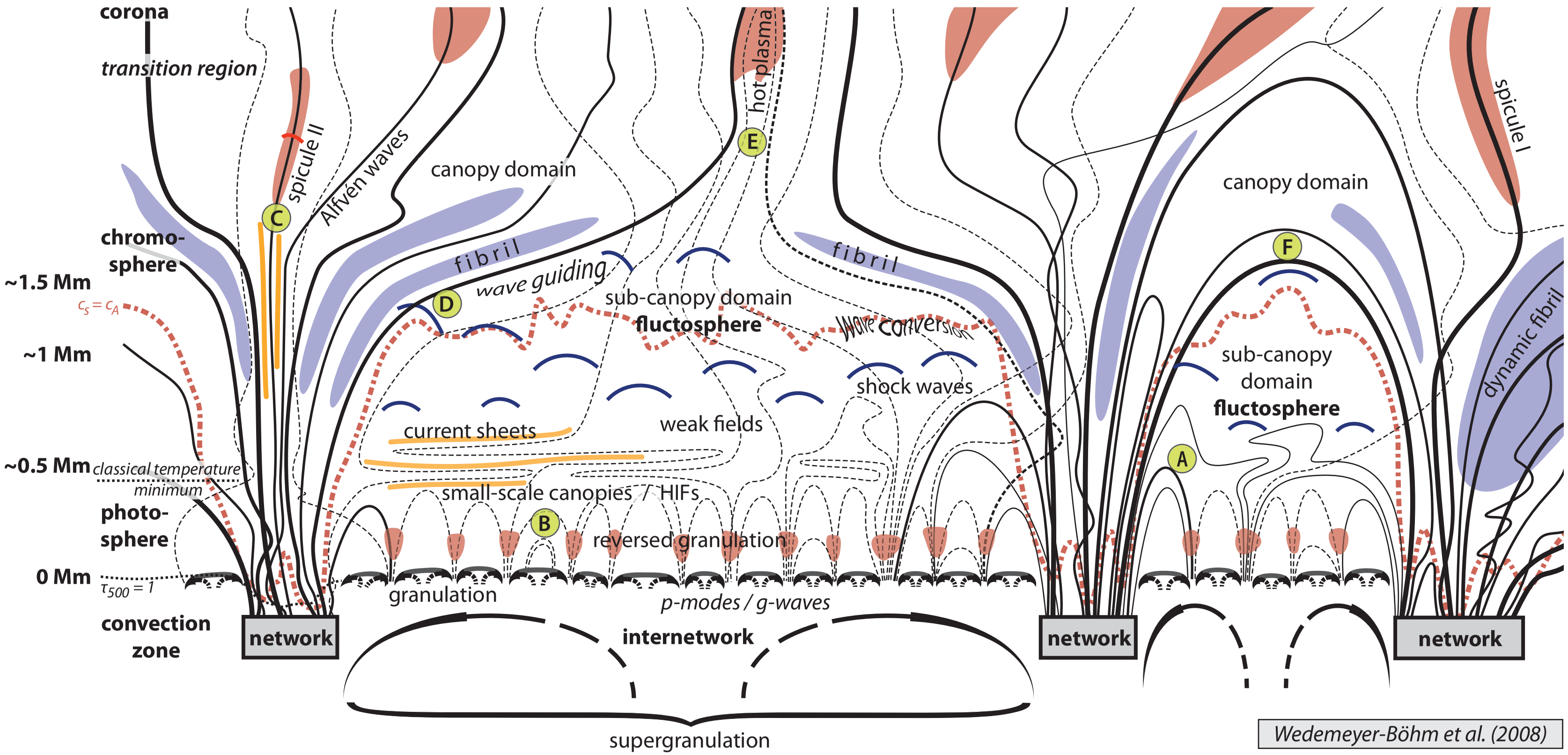

Figure 1.3: Cartoon of the lower quiet Sun atmosphere, showing the various features like, the magnetic network field (solid lines), internetwork field (dashed lines), the magnetic canopy fields, granulation and supergranulation, shocks, current sheets, *stratosphere* formed by the shocks, the surface of equal gas and magnetic energy density (red dot-dashed line), and observed features like spicules and type II spicules and fibrils (Courtesy of Wedemeyer-Böhm et al. 2009)

1.4 PLAN OF THE THESIS

Small-scale magnetic structures present in the quiet sun play a key role in solar irradiance variability as well as in the energy transport to the corona. Most small-scale magnetic flux concentrations are visible as bright objects with a magnetic field strength around kilogauss, with a typical size of 100 km and a field that is largely vertically oriented (Gaizauskas 1985). The solar variability at UV and EUV wavelengths is dominated by emissions from the "magnetic network". These network elements are thought to be heated by dissipation of magneto-hydrodynamic (MHD) waves, but the MHD processes involved in wave generation, propagation and dissipation are poorly understood.

As part of this thesis work, we carried out an investigation of MHD wave dynamics in magnetic network elements using numerical simulations. The work is performed in the context of a model of magnetic network elements as a collection of smaller flux tubes that merge at some height in the chromosphere. We have carried out a number of numerical simulations of wave propagation in a two-dimensional gravitationally stratified atmosphere consisting of individual magnetic flux concentrations representative of solar magnetic network elements. The main objectives of the work were: (a) to construct 2-D magnetostatic equilibrium models that closely resemble network elements; (b) to perform numerical simulations of MHD waves in order to examine wave generation in the magnetic network; (c) to study MHD wave propagation into the chromosphere and low corona in order to understand mode coupling and to estimate the energy transported by these waves; and (d) to predict observational signatures of MHD waves at various heights in the solar atmosphere.

This thesis is mainly based on a numerical simulation study of processes that take place in the solar atmosphere. There are two different routes that one can follow in a numerical simulation study: viz. "idealistic" and "realistic". A "realistic" simulation tries to recreate as much as what the we observe, while a "idealistic" simulation attempts to capture the basic physics accurately while dispensing with details. This thesis mainly follows the latter approach.

Numerical simulations of wave propagation in magnetically structured and gravitationally stratified atmospheres have helped us to identify various physical mechanisms that contribute to the dynamics of the magnetic network on the Sun. We have also explored the feasibility of developing diagnostic tools for the helioseismic exploration of such atmospheres using numerical simulations. Our work aims at contributing to a better understanding of the dynamics, particularly wave phenomena in the magnetic network of the Sun.

The outline of the thesis is as follows:

CHAPTER 1 (*present chapter*): This chapter gave an introduction to the Sun and the solar atmosphere as well as the motivation for carrying out the present investigation. The generation of magnetic fields, their nature and how they manifest themselves on the solar surface are discussed. This chapter presents a review of the current knowledge, state of research and highlights of latest developments in the field related to this thesis.

CHAPTER 2: This chapter discusses the structuring of the magnetic elements in the solar atmosphere, mainly focusing on small-scale structures. These are kilogauss flux concentrations formed by convective motions sweeping magnetic fields into intergranular lanes. Due to the geometry of these lanes, the magnetic flux is arranged in sheets or individual flux tubes. Earlier theoretical models (e.g. Bogdan et al. 2003) to explain the observations will be critically examined. We use the magnetohydrodynamics (MHD) approximation used for modelling these magnetic elements. Our investigations are based on the premise that thick flux sheets provide a more realistic model for the magnetic network. The initial atmosphere containing the flux sheet is computed in Cartesian coordinates using numerical methods described Steiner et al. (1986). The equilibrium model is computed by solving the magneto-hydrostatic equations with appropriate boundary conditions. A detailed description of the method and boundary conditions are presented. Construction of various magneto-hydrostatic equilibrium models of magnetic elements is also discussed. We start with a flux sheet in the magnetic network having a potential field structure. We then proceed by constructing non-potential flux sheets of varying field strengths in two-dimensional, gravitationally stratified atmospheric models with a temperature profile which is very similar to: (a) a photosphere and (b) a chromosphere. One of the important properties of these flux sheets concerns the varying widths of the boundary layer that separates the magnetic interior from the ambient medium, which is also studied in detail in the following chapters.

CHAPTER 3: Waves are present everywhere on the Sun. The main sources of waves in the photosphere are excited through, magneto-convection and the global p modes, which interact with the small scale structures in the photosphere and generate waves. The main focus of this chapter is to study wave generation and propagation in a two-dimensional, gravitationally stratified atmosphere comprising individual magnetic flux elements representative of the solar magnetic network. Waves are excited in the equilibrium magnetic field configurations which are discussed in Chapter 2. The MHD equations are solved following the numerical method given by Steiner et al. (1994). A detailed description on the method and boundary conditions of the numerical simulation is also presented. Our simulations shows a variety of wave modes excited in the flux sheet. We see that the nature of the modes excited depends upon the value of β (the ratio of gas to magnetic pressure) in the region where the driving motion occurs. We also see instances of "mode conversion" and "mode transmission" (Cally 2005, 2007) in our simulation. For a high-β medium, the slow wave is a transverse magnetic mode that propagates along the field lines and undergoes "mode transmission" as it crosses the $\beta = 1$ layer. In the case of low-β, the magnetically dominated fast wave within the flux sheet undergoes strong refraction and finally leaves the flux sheet, where it undergoes "mode conversion" to a fast, acoustically dominated wave. With numerical experiments we have explored the feasibility of using high frequency waves for probing the magnetic fields in the photosphere and chromosphere.

CHAPTER 4: Recent observations of the chromospheric network suggest that Ca II network grains are associated with plasma with quasi-steady heating at heights between 0.5 and 1 Mm inside magnetic flux concentrations. In the previous chapter we show that network fields carry waves generated deeper in the photosphere to higher layers where they transfer their energy into different wave modes by mode coupling. These fields can also excite acoustic waves in the surrounding field free regions. The quantitative estimate of the total energy that these waves carry to the higher layers will be discussed in this chapter. The energy losses in the magnetic network at chromospheric heights are of the order of 10^4 W m^{-2}. We show that although acoustic energy flux generated in strong flux concentrations can in principle balance this, the average fluxes are an order of magnitude less. In order to be compatible with the observed quasi-steady Ca emission the injection needs to be in the form of sustained multiple short duration pulses but they could probably not maintain the values of acoustic flux to balance the chromospheric energy loses, implying that acoustic waves would hardly balance the chromospheric energy requirements.

CHAPTER 5: Apart from identifying various physical mechanisms that contribute to the dynamics of the magnetic network on the Sun, numerical simulations of wave propagation in magnetically structured and gravitationally stratified atmospheres also provide diagnostic tools for the helioseismic exploration of such atmospheres. The main objective of this chapter is to predict observational signatures of MHD waves at various heights in the solar atmosphere by computing synthetic spectral lines. This can be compared with existing and new observations in order to place constraints on different wave excitation mechanisms. We have used the Stokes profile code DIAMAG (Grossmann-Doerth 1994) to compute the emergent stokes profiles of various photospheric lines emerging from the top of our simulation box in the case of various flux sheet models discussed in the previous chapter. We show that a clear evidence of wave phenomena can be seen in these profiles only when we look at highly resolved line-of-sights on either sides of the flux sheet. Profiles averaged over the entire flux sheet does not show signs of wave phenomena. We have also identified signatures of wave mode couplings present in them.

CHAPTER 6: This chapter provides a summary and conclusion of the thesis. Our research aims to understand the generation, propagation and energy transport of waves in magnetized solar atmosphere. The numerical studies carried out in this thesis contribute towards a better understanding of the coupling between transverse and longitudinal waves in solar magnetic structures and the heating of solar and stellar chromospheres. The search for observable effects associated with MHD waves will provide a new diagnostic tool for probing MHD waves in the solar atmosphere. Our results compared with high resolution observation will result in constraints and will motivate further improvements in theoretical and numerical modeling work.

CHAPTER 2

STRUCTURE*

Solar atmosphere harbours magnetic structures on every possible scale. Appearing to be well separated from the surrounding relatively unmagnetized plasma, they form a hierarchical order in spatial scales. Ranging from the most conspicuous *sunspots* (diameters between tens of Mm† to 50 Mm), to *pores* (0.5 Mm to 5 Mm), all the way down to scales that are orders of magnitude smaller than sunspots. The small scale structures at the lower end of the hierarchy that can be seen using Zeeman‡ techniques are called *magnetic flux tubes* or *knots*.

2.1 SMALL SCALE STRUCTURES

The "salt and pepper" appearance of the magnetogram of a quiet sun region reveals that the quiet sun is filled with intermittent magnetic flux fragments of mixed polarities (see Stenflo 1994). The first observational evidence about the inhomogeneous nature of quiet sun magnetic field came from the works of Sheeley (1966, 1967) using spectroheliograms taken at the Mount Wilson Observatory. They found regions of sizes as small as 500 km with magnetic field of several hundred Gauss thereby confirming the existence of the so called "invisible sunspots" as reported by Hale & Nicholson (1938). These flux concentrations are associated with cellular convective patterns referred to as photospheric granulation. The small scale intense fields observed at the granular and supergranular boundaries are formed by the accumulation of magnetic flux by the converging flows

---

[*] Part of publications: Hasan et al. (2006), Vigeesh et al. (2009)

[†] Mega meter (Mm) = 1000 kilo meter (km), an appropriate length scale used in Solar context

[‡] Discovered by P. Zeeman in 1896, Zeeman effect refers to the splitting of spectral lines into polarized components in the presence of a magnetic field.

Table 2.1: Table of typical magnetic Reynolds number on the Sun

Flow	l_0 $[m]$	v_0 $[ms^{-1}]$	σ $[\Omega^{-1}\ m^{-1}]$	η $[m^2 s^{-1}]$	R_m
Sun	10^9	100	10^4	100	10^9
Solar Atmosphere	10^6	10^3	10^3	10^3	10^6
Granulation	8×10^5	10^3	10^3	10^3	10^5
Supergranulation	1.5×10^7	10^3	10^3	10^3	10^6
Solar Wind (at 1AU)	10^8	3×10^5	10^4	100	10^{11}

which are part of a convection cell. It is now believed that the formation of these kilogauss fields proceed by the following process:

FLUX EXPULSION

The velocity fields and the magnetic fields in the solar photosphere strongly interact with each other. The coupling between the flow and the magnetic field is due to the high electrical conductivity (σ) of the photospheric gases which are typically of $10^3\ \Omega^{-1}m^{-1}$, so the magnetic diffusivity[§], η is 10^3 m^2 s^{-1}. It can be shown that the evolution of the magnetic field due to flows is governed by the magnetic induction equation (e.g. Priest 1982),

$$\frac{\partial \boldsymbol{B}}{\partial t} = \boldsymbol{\nabla} \times (\boldsymbol{v} \times \boldsymbol{B}) + \eta \boldsymbol{\nabla}^2 \boldsymbol{B}. \tag{2.1}$$

Considering typical length scale, l_0 and velocity, v_0, a dimensionless quantity called the "magnetic Reynolds number", defined as,

$$R_m = \frac{l_0 v_0}{\eta}, \tag{2.2}$$

determines the domination of the convective term $|\nabla \times (\boldsymbol{v} \times \boldsymbol{B})|$ over the diffusive term $|\eta\nabla^2\boldsymbol{B}|$ in the induction equation, Eq (2.1). Some typical values of the magnetic Reynolds number seen in a astrophysical body like the Sun are given in Table 2.1.

The magnetic Reynolds numbers have large values, which means that the convective term dominates in the solar atmosphere over diffusion and the magnetic field lines behave as if they move with the plasma according to Alfvén's frozen flux theorem by (Alfven 1950). Thus the observed supergranulation flows are very likely to expel and concentrate magnetic fields around the boundaries of the cell, a process termed as "flux expulsion". Parker (1963) showed that the photospheric motions accumulate the magnetic fields into

---

[§] $\eta = \frac{1}{\mu_0\sigma}$, where $\mu_0 = 4\pi \times 10^{-7}$ H m^{-1}, is the permeability of free space narrow filaments thereby increasing the field strength. The equipartition between magnetic energy density of flux tubes and the kinetic energy density of the granular flow can increase the field strength up to ~ 400 G. Flux concentration stops when an equipartition between the two energy densities is reached. With a gas density of 3×10^{-4} kg m^{-3} at the surface of the sun and a typical flow speed of 1 km s^{-1}, the equipartition field strength given by,

$$\frac{B^2}{2\mu} = \frac{1}{2}\rho v^2 \tag{2.3}$$

requires a field strength of few hundred gauss which is well below the kilogauss value in small-scale magnetic elements. The maximum limit of the field can be easily deduced by calculating the pressure balance between the flux tube and the ambient medium. When the flux tube is completely evacuated of gas,

$$B = \sqrt{2\mu p_e}, \tag{2.4}$$

where p_e is the ambient gas pressure. From Eq. (2.4), we find $B_{\max} = 1600$ G at the base of the photosphere. The growth of the field to this limiting value is prevented by the horizontal flow (Galloway et al. 1977). The intensification of the field to a kilogauss strengths occurs due to "convective collapse" as described below.

CONVECTIVE COLLAPSE

The magnetic field attains equipartition strength in regions where the flows converge into a downdraft at the boundaries of supergranulation cells. The convective heat transport is strongly suppressed within these flux concentrations similar to sunspots. The back reaction of the field on the horizontal flow due to Lorentz force thermally isolates the flux tube from bringing more heat into it, resulting in a strong cooling of the gas flowing downward within the field. The gas pressure within the field decreases accelerating further downfall and thereby evacuating the upper layers. The field amplified in the flux tube in order to maintain pressure equilibrium with the super-adiabatic surroundings. This "super adiabatic effect" proposed by Parker (1978) was investigated using a linear stability analysis by different authors (Webb & Roberts 1978; Spruit & Zweibel 1979; Unno & Ando 1979) in the framework of the thin flux tube approximation (see Section: 2.3) in the adiabatic limit. They showed that, a convective instability sets in resulting in either a downflow or an upflow. If the instability occurs in a magnetic flux tube embedded in an updraft, the pressure increases and it heats up and there is no new equilibrium reached and hence the whole tube disperses. On the other hand, if the instability occurs in a flux tube with a downdraft, it is subject to strong cooling so that the temperature within the flux tube falls below the temperature of the ambient medium, the pressure decrease and the action of gravity strongly evacuates the tube from the top layers in the photosphere, leading to amplification of the magnetic field. This process is referred to as "convective collapse", which eventually quenches the instability when the field becomes sufficiently strong.

A linear analysis taking into account heat exchange between the flux tube and its surroundings was carried out by Webb & Roberts (1980b,a) and Hasan (1986) for a realistic stratification. Non linear, time dependent calculations of the instability in the thin flux tube approximation were performed in adiabatic case by Hasan (1983); Venkatakrishnan (1983); Hasan (1984b). They were extended to include radiative heat exchange through Newtons laws of cooling (Hasan 1984a, 1985), the Eddington approximation (Hasan 1988) and the diffusion approximation (Rajaguru & Hasan 2000). These investigations showed that convective collapse initially leads to the intensification of magnetic field. The final state is an over-stable one exhibiting stationary oscillations (Hasan 1985) or ends up to form a static state (Takeuchi 1993, 1995) depending on the boundary conditions.

Magneto-convection, or the dynamical interaction of the field with a convective fluid was studied in the Boussinesq approximation[¶] using two dimensional numerical simulations by Meyer et al. (1979); Galloway & Weiss (1981) (see the review by Proctor & Weiss 1982) and in three dimensions by Galloway & Proctor (1983). They found that although the magnetic fields are initially swept into the granular boundaries, eventually a stable state is reached where most of the flux is concentrated in the centre of the cell. Since the Boussinesq approximation assumes that the fluid is incompressible, the evacuation of the tube cannot be modelled as required by the "convective collapse" model. The numerical simulations of compressible magneto-convection that followed these work, showed that occurrence of cellular patterns with strong downflows at the boundaries (Hurlburt et al. 1984).

More realistic numerical simulation of magnetoconvection started with the work of Nordlund (1983), who showed that the fields are swept away into the intergranular lanes by the converging granular flow and that the convective instability is responsible for the intensification of fields above the equipartition value. Later studies by Nordlund (1986); Nordlund & Stein (1989) in three dimensions, and also in two dimensions by Grossmann-

---

[¶] Boussinesq approximation (Boussinesq 1903) refers to an approximation in which the perturbations in density is negligible and it appears only in the buoyancy force term. Hence the fluid can be considered as incompressible (from Eq. (2.5)), for instance, a liquid or a shallow layer of gas such that the hydrostatic vertical pressure difference is negligible

Doerth et al. (1998) found evidence of convective intensification of magnetic fields. These works were followed by many authors (e.g. Sheminova & Gadun 2000; Gadun et al. 2001; Vögler et al. 2005; Cheung et al. 2007; Danilovic et al. 2009).

The first observational evidence on the high spatial correlation between magnetic field and granular downdraft came from high spatial resolution ($0.5''$) observations made at Sac Peak Vacuum Tower Telescope by Title et al. (1987). These showed that the concentration of magnetic field by flow pattern into granular lanes is in good agreement with the numerical simulations by Nordlund (1983). The spectropolarimetric confirmation of the convective collapse process were first reported by Bellot Rubio et al. (2001) using the Tenerife Infrared Polarimeter (TIP) on the German Vacuum Tower Telescope. Recent observations using the Solar Optical Telescope (SOT) aboard *Hinode* (Tsuneta et al. 2008) with a spatial resolution of $0.2''$ enabled investigations of the evolution of small scale magnetic elements with unprecedented accuracy. Nagata et al. (2008) provided strong support for the convective collapse hypothesis. More conclusive evidence have been presented very recently by the work of Fischer et al. (2009) who observed around 49 such events with a magnetic field intensification upto 1.6 kG and an associated brightening in the continuum and Ca II H images.

The quiet Sun chromosphere can be separated into two regions: magnetic network and internetwork. While the magnetic field in the internetwork regions of the quiet Sun is mainly predominantly horizontal (Lites et al. 2008) with a rare occurrence of flux concentrations greater than few hundred gauss, the magnetic network shows an abundance of vertical flux concentrations with kilogauss fields. “Magnetic networks” are localized regions of strong vertical magnetic fields at the inter-granular boundaries with a typical field strength of a kilogauss and a diameter of few hundred kilometres (Gaizauskas 1985; Zwaan 1987). High resolution filtergrams taken in Ca II H (3968 Å) or K (3933 Å) reveals the network as small brightenings at the periphery of supergranulation cells. These network bright points (Stenflo & Harvey 1985; Muller 1985), are the beads or the historical “crinkles” in the chain like formation called “filigree” by Dunn & Zirker (1973) who observed in the wings of Hα.

The location of bright points seen in images of Ca II H and K line can be mapped with G-band bright points (Rutten & Uitenbroek 1991). These observation confirm the fact that flux tubes extend to chromospheric heights and even higher. It is seen that the bright points in Ca II H and K line are diffuse in nature relative to the G-band bright points. This can be explained if the flux tubes expand with height since Ca II H & K lines form higher in the atmosphere than the G-band.

The theoretical studies followed by large scale numerical simulations and the high spatial resolution observations agree upon the fact that the small scale structures seen at photospheric level can be approximated as flux tubes or flux sheets. Magnetic flux tubes are the building blocks of the solar atmosphere. Their study requires an understanding of magnetohydrodynamics.

2.2 MAGNETOHYDRODYNAMICS

Magnetohydrodynamics (MHD) describes the behaviour of plasma in the presence of magnetic field. In the photospheric layers of the solar atmosphere, the effect of viscosity, or thermal conduction, or finite resistivity are irrelevant and therefore all the dissipative processes can be neglected. Such a fluid can be assumed to be an ideal fluid and can be studied using equations of ideal MHD. The equations of MHD are the combination of governing equations of hydrodynamics and electrodynamics with the displacement current ignored from the later (e.g. Priest 1982) and are given below,

CONTINUITY EQUATION: The equation of mass conservation can be written as,

$$\frac{\partial \rho}{\partial t} + \boldsymbol{\nabla} \cdot (\rho \mathbf{v}) = 0, \tag{2.5}$$

where ρ is the density of the fluid element. This equation says that, as time evolves, the density will increase (or decrease) if there is a total influx (or outflux) of matter into the fluid element.

MOMENTUM EQUATION: The equation of motion gives the acceleration of a fluid element under the influences of various forces. It can be written as,

$$\rho \frac{\partial \mathbf{v}}{\partial t} + \rho(\mathbf{v} \cdot \boldsymbol{\nabla})\mathbf{v} = -\boldsymbol{\nabla} p - \rho g + \boldsymbol{J} \times \boldsymbol{B} + \nu \rho \boldsymbol{\nabla}^2 \mathbf{v}, \tag{2.6}$$

where, the LHS (left hand side) represents the rate of change of the momentum of the fluid element as it is carried away by the flow[‖]. The RHS (right hand side) gives the forces that act on the fluid element: viz. pressure gradient, gravity, the Lorentz force and

---

[‖] The LHS can also be written as

$$\rho \frac{D\mathbf{v}}{Dt} = -\boldsymbol{\nabla} p - \rho g + \boldsymbol{J} \times \boldsymbol{B} + \nu \rho \boldsymbol{\nabla}^2 \mathbf{v},$$

the viscous term, where ν denotes the kinematic viscosity. We assume an ideal fluid and neglect the viscous force, which is valid if the Reynolds number (R_e) given by,

$$R_e = \frac{l_0 v_0}{\nu} \tag{2.7}$$

is much greater than unity. The Reynolds number, R_e is the ratio of the viscous term to the advective term (second term in the LHS) in Eq. (2.6)

MAGNETIC INDUCTION EQUATION: The magnetic induction equation can be written as,

$$\frac{\partial \boldsymbol{B}}{\partial t} = \boldsymbol{\nabla} \times (\boldsymbol{v} \times \boldsymbol{B}) + \eta_m \nabla^2 \boldsymbol{B}. \tag{2.8}$$

This equation determines the evolution of the magnetic field when fluid motions act on the magnetic field. As shown in 2.1 the convective term dominates over the diffusive term in the magnetic induction equation and hence the frozen-in condition applies to the field in the photosphere and chromosphere. So, in the perfectly conducting limit ($R_m \gg 1$), the second term in Eq. (2.8) can be neglected.

ENERGY EQUATION: The equation of conservation of energy can be written in many ways. In terms of the entropy (s), it takes the form,

$$\frac{\partial s}{\partial t} + \boldsymbol{v} \cdot \boldsymbol{\nabla} s = 0, \tag{2.9}$$

where there are no sources or sinks of energy (adiabatic limit). Hence the entropy of each fluid element remains constant in time.

EQUATION OF STATE: The gas pressure is determined by the equation of state, given as,

$$p = f(\rho, T), \tag{2.10}$$

---

where,

$$\frac{D}{Dt} = \frac{\partial}{\partial t} + \boldsymbol{v} \cdot \boldsymbol{\nabla},$$

is called the Lagrangian or the material derivative, which gives the time variations following the fluid element in motion. $\frac{\partial}{\partial t}$ is called the Eulerian derivative, which gives the time variation of a quantity in a fixed point in space.

For an ideal gas, this takes the form,

$$p = \frac{\rho \mathcal{R} T}{\tilde{\mu}} \tag{2.11}$$

where $\mathcal{R}$ is the gas constant and $\tilde{\mu}$ is the mean atomic weight.
The above equations are constrained by the divergence free condition on $\boldsymbol{B}$, given by,

$$\nabla \cdot \boldsymbol{B} = 0 \tag{2.12}$$

The above set of equations (from Eq. 2.5- 2.12) form the basic equations of MHD for an inviscid adiabatic fluid. These equations are used to determine the time evolution of density (ρ), momentum ($\rho \mathbf{v}$), entropy (s), and the magnetic field ($\boldsymbol{B}$).

2.3 FLUX TUBE APPROXIMATION

At the level of the photosphere, high resolution observations can resolve islands of magnetic elements from the field free surrounding. The standard model of the magnetic field structures in the solar atmosphere is based on the interpretations of the magnetogram images of the photosphere in terms of the so-called "two component model" (Stenflo 1973). Magnetic flux tubes, the basic building blocks of solar magnetism, are isolated structures embedded in an ambient medium with weak field.

2.3.1 THIN FLUX TUBE

Early studies of the structure of magnetic flux tubes and wave propagation in them were carried out under the assumption of the flux tubes being "thin". The "thin flux tube approximation" was developed in order to reduce the full MHD equations to a tractable form for analytical studies. The "magnetohydraulic" approximation of Defouw (1976) considered thin flux tubes embedded in an isothermal atmosphere. The zeroeth order thin flux tube approximation of Roberts & Webb (1978) considered more intense thin flux tubes with an atmosphere in which the scale height is a function of height. In the zeroeth order thin flux tube approximation, the complete MHD equations are expanded about the axis and only the lowest order term is retained. Thus, in the magnetic tube, the quantities vary along the length of the tube and not in the transverse direction. The resulting equations are (see Roberts & Webb 1978):

CONTINUITY EQUATION

$$\frac{\partial \rho}{\partial t} + \rho(\boldsymbol{\nabla} \cdot \boldsymbol{v}) + \boldsymbol{v}_z \frac{\partial \rho}{\partial z} = 0 \tag{2.13}$$

MOMENTUM EQUATION

$$\rho \frac{\partial \boldsymbol{v}_z}{\partial t} + \rho \boldsymbol{v}_z \frac{\partial \boldsymbol{v}_z}{\partial z} = -\frac{\partial p}{\partial z} - \rho g \tag{2.14}$$

ENTROPY EQUATION

$$\frac{\partial s}{\partial t} + \boldsymbol{v}_z \frac{\partial s}{\partial z} = 0, \tag{2.15}$$

MAGNETIC INDUCTION EQUATION

$$\frac{\partial \boldsymbol{B}}{\partial t} = -(\boldsymbol{\nabla} \cdot \boldsymbol{v}_z)\boldsymbol{B} + \boldsymbol{B}\frac{\partial \boldsymbol{v}_z}{\partial z} - \boldsymbol{v}_z \frac{\partial \boldsymbol{B}}{\partial z} \tag{2.16}$$

We assume that the temperature inside the flux tube and the ambient medium are equal. The internal and external pressures are related using the pressure balance condition,

$$p_i + \frac{B^2}{2\mu} = p_e. \tag{2.17}$$

With the boundary condition specifying the internal pressure and the magnetic strength at the bottom, the equilibrium of a thin flux tube is completely characterized by a single parameter, the scale height, which can be used to determine the magnetic field as a function of height from the pressure profile.

Early works mainly studied the transverse and longitudinal waves excited by impact of granules on flux tubes (Hasan & Kalkofen 1999; Hasan et al. 2000). All these studies modelled them as thin-flux tubes. The zeroeth order thin flux tube approximation were followed by higher order thin flux tubes approximation (Ferriz-Mas et al. 1989). But the thin flux tube approximation becomes invalid at about the height of formation of the emission peaks in the cores of the Ca II H and K lines. Hasan et al. (2003) compared a thin flux tube with an exact magnetostatic solution and showed that both agree reasonably well only upto a height of 1 Mm above the base of the photosphere. Also, this approximation does not treat the dispersion of magnetic waves caused by the variation of the magnetic field strength across the flux concentration and it does not take into account the emission of acoustic waves into the ambient medium.

2.3.2 THICK FLUX TUBE

Potential field models to describe the structure of magnetic field in small flux tubes were developed by Simon et al. (1983). These small flux tubes form even more complicated field structures that merge with their neighbouring flux tubes.

Potential field

A potential field or current-free field is a field configuration in which the current density is zero everywhere. If the equilibrium magnetic field is free from electric currents,

$$\boldsymbol{j} = 0. \tag{2.18}$$

then,

$$\nabla \times \boldsymbol{B} = 0. \tag{2.19}$$

Let us assume a 2-D configuration in the $x - z$ plane. From Eq. (2.19), the magnetic field can be expressed in terms of a potential function, $\phi(x, z)$ as,

$$\boldsymbol{B} = \nabla\phi. \tag{2.20}$$

The $\phi(x, z)$, the *scalar magnetic potential*, also know as the *stream function* satisfies Laplace's equation,

$$\nabla^2\phi = 0. \tag{2.21}$$

The magnetic field is constructed by solving the Laplace equation with appropriate boundary conditions at the base (here $z = 0$ corresponds to the base of the photosphere) and at the top and side boundaries. Simon et al. (1983) used boundary condition in which the vertical component of magnetic field (B_z) is defined by a Gaussian function or a step function at $z = 0$ and a monopole-like field at $z = \infty$. We follow a similar approach.

Method and Boundary conditions

We construct a simple potential field model of a magnetic network. Assuming axial symmetry, the Laplace's equation for ϕ is solved on a computational domain consisting of only half of the flux sheet with horizontal and vertical extensions of 600 km and 1200 km, respectively. This domain is discretized on a equidistant rectangular mesh with a spacing of 5 km. The left boundary of the domain corresponds to the axis of the flux sheet. The value of ϕ is prescribed at the left ($\phi = 0$) and the right side ($\phi = \phi_{\mathrm{max}}$) boundaries (Dirichlet type boundaries). Figure 2.1 shows the variation of ϕ as a function of horizontal distance at the bottom boundary. The vertical component of the field at the bottom boundary is specified as follows,

$$B_z(x, z = 0) = \left.\frac{\partial\phi}{\partial x}\right|_{at\, z=0} = B_0 \mathrm{sech}^2(x),$$

and at the top boundary we assume that the field is vertical with a uniform value so that,

$$B_z(x, z = 1200\ \mathrm{km}) = \left.\frac{\partial\phi}{\partial x}\right|_{\mathrm{at\ z=1200\ km}} = B_{\mathrm{uniform}}.$$

These choices result in a Neumann condition at these boundaries. The field strength (B_0) and gas pressure on the axis at the base are specified. The gas pressure as a function of height is similar to Eq. (2.38), with two pressure scale heights. The resulting field configuration is shown in Fig. 2.2 by plotting contours of ϕ = const., which represent

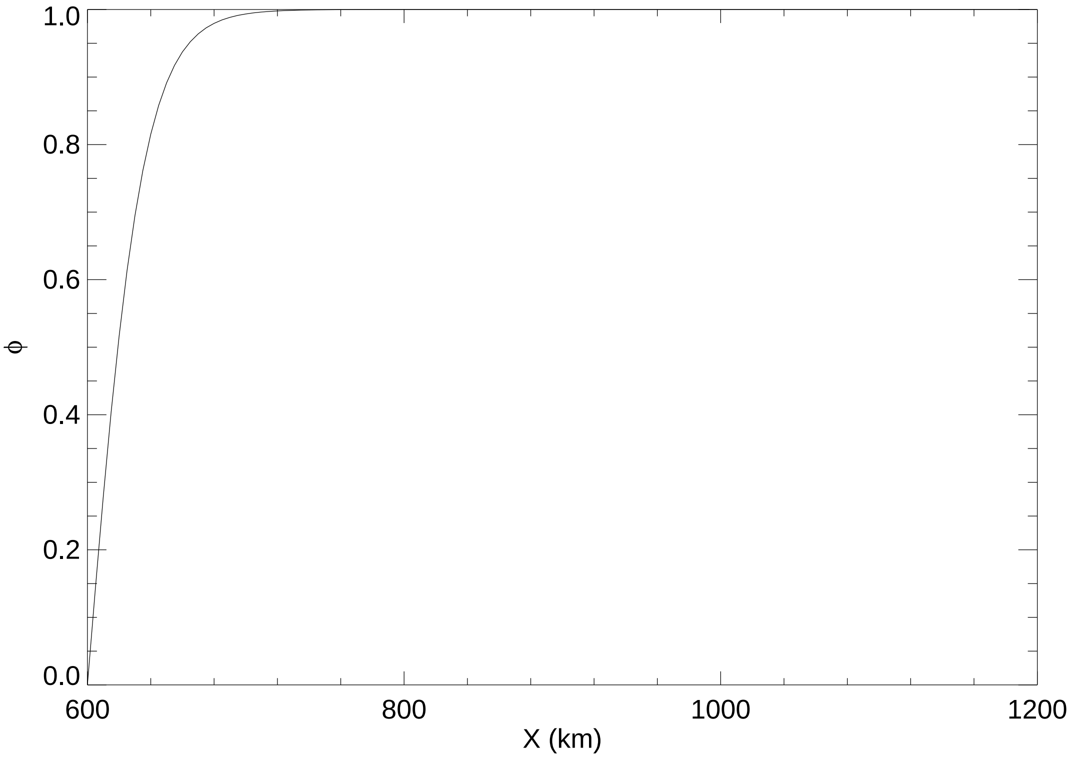

Figure 2.1: The stream function (ϕ) as a function of horizontal distance x at the bottom boundary.

magnetic field lines[**]. Some of the properties of the potential field readily noticed is the

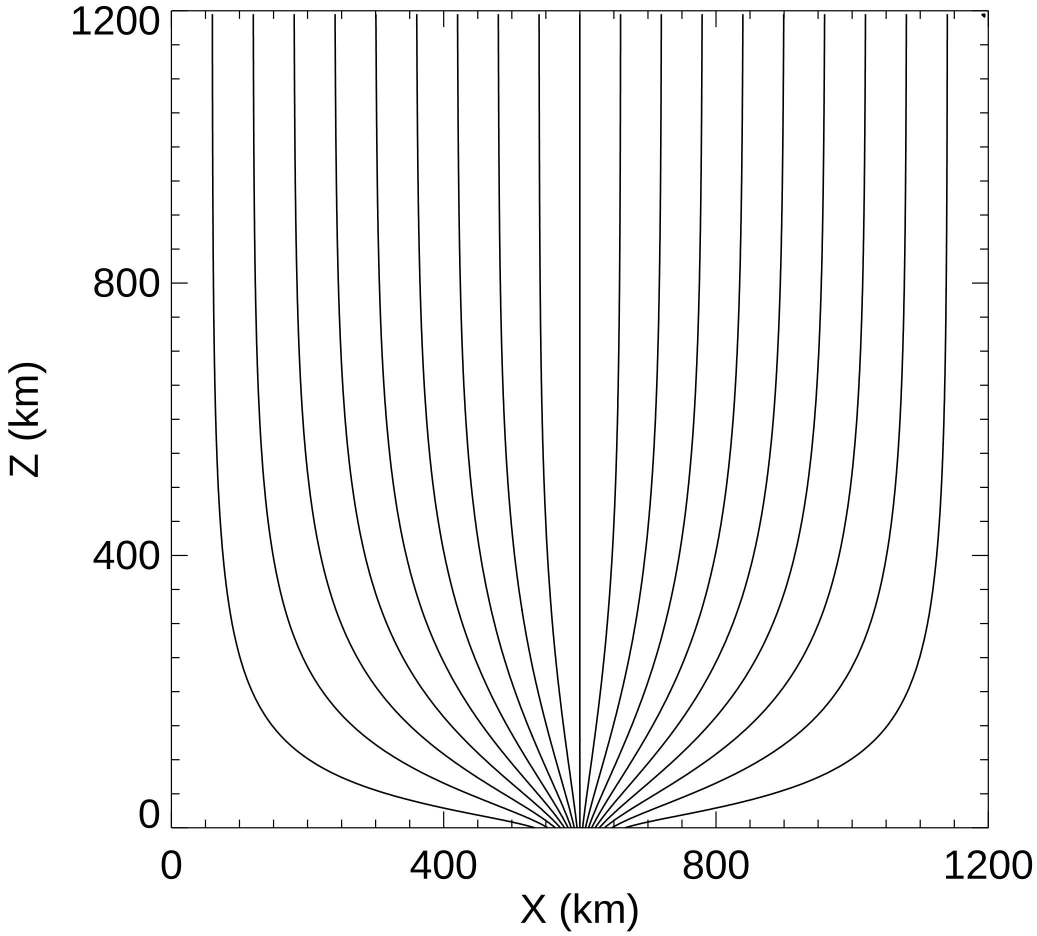

Figure 2.2: Magnetic field lines for a potential field configuration.

uniform spreading of the fields in the horizontal direction as soon as it emerges from a small region in the base. It should be noted that there is no sharp interface that separates the field from the ambient medium. Out of the many field configuration possible for a given boundary condition on the magnetic field, a potential field has the least energy

---

[**] A magnetic field line or magnetic line of force is a curve such that the tangent at any point gives the direction of the magnetic field. The concept of magnetic field lines were developed by Micheal Faraday(Nineteenth Century) for representing the configuration of the magnetic field.

given by (for e.g. see Priest 1982),

$$W_B = \int_V \frac{B^2}{2\mu} dV. \tag{2.22}$$

Thus every stationary flux tube, in the absence of a source, should eventually settle down to its minimum-energy configuration given by a potential field. Since the solar atmosphere is very dynamic, the thermal gas pressure, kinetic energy density and the energy density of the magnetic field are all of similar magnitude in the photosphere, the fields remain non-potential. To model a more realistic field configuration, the full magnetostatic force balance equation has to be solved. The computational difficulties of solving the non-linear magnetostatic equations were overcome by robust methods developed by Pizzo (1986); Steiner et al. (1986); Steiner & Pizzo (1989).

2.4 MAGNETOHYDROSTATIC FLUX TUBES

When electric currents are non zero, the equilibrium structure of the flux tube is determined by the magnetostatic force balance equation given as,

$$-\nabla p + \rho \boldsymbol{g} + \boldsymbol{J} \times \boldsymbol{B} = 0, \tag{2.23}$$

along with,

$$\nabla \times \boldsymbol{B} = 4\pi \boldsymbol{J} \tag{2.24}$$

and,

$$\nabla \cdot \boldsymbol{B} = 0 \tag{2.25}$$

Using Eq. (2.25), the magnetic field (assuming a 2-D configuration as before) can be written in terms of the flux function ψ as

$$\boldsymbol{B} = \nabla \times \psi \hat{\boldsymbol{y}} \tag{2.26}$$

The components of magnetic field in two dimensional Cartesian coordinates in terms of $\psi(x, z)$ become,

$$B_x = -\frac{\partial \psi}{\partial z}, B_z = \frac{\partial \psi}{\partial x}. \tag{2.27}$$

The initial atmosphere containing the flux sheet is computed in Cartesian coordinates using the numerical methods described in Steiner et al. (1986). The iterative method starts by specifying an initial magnetic field configuration and the radius of the tube at the base. The description of the method is provided in Appendix A.

We construct two atmospheric models with a temperature profile which are very similar to a photosphere and a chromosphere. The resultant field configuration has a sharp interface across which the field drops rapidly though continuously to a small value unlike a potential field which fans out and occupies the entire domain as soon as it emerges from the bottom boundary. This region with a very small magnetic field (of the order of a few Gauss) in the case of non potential field is the ambient medium.

2.4.1 PHOTOSPHERE

For the case of a photosphere we model the atmosphere with the gas pressure as a function of height and field line (flux value), $p(\psi, z)$, given by,

$$p(\psi, z) = \begin{cases} \dfrac{p}{p_0}(p_0 + p_2\psi^2) & \text{if} \quad 0 \le \psi \le \psi_1, \\ \dfrac{p}{p_0}(a(\psi - \psi_1)^n + b(\psi - \psi_1)^2 + c(\psi - \psi_1) + d) & \text{if} \quad \psi_1 < \psi < \psi_2, \\ \dfrac{p}{p_0}(p_0 + \dfrac{B_0^2}{8\pi}) & \text{if} \quad \psi_2 \le \psi \le \psi_{\max}, \end{cases} \tag{2.28}$$

where the constants a, b, c, and d are chosen such that the pressure and its first derivative with respect to ψ is a continuous function of ψ and where we choose $n = 8$ so that, we get a pressure profile at $z = 0$ as shown in Fig. 2.3.

Furthermore, B_0 is the magnetic field strength on the axis of the flux sheet at the reference height $z = 0$.

The pressure, p is defined as,

$$p = p_0 \exp\left[- \int_0^z \frac{\tilde{\mu} g}{\mathcal{R} T(z)} dz \right], \tag{2.29}$$

where $\tilde{\mu}$ is the mean atomic weight. The integration carried along the surface of constant ψ. We specify T(z), the temperature as a function of height by an analytical function of the form

$$T(z) = T_0 + \alpha \tanh(\gamma z), \tag{2.30}$$

where α and γ are constants. With an appropriate choice of T_0, α and γ we get a photospheric temperature profile as shown in Fig. 2.4. Initially the temperature drops rapidly

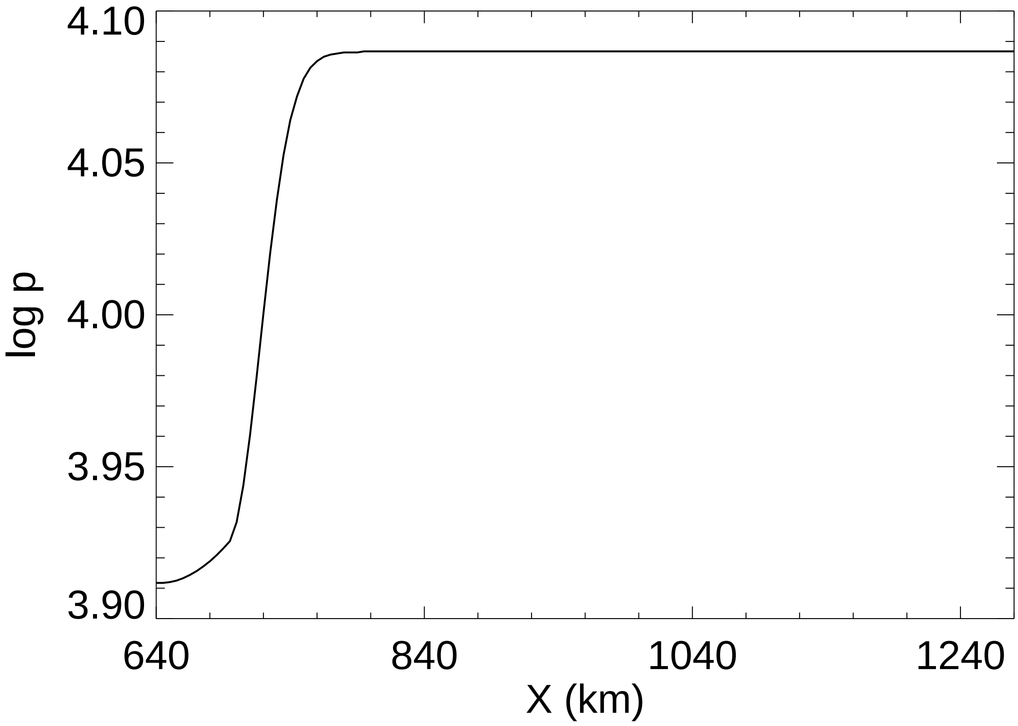

Figure 2.3: Pressure profile as a function of horizontal distance x at $z = 0$ km for a magnetohydrostatic flux tube model

from 10 500 K at the bottom boundary to 6 300 K at $z = 0$ km, then slowly decreases and plateaus at 4 000 K.

Having defined the pressure distribution through Eqs. (2.28 - 2.30), the equation of motion along each field line is given by:

$$\boldsymbol{B} \cdot [\nabla p - \rho \mathbf{g}] = 0, \tag{2.31}$$

which enables us to determine the density, ρ. The electric current density, $\boldsymbol{J}$ is calculated according to,

$$\boldsymbol{J} = \frac{1}{B^2} \boldsymbol{B} \times [\nabla p - \rho \boldsymbol{g}], \tag{2.32}$$

which reduces to:

$$j_y = \left. \frac{\partial p}{\partial \Psi} \right|_z . \tag{2.33}$$

The new magnetic field configuration can be calculated from the current density using the

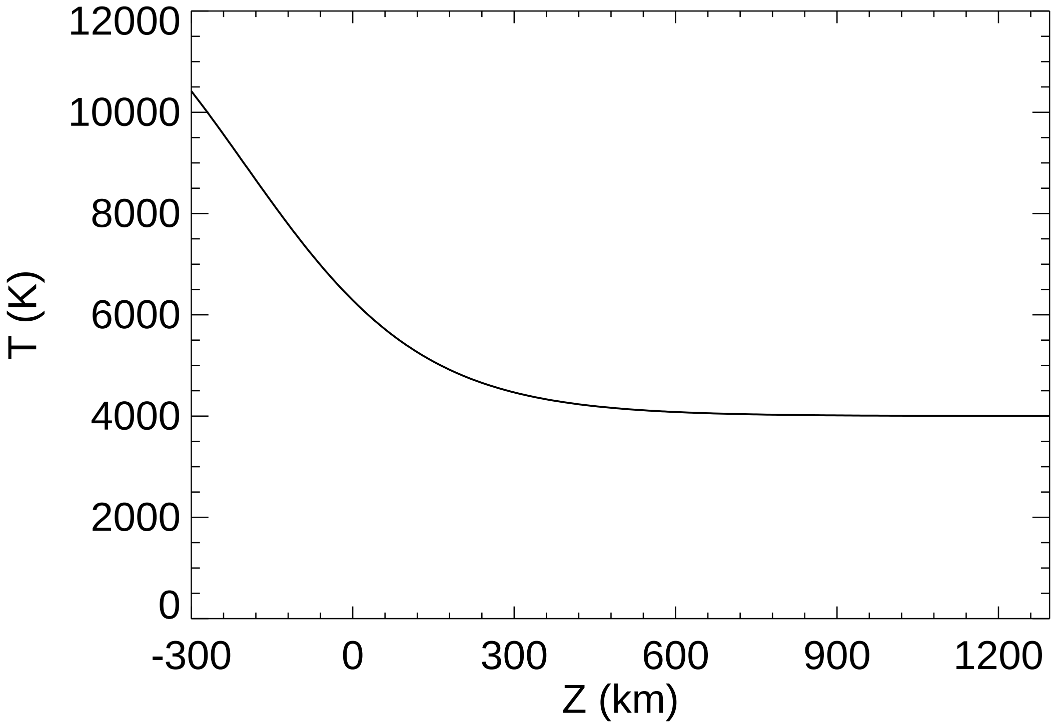

Figure 2.4: Temperature as a function of height for the photospheric model

Grad-Shafranov equation (Grad and Rubin (1958); Shafranov (1966)),

$$\frac{\partial^2 \psi}{\partial x^2} + \frac{\partial^2 \psi}{\partial z^2} = \mu j_y. \tag{2.34}$$

The above elliptic partial differential equation can be solved using standard numerical methods with appropriate boundary conditions. In practice we solve Eq. (2.34) on a computational domain that consists of only half of the flux sheet (in view of the axial symmetry) with horizontal and vertical extensions of 640 km and 1 600 km, respectively. The bottom boundary is at $z = -300$ km. This domain is discretized on a equidistant rectangular mesh with a spacing of 5 km. The left side of the domain corresponds to the axis of the flux sheet. The value of ψ is prescribed at the left and the right boundaries. At the top and bottom boundaries we use the Neumann condition $\partial\psi/\partial z = 0$, assuming that the horizontal field component vanishes at these two boundaries. We calculate cases corresponding to different field strengths (at $z = 0$) ranging between 1000 G to 1600 G, on the axis of the sheet.

In Fig. 2.5, the magnetic field lines for case with (a) 1000 G and (b) 1600 G are shown along with their respective $\beta = 1$ layer. The plasma β is defined as the ratio of the gas pressure and the magnetic pressure given as,

$$\beta = \frac{p}{B^2/2\mu} \tag{2.35}$$

For the weaker field case, the $\beta = 1$ layer lies well above the bottom boundary. Any field line originating from the bottom eventually crosses this layer, dividing the flux tube into two regions: viz. a lower region with $\beta > 1$ and the upper region with the $\beta < 1$. We find that the flux tube base is located in a high β region. On the other hand, in the case of a stronger field (1600 G), the $\beta = 1$ layer traces the boundary of the flux tube. Here we find that the whole flux tube is in a $\beta < 1$ region, whereas the ambient medium is a high β plasma. Figure 2.6 shows the variation of pressure with height for the two cases. The solid curve represents the pressure on the axis and the dashed curve represents the ambient medium. A stronger drop in pressure within the flux tube as a result of a stronger magnetic filed is evident in the case of 1600 G.

The variation of the magnetic field strength with height on the axis and in the ambient medium is shown in Fig. 2.7. In both cases, the magnetic field drops to a uniform value within the flux tube. In the ambient medium, the field strength in the lower part is negligible, but with height settles down to the same uniform value as that of the flux tube. The horizontal variation of the horizontal and vertical components of magnetic field at three different heights, $z = 0$ km (solid curve), 500 km (dotted curve), and 1000 km (dashed curve) are shown in Figs. 2.8 & 2.9. The horizontal component of the field at $z = 0$ km is close to zero, hence the field is almost vertical at this level. The flux tube at this height has a vertical component of the magnetic field that drops sharply to the ambient value in horizontal direction, confining it to a narrow region with a width of about 320 km. The flux tube has expanded to entirely cover the full horizontal extent at a height of $z = 500$ km and above.

The equilibrium parameters of the two model is summarized in Table 2.4.1. The values of the physical quantities at the sheet axis and ambient medium are shown with the numbers in first row of each quantity corresponding to the top boundary ($z = 1300$ km) and the numbers in the second row corresponding to the bottom boundary ($z = 0$ km). The plasma β at the tube axis at the base is 2.1 for the 1000 G case and 0.2 for the 1600 G case. The sound speed (c_s) and the Alfvén speed (v_A) are defined as,

$$c_s = \sqrt{\frac{\gamma p_0}{\rho_0}} \tag{2.36}$$

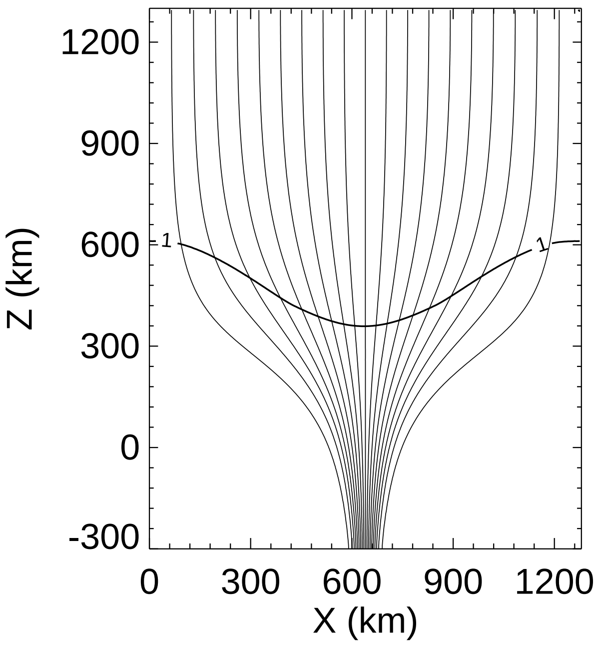

a) 1000 G

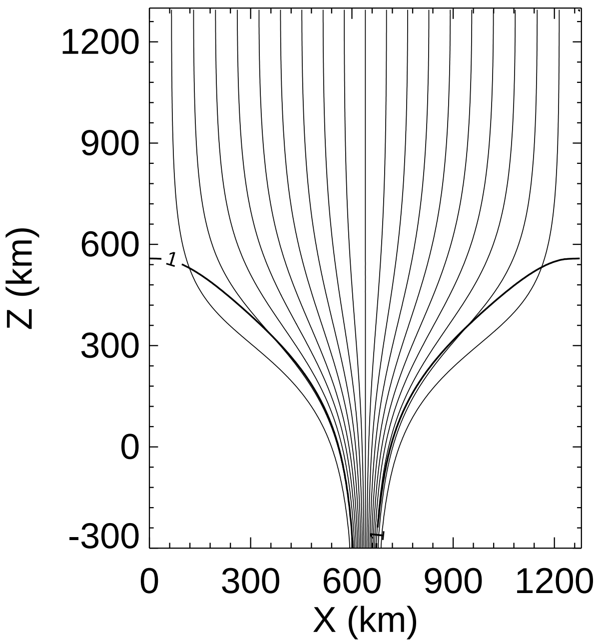

b) 1600 G

Figure 2.5: Field lines of photospheric magnetic flux tubes with field strength of 1000 G and 1600 G at the axis. The bold curve shows $\beta = 1$ contour

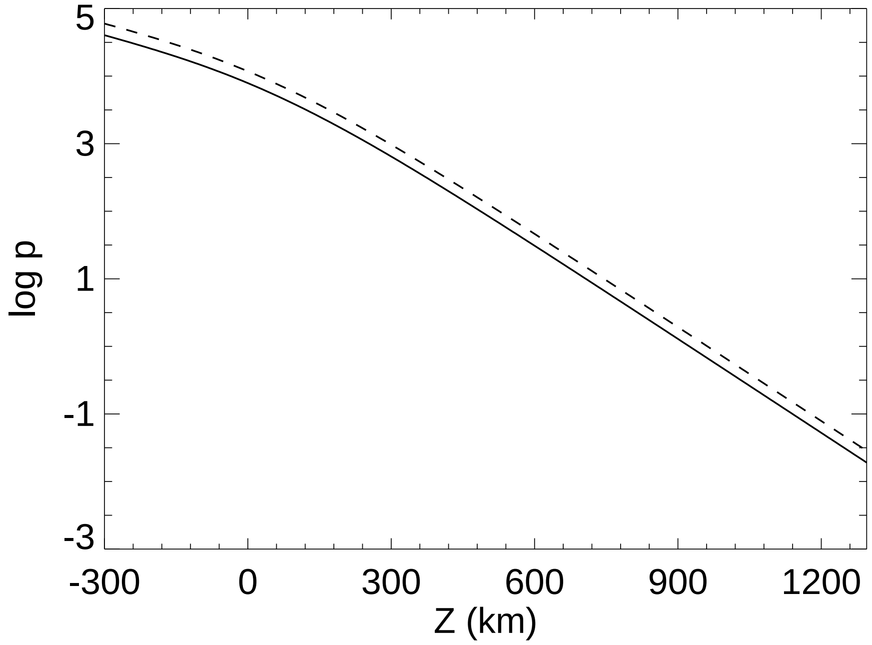

a) 1000 G

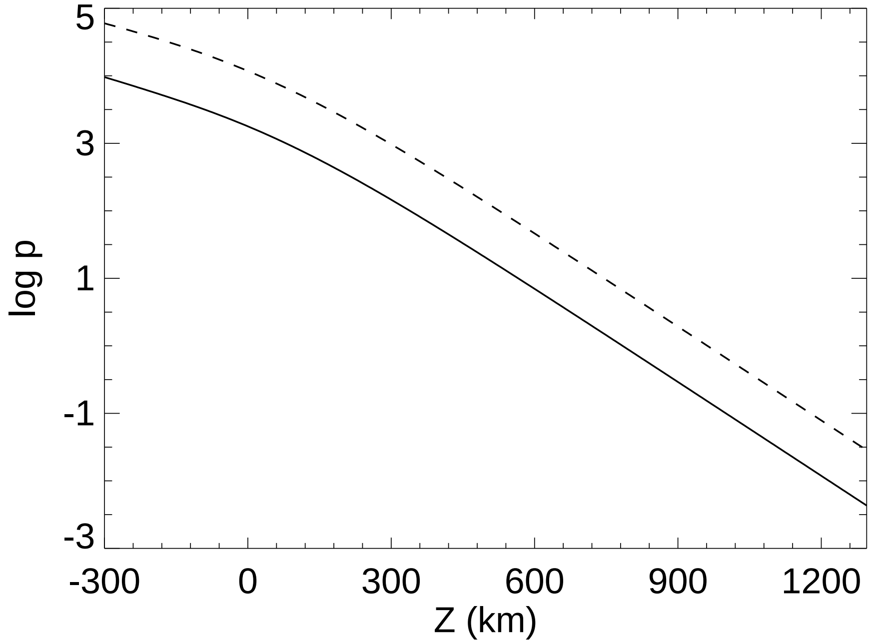

b) 1600 G

Figure 2.6: Pressure as a function of height on the axis (solid curve) and in the ambient medium (dashed curve) of a photospheric magnetic flux tubes with field strength of 1000 G and 1600 G at the axis at $z = 0$.

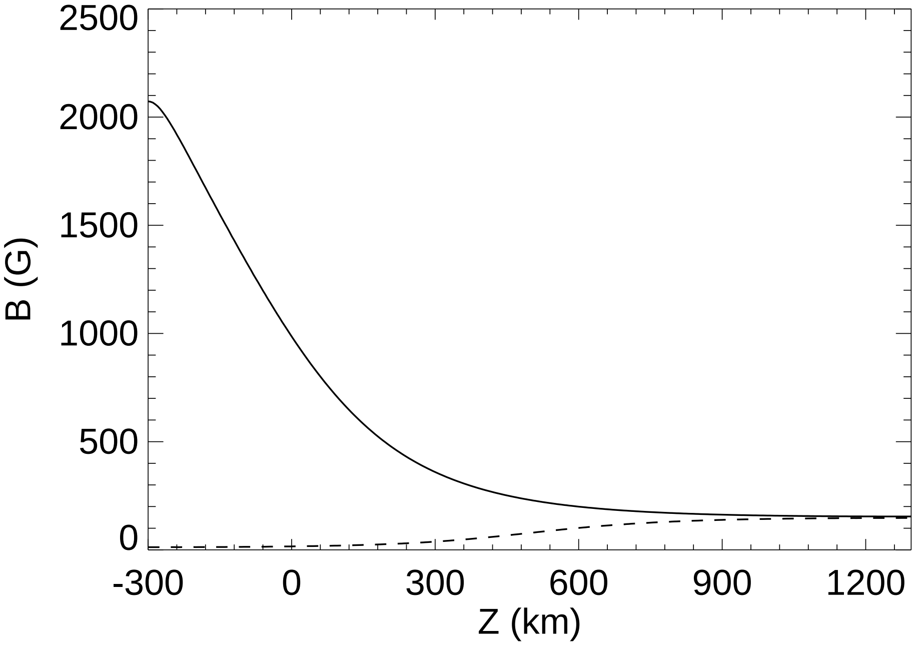

a) 1000 G

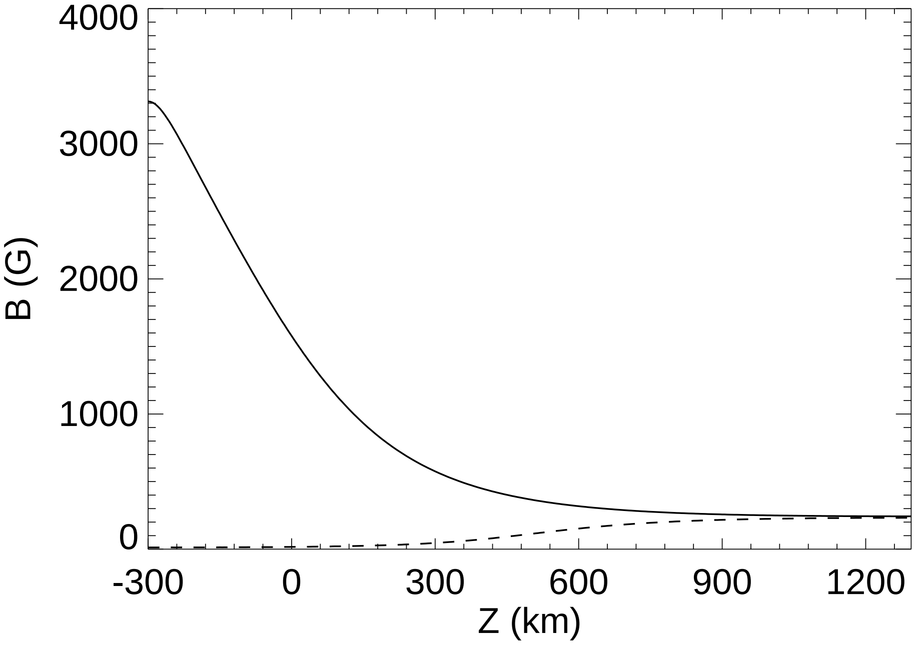

b) 1600 G

Figure 2.7: Magnetic field strength as a function of height on the axis (solid curve) and in the ambient medium (dashed curve) of a photospheric magnetic flux tubes with field strength of 1000 G and 1600 G at the axis at $z = 0$.

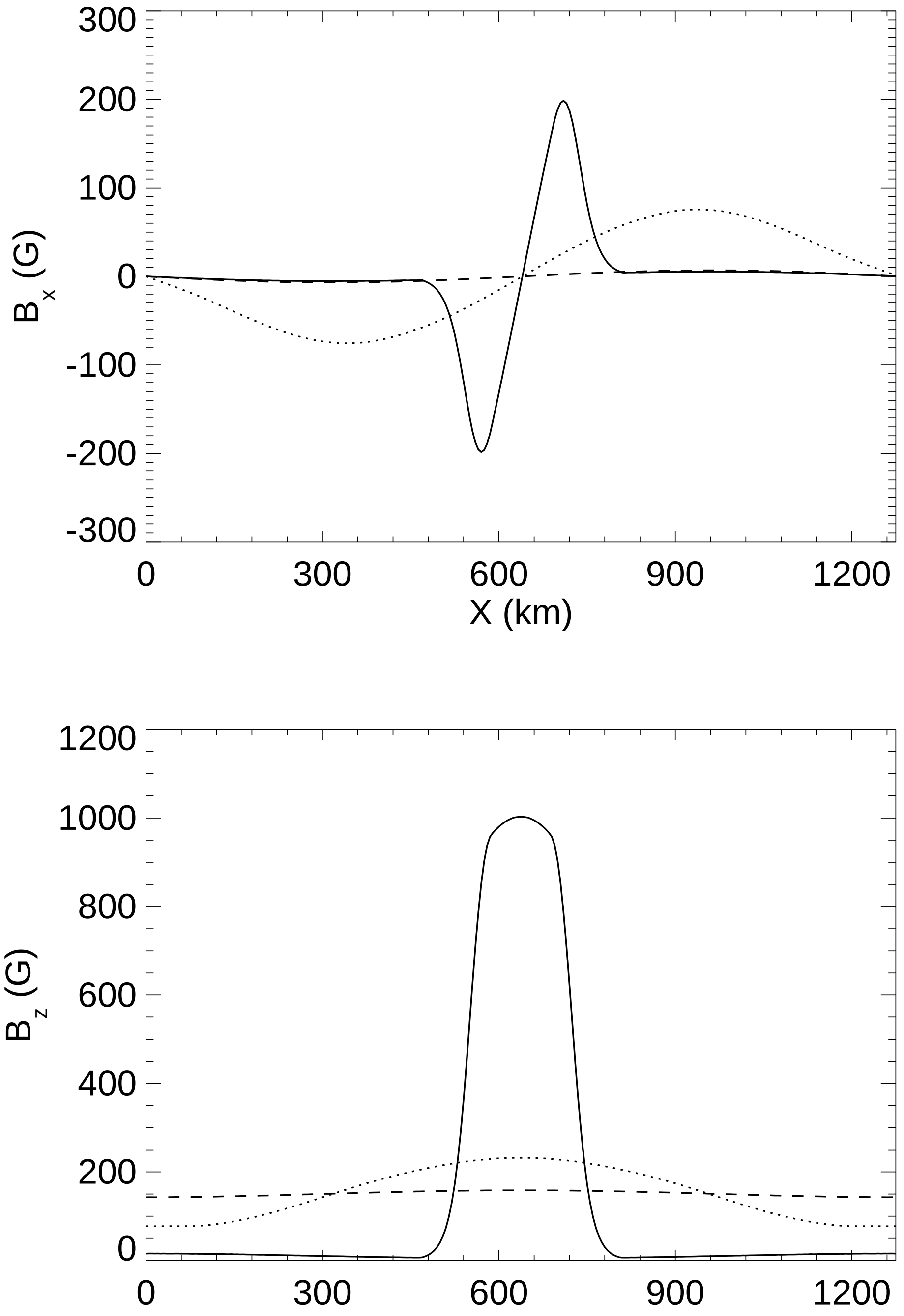

Figure 2.8: B_x (top) and B_z (bottom) components of the magnetic field as a function of horizontal distance at the following heights: $z = 0$ km (solid curve), 500 km (dotted curve), and 1000 km (dashed curve) of a photospheric magnetic flux tubes with field strength of 1000 G on the axis at $z = 0$.

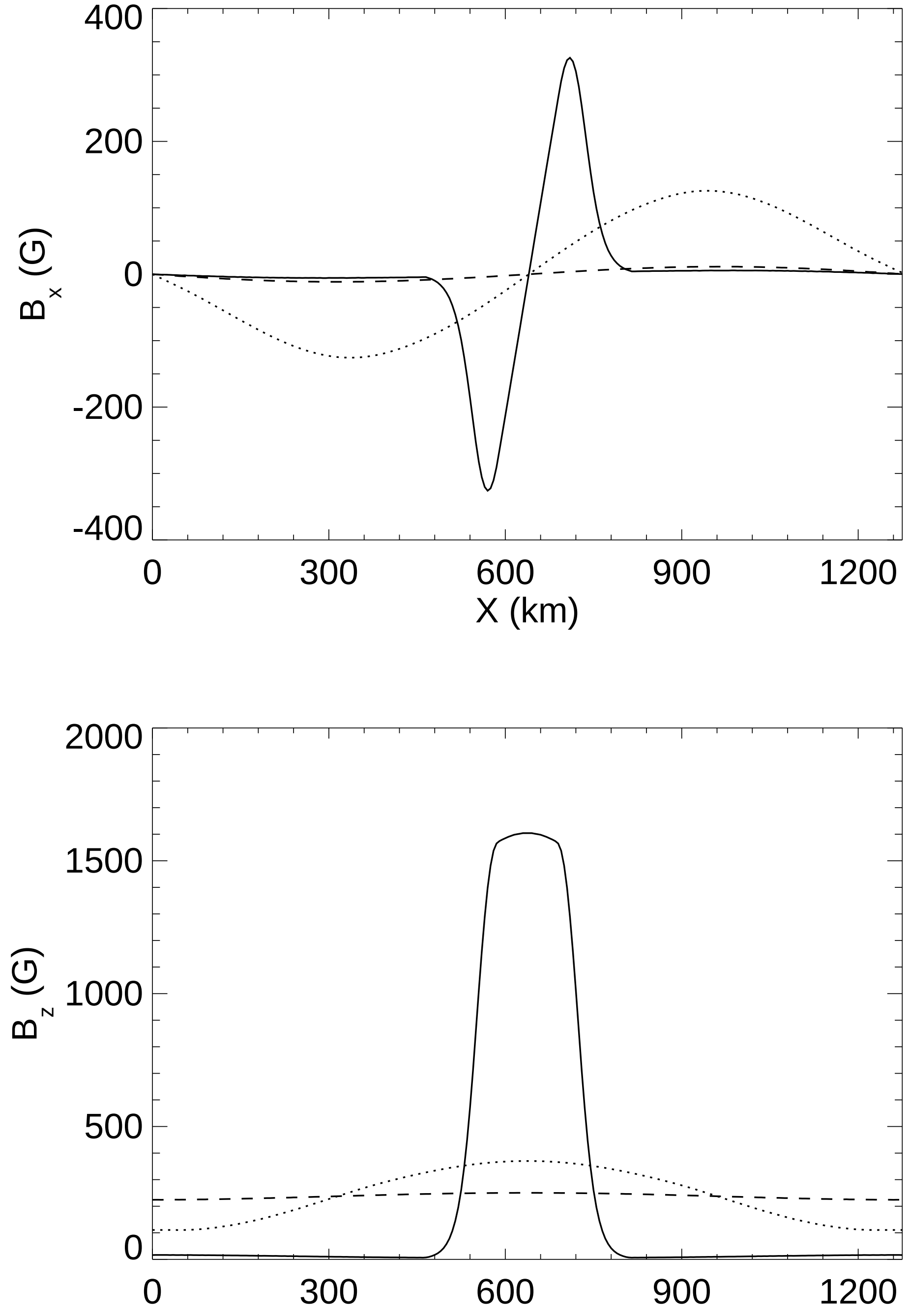

Figure 2.9: B_x (top) and B_z (bottom) components of the magnetic field as a function of horizontal distance at the following heights: $z = 0$ km (solid curve), 500 km (dotted curve), and 1000 km (dashed curve) of a photospheric magnetic flux tubes with field strength of 1600 G on the axis at $z = 0$.

$$v_A = \frac{B_0}{\sqrt{\mu \rho_0}} \tag{2.37}$$

where, p_0, ρ_0, and B_0 are the equilibrium values of pressure, density and magnetic field strength respectively. In the above models, the sound speed drops from 8.2 km s^{-1} at z = 0 km to 6.5 km s^{-1} at a height of z = 1300 km. The Alfvén speed at the base for the weak field case is 6.3 km s^{-1}, which is less than the sound speed in that region. However for the strong field case (since it has a low β at this level), the Alfvén speed is larger. For both models, Alfvén speed rapidly increases with height and has a value that is two orders of magnitude greater at the top boundary compared to the base.

Table 2.2: Equilibrium model parameters for the photospheric 1000 G and 1600 G flux sheets. The numbers in the first row of each quantity corresponds to the top boundary (z = 1300 km) and the numbers in the second row corresponds to the bottom boundary (z = 0 km).

Physical quantity	1000 G		1600 G	
	Sheet Axis	Ambient medium	Sheet Axis	Ambient medium
Temperature [K]	4001	4001	4001	4001
	6342	6342	6342	6342
Density [kg m^{-3}]	7.4×10^{-10}	1.1×10^{-9}	1.7×10^{-10}	1.1×10^{-9}
	2.0×10^{-4}	3.0×10^{-4}	4.5×10^{-5}	3.0×10^{-4}
Pressure [Pa]	2×10^{-2}	3×10^{-2}	4×10^{-3}	2.9×10^{-2}
	8.2×10^{3}	1.2×10^{4}	1.8×10^{3}	12.2×10^{3}
Sound speed [km s^{-1}]	6.5	6.5	6.5	6.5
	8.2	8.2	8.2	8.2
Alfvén speed [km s^{-1}]	504	394	1672	620
	6.3	0.1	21	0.08
Magnetic field [G]	154	147	243	232
	1003	16	1604	16
Plasma β	2.0×10^{-4}	3.4×10^{-4}	1.9×10^{-5}	1.4×10^{-4}
	2.1	1.3×10^{4}	0.2	1.2×10^{4}

The choice of a strong temperature gradient in the lower part of the model (below the photospheric base) is used in order make realistic comparison with spectral lines. In Chapter 5, we use this photospheric model to study the effect of wave propagation on spectral lines, by synthesizing Stokes profiles of a set of Fe I lines.

2.4.2 CHROMOSPHERE

We allow for an increase of temperature in the chromosphere, where the gas pressure as a function of height is modelled as,

$$p(\psi, z) = \begin{cases} (p_0 + p_2\psi^2)\dfrac{p_\mathrm{p} + p_\mathrm{c}}{p_0} & \text{if} \quad 0 \le \psi \le \psi_1, \\ \Big((a(\psi - \psi_1)^n + b(\psi - \psi_1)^2 + c(\psi - \psi_1) + d\Big)\dfrac{p_\mathrm{p} + p_\mathrm{c}}{p_0} & \text{if} \quad \psi_1 < \psi < \psi_2, \\ (p_0 + \dfrac{B_0^2}{8\pi})\dfrac{p_\mathrm{p} + p_\mathrm{c}}{p_0} & \text{if} \quad \psi_2 \le \psi \le \psi_\mathrm{max}, \end{cases} \tag{2.38}$$

where the constants a, b, c, and d are chosen such that the pressure and its first derivative with respect to ψ is a continuous function of ψ and as before we choose $n = 8$.

The quantities p_p, p_c and p_0 are defined as,

$$p_\mathrm{p} = p_{0,\mathrm{p}} e^{-z/H_\mathrm{p}}, \tag{2.39}$$

$$p_\mathrm{c} = p_{0,\mathrm{c}} e^{-z/H_\mathrm{c}}, \tag{2.40}$$

$$p_0 = p_{0,\mathrm{p}} + p_{0,\mathrm{c}}, \tag{2.41}$$

where H_p and H_c are the photospheric pressure scale height and the chromospheric scale height respectively. We choose $H_\mathrm{p} = 110$ km and $H_\mathrm{c} = 220$ km. Having defined the pressure distribution, the density distribution along the field line can be calculated according to Eq. (2.31), and with it the temperature. The resulting temperature as a function of height is show in Fig. 2.10.

Similar to the photospheric flux tube case, new magnetic field configuration can be calculated from the resulting current density (see Eq. 2.33) using the Grad-Shafranov equation given by Eq. (2.34). The equation is solved on a computational domain consisting of only half of the flux sheet which has horizontal and vertical extensions of 640 km and 1 600 km respectively. With the same type of discretization and boundary conditions as for a photospheric flux tube considered earlier, we treat two different cases corresponding to field strengths (at $z = 0$) of 800 G and 1 600 G, on the axis of the sheet. In order to study the effect of the boundary between the flux tube and the ambient medium, for each of these cases we consider three boundary widths 20 km, 40 km and 80 km at the reference height $z = 0$. These widths can be obtained by choosing appropriate values of ψ_1 and ψ_2 in Eq. (2.38).

The vertical component of the magnetic field at $z = 0$ is shown in Fig. 2.11 for the strong and moderate field cases. For the sharp interface (red curve) the vertical component

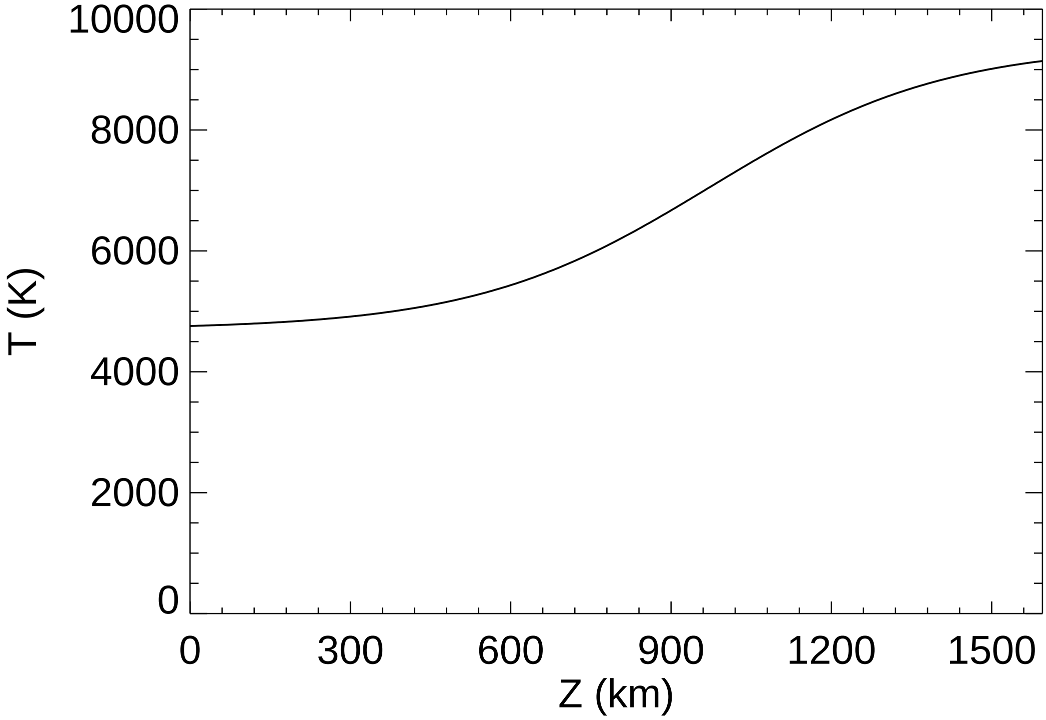

Figure 2.10: Temperature as a function of height for the chromospheric model

of the magnetic field component drops sharply, whereas in the case of a wide interface (blue curve) the field decreases smoothly. In the strong field case, the field strength at the axis of the sheet is 1 600 G for both sharp and wide interfaces. A similar plot is obtained for the moderate field case, where the field strength at the axis of the flux sheet is 800 G.

The magnetic field configuration along with the $\beta = 1$ contour for the above mentioned four cases is shown in fig. 2.12. The left panel shows the case with a field strength of 800 G at the tube axis, and the right panel shows the 1600 G case. The top panel in each column represents the field lines for a diffuse flux tube, and the bottom panel shows a sharp flux tube. The $\beta = 1$ layer is well above the bottom boundary in the weak field case, dividing the flux tube into a region with $\beta > 1$ (below $\beta = 1$)and a region with the $\beta < 1$ (above $\beta = 1$). In the case of a diffuse tube, the field lines emerge from a wider area compared to a sharp interface. This is due to the spreading of the magnetic flux over a wider region in the case of the diffuse tube. In the strong field case, with a sharp interface, the whole flux tube is in a $\beta < 1$ region, and only the ambient medium has a high β plasma. But, this is not the case with wider interface, since few outer field lines at the base are still in the high β regime. The effect of these in the generation and propagation

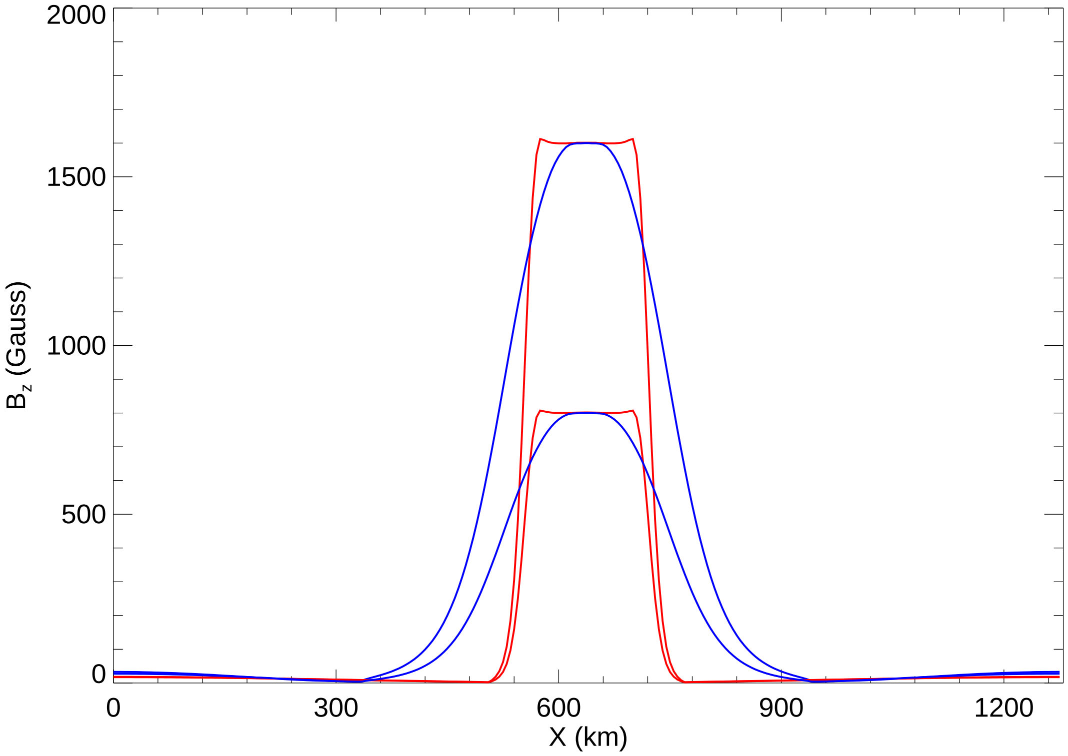

Figure 2.11: Vertical component of the magnetic field at the base of the flux sheet, $z = 0$. Red and blue curves correspond to field configurations with a sharp and a wide interface to the weak-field surroundings, respectively. Each configuration is subdivided into a case of moderate field-strength with $\max(B_z) = 800$ G and and a case of strong field with $\max(B_z) = 1600$ G.

of waves will be discussed in the next chapter.

The characteristic properties of the two models are summarized in Table 2.3 The numbers in the first row of each quantity corresponds to the top boundary ($z = 1\,600$ km) and the numbers in the second row corresponds to the bottom boundary($z = 0$ km). The temperature increases monotonically from 4758 K in the photosphere to 9142 K in the chromosphere corresponding to the sound speed variation from 7.1 km s^{-1} to 13.5 km s^{-1}. The density and pressure at the axis of the tube is the same for both the cases. We should mention that the ambient magnetic field is weak (of the order of few tens of Gauss). As we go higher up in the atmosphere the flux tube expands and become uniform near the top with a average field strength of 118 G and 227 G for the moderate and strong field cases, respectively. The plasma β on the tube axis is 1.69 and 0.42 at the base for the moderate and strong field cases.

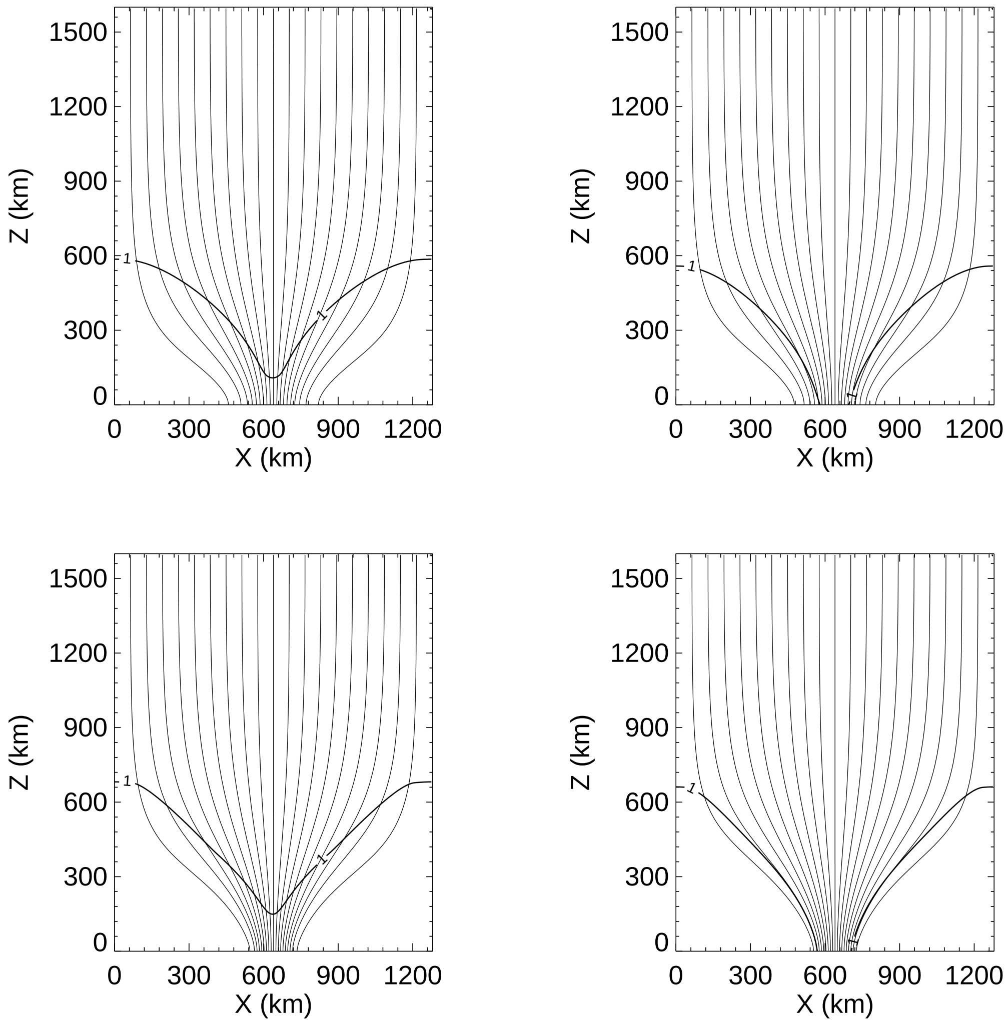

a) 800 G

b) 1600 G

Figure 2.12: Field lines of chromospheric magnetic flux tubes with field strength of 800 G and 1600 G at the axis. The bold curve shows $\beta = 1$ contour. The top two panels are for the case with a wide interface. The bottom two panels are for the sharp interface

The chromospheric model is constructed to study the wave dynamics and energy transport in magnetohydrostatic flux tubes. These discussions will be the topic of the following chapter. Chapter 3 will discuss the wave dynamics in these flux tubes. In Chapter 4, a quantitative estimate of the energy that these waves carry are discussed.

Table 2.3: Equilibrium model parameters for the the moderate and strong flux sheets. The numbers in the first row of each quantity corresponds to the top boundary (z = 1600 km) and the numbers in the second row corresponds to the bottom boundary (z = 0 km).

Physical quantity	Moderate field		Strong field	
	Sheet Axis	Ambient medium	Sheet Axis	Ambient medium
Temperature [K]	9142	9142	9142	9142
	4758	4758	4758	4758
Density [kg m^{-3}]	1.2×10^{-9}	2.4×10^{-9}	1.2×10^{-9}	6.0×10^{-9}
	1.4×10^{-4}	2.7×10^{-4}	1.4×10^{-4}	6.7×10^{-4}
Pressure [Pa]	0.13	0.27	0.13	0.66
	4.2×10^{3}	8.3×10^{3}	4.2×10^{3}	20.6×10^{3}
Sound speed [km s^{-1}]	13.5	13.5	13.5	13.5
	7.1	7.1	7.1	7.1
Alfvén speed [km s^{-1}]	304	212	582	259
	6	0.9	12	0.6
Magnetic field [G]	119	117	229	225
	801	17	1601	18
Plasma β	2.0×10^{-3}	5.0×10^{-3}	6.0×10^{-4}	3.0×10^{-3}
	1.7	7.4×10^{3}	0.4	1.6×10^{4}

2.5 STABILITY ISSUES

The flux tube models discussed above are constructed by solving the Grad-Shafranov equation (Eq. 2.34) for magnetohydrostatics. The solution requires that the hydrostatic balance has to be maintained on each and every field line. The discretization of the computational domain into grids of finite sizes results in discontinuous jumps. Hence, in practice the solution is very sensitive to small numerical perturbations and can thereby become unstable. The stability of the above models were checked by solving the time dependent MHD equations without any perturbations. We find that the the maximum velocities in the entire computational domain increased as a function of time and were of the order of few km s^{-1} during the entire span of the simulation. To cope with this problem we subtract these velocities from the perturbed solution in order to remove the effect of deviation from hydrostatic equilibrium. Figure 2.13 shows the maximum velocity in the domain as a function of time. The dashed curve shows the solution without any initial perturbation and the continuous curve shows the maximum velocity with a excitation of V_{max} = 750 m s^{-1}.

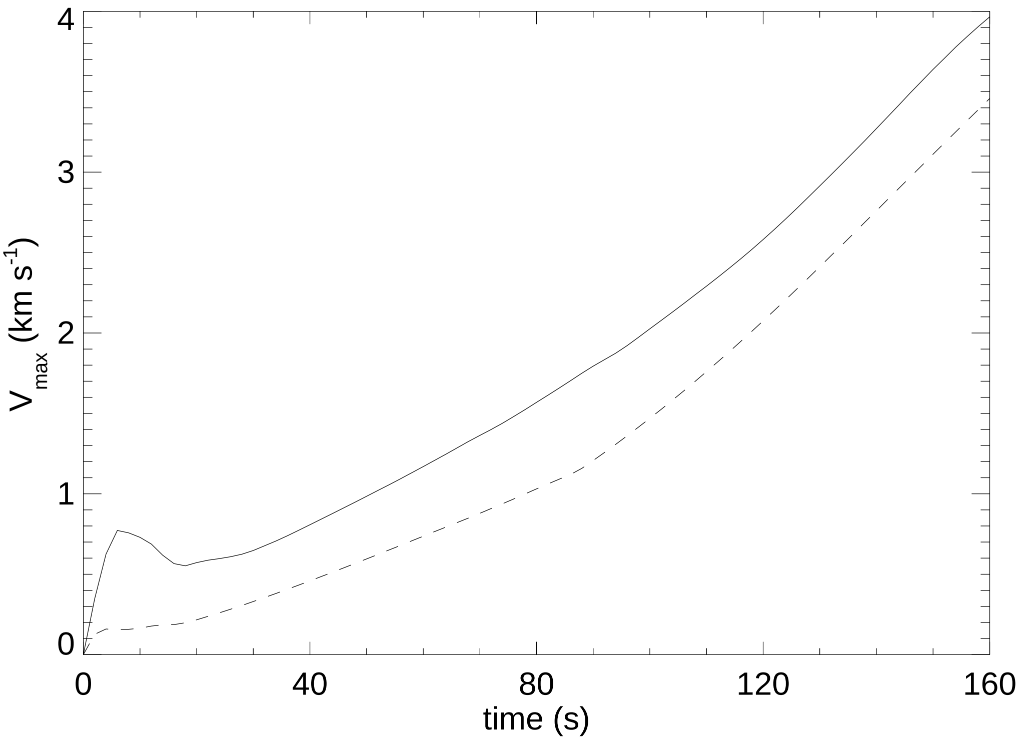

Figure 2.13: Maximum velocity as a function of time. The dashed curve shows the solution without perturbation and the continuous curve shows the maximum velocity with a impulsive excitation of V_{max} = 750 m s^{-1}.

CHAPTER 3

DYNAMICS*

"*A light shower of large raindrops on the surface of a pond...*", is how Musman & Rust (1970) poetically described the quiet solar surface. The solar surface shows a uniform distribution of oscillations with a period of 5 minutes (Leighton et al. 1962). These oscillations typically last for four or five periods with a velocity amplitude of around 1 km s^{-1}. These 5-min photospheric waves are driven by granular flows associated with the underlying convection. Different models were put forward to explain these "five minute" oscillations (for a review see Stein & Leibacher 1974). The Lighthill mechanism[†] (Lighthill 1952) is generally considered the most promising candidate for their generation through turbulence in the solar convection zone. The Lighthill mechanism was developed for the generation of acoustic waves by turbulent motions in a homogeneous medium. The effect of magnetic fields on the waves generated by turbulence were studied by Kulsrud (1955) and Parker (1964). The Lighthill theory was extended to stratified atmosphere by Stein (1967), making it more applicable to the solar convection zone.

Small scale magnetic elements appear as bright features especially in images taken in the G-band[‡] or in the cores of other photospheric lines and also in the wings of Ca II H 3968 Å and K 3933 Å. Despite earlier observations suggesting that these brightening appears independent of the magnetic fields, it was later confirmed (Berger & Title 2001) that these bright points are always magnetic in nature. The magnetic structure of these

---

[*] Part of publications: Hasan et al. (2006), Steiner et al. (2007), Vigeesh et al. (2009)

[†] Its ironic that Lighthill did not realize that his theory was used in Solar context. Quoting Lighthill,

> *"I developed that theory solely to understand the noise of jet aircraft, and realized that it had been applied to solar physics only two months ago"* (Lighthill 1967)

[‡] The G-band is a region of solar spectrum centred around 4305 Å, having absorption lines from CH, Fe, Ca and other trace elements

network bright points has already been discussed in Chapter 2 (for more details see the reviews by Muller 1983, 1985). During the formation of these bright points, the magnetic field associated with them dynamically interacts with the surrounding convective granular pattern (Muller et al. 1989). Owing to the dynamic nature of the regions in which these magnetic features exist, waves can be excited in them. Their formation which appears as brightening in filtergram images is followed by a highly dynamical state in which their motion is confined to the intergranular lanes. During their lifetime in these intergranular lanes, these bright points undergo various morphological changes like fragmentation and merging on timescales of 100 s or even less (Berger & Title 1996). The brightening seen in G-band images, also referred to as G-band bright points, or GBPs, were studied extensively by Berger & Title (2001). They reported a very strong spatial, temporal and morphological relationship between isolated GBPs and the corresponding structures seen in the magnetograms taken at 0.3″ resolution.

3.1 WAVES

Waves permeate the entire Sun. The solar atmosphere is abundant with different types of waves. These waves owe there existence to the processes taking place in the highly dynamic photosphere. The main source of waves is the magneto-convection and the global p modes, which interact with the small scale structures in the photosphere and excite waves.

As we have shown in Chapter 2, to a first approximation the magnetic field in the lower part of the solar atmosphere can be considered as frozen in to the plasma and hence we can use ideal MHD to describe the behaviour of this medium. The theoretical formulation of MHD wave investigation starts with the basic MHD equations (described in Chapter 2). The equations are linearised about a time independent ($\partial/\partial t = 0$) or static background characterized by equilibrium values of density (ρ_0), pressure (p_0) and magnetic field ($\boldsymbol{B_0}$). Time dependent perturbations of density (ρ_1), velocity ($\mathbf{v}_1$), pressure (p_1) and magnetic field strength ($\boldsymbol{B_1}$) about the equilibrium, given as,

$$\rho = \rho_0 + \rho_1, \mathbf{v} = \mathbf{v}_1, p = p_0 + p_1, \boldsymbol{B} = \boldsymbol{B}_0 + \boldsymbol{B}_1 \tag{3.1}$$

are inserted into the basic equations. Neglecting second and higher order terms in the perturbed quantities, the resulting linearised equations are,

$$\frac{\partial \rho_1}{\partial t} + (\mathbf{v}_1 \cdot \boldsymbol{\nabla})\rho_0 + \rho_0(\boldsymbol{\nabla} \cdot \mathbf{v}_1) = 0, \tag{3.2}$$

$$\rho_0 \frac{\partial \boldsymbol{v}_1}{\partial t} = -\boldsymbol{\nabla} p_1 - \rho_1 g + (\boldsymbol{\nabla} \times \boldsymbol{B_1}) \times \frac{\boldsymbol{B_0}}{\mu}, \tag{3.3}$$

$$\frac{\partial \boldsymbol{B_1}}{\partial t} = \boldsymbol{\nabla} \times (\boldsymbol{v}_1 \times \boldsymbol{B_0}), \tag{3.4}$$

$$\frac{\partial p_1}{\partial t} + (\boldsymbol{v}_1 \cdot \boldsymbol{\nabla}) p_0 - c_s^2 (\frac{\partial \rho_1}{\partial t} + (\boldsymbol{v}_1 \cdot \boldsymbol{\nabla}) \rho_0) = 0, \tag{3.5}$$

$$\nabla \cdot B_1 = 0 \tag{3.6}$$

where

$$c_s = \sqrt{\frac{\gamma p_0}{\rho_0}} \tag{3.7}$$

is the sound speed, the characteristic speed with which pressure disturbances travel. By differentiating Eq. (3.3) with respect to time and using Eq.(3.2),(3.4) and (3.5), we finally get a wave equation for the velocity (e.g. Priest 1982),

$$\frac{\partial^2 \boldsymbol{v}_1}{\partial t^2} = c_s^2 \boldsymbol{\nabla}(\boldsymbol{\nabla} \cdot \boldsymbol{v}_1) - (\gamma - 1)\boldsymbol{g}(\boldsymbol{\nabla} \cdot \boldsymbol{v}_1) - \boldsymbol{g} \cdot \boldsymbol{\nabla} \boldsymbol{v}_1 + [\boldsymbol{\nabla} \times (\boldsymbol{\nabla} \times (\boldsymbol{v}_1 \times \boldsymbol{B_0}))] \times \frac{\boldsymbol{B_0}}{\mu \rho_0} \tag{3.8}$$

Assuming perturbations in the form of travelling waves of the form

$$\boldsymbol{v}_1(\boldsymbol{r}, t) = \boldsymbol{v}_1 e^{i(\boldsymbol{k} \cdot \boldsymbol{r} - \omega t)}, \tag{3.9}$$

where ω is the frequency and $\boldsymbol{k}$ is the wavenumber, an equation that relates these two quantities in the form of a *dispersion* relation is derived by substituting, $\partial/\partial t$ with $-i\omega$ and ∇ with $i\boldsymbol{k}$ in Eq. (3.8). The dispersion relation for this case then becomes,

$$\omega^2 \boldsymbol{v}_1 = c_s^2 \boldsymbol{k}(\boldsymbol{k} \cdot \boldsymbol{v}_1) + i(\gamma - 1)\boldsymbol{g}(\boldsymbol{k} \cdot \boldsymbol{v}_1) + i\boldsymbol{g} \cdot \boldsymbol{k} \boldsymbol{v}_1 + [\boldsymbol{k} \times (\boldsymbol{k} \times (\boldsymbol{v}_1 \times \boldsymbol{B_0}))] \times \frac{\boldsymbol{B_0}}{\mu \rho_0} \tag{3.10}$$

The various wave modes on the Sun owe their existence to the different restoring forces present in the solar atmosphere. The three main driving forces are the gas pressure (first term in Eq. 3.10), gravitation (second and third terms) and magnetism (last term). These forces can act individually or simultaneously giving a multitude of wave phenomena.

SOUND WAVES: When the pressure gradient is the only restoring force acting to bring the system back to equilibrium, the waves generated are the sound waves. Sound waves owe their existence to the compressibility of the medium. Retaining only the first term (since $g = 0$ and $B_0 = 0$) in the RHS of Eq. (3.10), and taking a scalar product of the equation with $\boldsymbol{k}$ and since in general $\boldsymbol{\nabla}\cdot\boldsymbol{v}_1$ (and so $\boldsymbol{k}\cdot\ \boldsymbol{v}_1)\neq 0$, the dispersion relation for sound waves can be written as,

$$\omega^2 = k^2 c_S^2. \tag{3.11}$$

The *phase velocity*, ω/k and the *group velocity* defined as $(\partial\omega/\partial k)$ are the same for an acoustic wave. If the phase speed is a function of k, the wave is said to be *dispersive*. Sound waves are *non-dispersive* since the phase velocity and the group velocity are the same.

MAGNETO-ACOUSTIC WAVES: The presence of magnetic field introduces more complexity through additional modes. When gas pressure and the magnetic force are present, in general there are three wave modes. Using Eq. (3.10), and neglecting gravity ($g = 0$), we get

$$\omega^2\boldsymbol{v}_1 = (c_S + v_A)^2(\boldsymbol{k}\cdot\boldsymbol{v}_1)\boldsymbol{k} + \boldsymbol{v}_A\cdot\boldsymbol{k}[(\boldsymbol{v}_A\cdot\boldsymbol{k})\boldsymbol{v}_1 - (\boldsymbol{v}_A\cdot\boldsymbol{v}_1)\boldsymbol{k} - (\boldsymbol{k}\cdot\boldsymbol{v}_1)\boldsymbol{v}_A], \tag{3.12}$$

where,

$$\boldsymbol{v}_A = \frac{\boldsymbol{B_0}}{\sqrt{\mu\rho_0}}, \tag{3.13}$$

is the Alfvén speed, the characteristic speed with which a perturbation in the magnetic field lines propagates.

If θ_{kB} is the angle between the direction of propagation ($\boldsymbol{k}$) of the wave and the equilibrium field ($\boldsymbol{B}_0$), then we see that Eq. (3.12) possess non-trivial solutions provided,

$$\begin{vmatrix} (c_S^2 + v_A^2)k^2sin^2\theta_{kB} + v_A^2k^2cos^2\theta_{kB} - \omega^2 & 0 & c_S^2k^4sin^2\theta_{kB}cos^2\theta_{kB} \\ 0 & v_A^2k^2cos^2\theta_{kB} - \omega^2 & 0 \\ c_S^2k^4sin^2\theta_{kB}cos^2\theta_{kB} & 0 & c_S^2k^2cos^2\theta_{kB} - \omega^2 \end{vmatrix} = 0. \tag{3.14}$$

Expanding the determinant we obtain the condition

$$(v_A^2k^2cos^2\theta_{kB} - \omega^2)(\omega^4 - \omega^2k^2(c_S^2 + v_A^2) + c_S^2v_A^2k^4cos^2\theta_{kB}) = 0, \tag{3.15}$$

which is satisfied if either,

$$\omega^2 = v_A^2k^2cos^2\theta_{kB}, \tag{3.16}$$

or

$$\omega^4 - \omega^2k^2(c_S^2 + v_A^2) + c_S^2v_A^2k^4cos^2\theta_{kB} = 0. \tag{3.17}$$

Equation (3.16), represents *Alfvén waves* propagating along $\boldsymbol{B_0}$. The density, and the pressure perturbations are constant for this mode.

We now consider Eq. (3.17) that describes the propagation of “magneto-acoustic waves (or magnetosonic waves)”. The two distinct solution of the above equation can be written as,

$$\omega/k = [\frac{1}{2}(c_S^2 + v_A^2) \pm \frac{1}{2}\sqrt{(c_S^4 + v_A^4 - 2c_S^2 v_A^2 \cos 2\theta_{kB})}]^{1/2}. \qquad (3.18)$$

The wave with the higher frequency is known as the *fast magnetoacoustic wave* whereas the one with the lower frequency is called the *slow magnetoacoustic wave*. The properties of these waves are described in the Table 3.1

Table 3.1: Properties of the different magneto-acoustic wave modes

		Region	
Wave mode	Propagation direction	High-β ($\beta > 1$)	Low-β ($\beta < 1$)
Slow mode	*closely along* $\boldsymbol{B_0}$	Magnetic tension $v_1 \perp \boldsymbol{k}$ v_A	Gas pressure $v_1 \parallel \boldsymbol{B_0}$ c_S
Intermediate Alfvén mode	*along* $\boldsymbol{B}_0$	Magnetic tension $v_1 \perp \boldsymbol{k}$ & $\boldsymbol{B_0}$ v_A	
Fast mode	*isotropic*	Gas pressure $v_1 \parallel \boldsymbol{k}$ c_S	Magnetic pressure $v_1 \parallel \boldsymbol{B_0}$ v_A

3.2 NUMERICAL SIMULATION

Time dependent numerical simulations aim at realistically describing the dynamical processes like flow, waves, oscillations and shocks that occur in a physical system. There are two different approaches for doing a numerical simulation: kinematical and dynamical. In a kinematical simulation, the induction equation is decoupled from the MHD equation in a way that, the evolution of the magnetic field is calculated from an initial velocity field. On the other hand, a dynamical simulation proceeds by simultaneously solving the coupled MHD equations. A dynamical simulation is more realistic in a sense that a multitude of different phenomenon can be studied in a single simulation. In this thesis, we adopt the dynamical approach.

A major step to explain the bright grain like features seen in Ca II H using numerical simulations started with the work of Carlsson & Stein (1997). The one dimensional radiation hydrodynamics simulations showed that the bright grains seen in Ca II H are due to shocks produced by acoustic waves. This was followed by non-radiative simulations of Rosenthal et al. (2002) and Bogdan et al. (2003), who studied wave propagation in two-dimensional stratified atmospheres in the presence of a magnetic field. This extensive work focused on more general aspects of waves in various magnetic structures to answer questions about the effect of magnetic topology in the network and internetwork regions on propagation of waves, excited by driving motions at the photospheric base. It was found that the fast and the slow magnetoacoustic waves are completely decoupled in regions of low and high-β plasma, and the important role was highlighted of the "magnetic canopy", the region that separates region of low-β and high-β. The coupling and transformation between various wave modes turns out to be restricted to this region. The thick flux sheets of Rosenthal et al. (2002) and Bogdan et al. (2003) were a somewhat idealized model for the network, since they assumed a potential magnetic field. Considering that the gas pressure, kinetic energy density, and the energy density of the magnetic field are all of similar magnitude in the photosphere, this assumption is probably not satisfied.

Cranmer & van Ballegooijen (2005) modelled the network as consisting of a collection of smaller flux tubes that are spatially separated from one another in the photosphere. Hasan et al. (2005) performed MHD simulations of wave generation and propagation in an individual magnetic flux sheet of such a collection and confirmed the existence of magneto-acoustic waves in flux sheets as a result of the interaction of these magnetic flux concentrations with the surrounding plasma. They used a non-potential field to model the network. They speculated that a well defined interface between the flux sheet and the ambient medium may act as an efficient source of acoustic waves to the surrounding plasma. In a later paper, Hasan & van Ballegooijen (2008) showed that the short period waves that are produced as a result of turbulent motions can be responsible for the heating of the network elements.

Cally (2005, 2007) provided linear magneto-acoustic-gravity dispersion relations for waves in a stratified atmosphere with a homogeneous, inclined magnetic field and discussed the process of mode transmission and mode conversion. Khomenko et al. (2008) presented results of nonlinear, two-dimensional, numerical simulations of magneto-acoustic wave propagation in the photosphere and chromosphere in small-scale flux tubes with internal structure. This work focussed on long period waves with periods of three to five minutes. Steiner et al. (2007) considered magnetoacoustic wave propagation in a complex, magnetically structured, non-stationary atmosphere. They showed that wave travel-times can be used to map the topography of the surface of thermal and magnetic equipartition ($\beta = 1$) of such an atmosphere. Hansteen et al. (2006) and De Pontieu et al. (2007) performed two-dimensional simulations covering the solar atmosphere from the convection zone to the lower corona. They showed how MHD waves generated by convective flows and oscillations in the photosphere turn into shocks higher up and produce spicules.

Despite these efforts, the physical processes that contribute to the enhanced network emission are still not fully understood. It is well known, that small scale magnetic elements have varying field strengths, ranging from hectogauss to kilogauss (Solanki 1993; Berger et al. 2004). This suggests that the $\beta = 1$ layer in these elements varies considerably in height, which in turn should affect the wave propagation in them (Schaffenberger et al. 2005).

3.2.1 METHOD AND BOUNDARY CONDITIONS

We consider waves excitation in the equilibrium magnetic field configuration described in Chapter 2, through a transverse motion of the lower boundary (similar to Hasan et al. 2005). The system of MHD equations, given in conservation-law form for an inviscid adiabatic fluid, is solved according to the method described in Steiner et al. (1994). These equations are the continuity, momentum, entropy, and the magnetic induction equations (see Appendix B for more details). The unknown variables are the density, ρ, the momenta, ρV_x and ρV_z, where V_x and V_z are the horizontal and vertical components of the velocity, the entropy per unit mass, s, and the components of the magnetic field, B_x and B_z. The equation of state corresponds to the solar composition in the photosphere with a mean molecular weight of 1.297. For the numerical integration, the system of MHD equations are transformed into a system of discrete finite volume equations. The numerical fluxes are computed based on the flux-corrected transport (FCT) scheme of Oran & Boris (1987) (see Appendix B). For the induction equation we use a constrained transport scheme (Devore 1991), which automatically keeps $\nabla \cdot \boldsymbol{B} = 0$. The time integration is explicit and of second order accuracy in time and has fourth order accuracy in space. The numerical techniques is described in Appendix B.

A finite size of the computational domain requires that the boundary conditions on every side be provided. The simulated region is a very small slice of the solar atmosphere. The implementation of boundary conditions requires that the values of the different parameters to be specified in the "ghost cells", which are the extensions of the computational box on the four sides. The different conditions implemented on the four boundaries are the following.

Bottom Boundary

We consider a lower boundary that lies at the base of the photosphere. It is "closed" with respect to material flow in and out of the computational region. We set the horizontal component of magnetic field to the same value as in the preceding interior point. The vertical component of the magnetic field is determined by the condition $\nabla \cdot \boldsymbol{B} = 0$. The density is computed using hydrostatic extrapolation. The temperature is determined by a constant extrapolation. A constant extrapolation of the horizontal and vertical component of the momentum is also applied. The system is driven by the forcing action of a flow at the lower boundary. A wide variety of different driving mechanisms can be implemented. In our case, we concentrated on horizontal driving, wherein the whole lower boundary is shaken horizontally. The transverse velocity V_x at $z = 0$ is specified as follows:

$$V_x(x, 0, t) = \begin{cases} V_0 \sin(2\pi t/P) & \text{for} \quad 0 \leq t \leq P/2\,, \\ 0 & \text{for} \quad 0 > t > P/2\,, \end{cases} \tag{3.19}$$

where V_0 denotes the amplitude of the horizontal motion and P is the wave period. This form was chosen to simulate the effect of transverse motion of the lower boundary. For simplicity we assume that all points of the lower boundary have this motion: this does not generate any waves in the ambient medium, other than at the interface with the flux sheet. In our simulation we use $V_0 = 750$ m s^{-1} and $P = 24$ s following Hasan et al. (2005). Such short duration motions are expected to be generated by the turbulent motion in the convectively unstable subsurface layers where the flux sheet is rooted. In terms of the analysis by Cranmer & van Ballegooijen (2005) of the kinematics of G-band bright points, this motion corresponds to a short, single step of their "random walk phase", for which these authors use a rms velocity of 0.89 km s^{-1} with a correlation time of bright-point motions of 60 s in accordance with the measurements of Nisenson et al. (2003). The cases with higher velocities would be representative of the "jump phase" for which Cranmer & van Ballegooijen (2005) use a velocity of 5 km s^{-1} with a duration of 20 s. This motion generates magnetoacoustic waves in the flux sheet.

Top Boundary

The top boundary is "open" in the sense that, any disturbance in the domain can escape through it without any reflection at the surface. This is achieved by a constant extrapolation of the horizontal component of the momentum. The density in the top boundary cells is determined using linear log extrapolation. For the temperature constant extrapolation is used. The horizontal component of the magnetic field at the top and bottom boundaries are set equal to the corresponding values at the preceding interior point. The vertical component of the magnetic field is determined by the condition $\nabla \cdot \boldsymbol{B} = 0$.

Side Boundaries

The side boundaries are also "open". Transmitting conditions apply to the side boundaries set by constant extrapolation of the variables from the physical domain to the boundary cells.

MOVIES OF THE SIMULATION

This thesis is accompanied with a CD-ROM containing movies of the simulation that will be described in the following sections and also in other chapters. The movies are provided to give the reader a more clear and detailed view of the processes being studied. The name of the movie files corresponding to a particular simulation is provided at the appropriate place where they are discussed. A more elaborate description of the movies is given in Appendix C.

3.2.2 POTENTIAL FIELD

We examine wave excitation in a potential field configuration, discussed in Chapter 2 due to a periodic transverse motions (this is different from the impulsive excitation described above) of the lower boundary, with a period of 24 s and an amplitude of 750 m s^{-1} (this corresponds to the *periodic* case treated by Hasan et al. (2005). These potential field configuration are similar to the one studied by Rosenthal et al. (2002) and Bogdan et al. (2003). It should be noted that the magnetic field above the base is more uniformly spread in the horizontal direction and there is no sharp interface that separates the field from the ambient medium.

Acoustic wave creates pressure fluctuations, and hence perturbations in the temperature relative to the background. By plotting contours of $\Delta T = T_{t=t} - T_{t=0s}$, we can see the propagation of an acoustic wave. Alfvénic type waves can be seen in the components of velocity perpendicular to the field line since they are associated with motions transverse to the field lines. Figure 3.1, 3.2 and 3.3 shows the temperature fluctuations (ΔT), parallel (V_s) and perpendicular (V_n) component of velocity (with respect to the magnetic field direction), respectively, at 27, 64, 100, and 137 s after the initiation of a periodic horizontal motion at the $z = 0$ boundary with an amplitude of 750 m s^{-1} and a period of $P = 24$ s. The thin black curves are magnetic field lines and the white curve represents the contour of $\beta = 1$. It is to be noted that in this particular simulation the side boundary condition is "periodic", which means that any disturbance propagating out of the left boundary enters

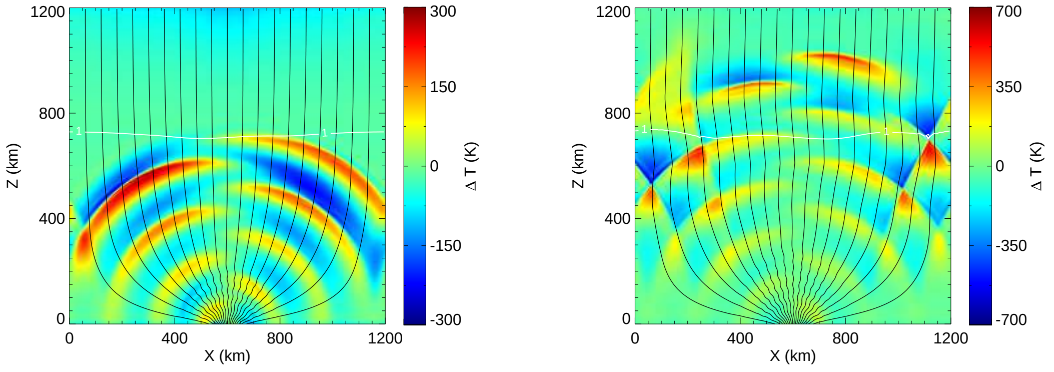

c) 100 s

d) 137 s

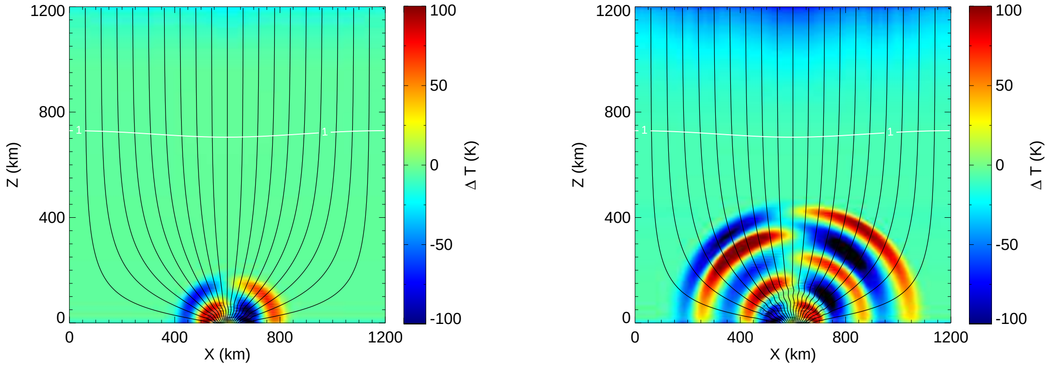

a) 27 s

b) 64 s

Figure 3.1: Temperature perturbations for the potential field configuration. The colours show the quantities at 27, 64, 100, and 137 s after initiation of an periodic horizontal motion at the $z = 0$ boundary with an amplitude of 750 m s^{-1} and a period of $P = 24$ s. The thin black curves are field lines and the white curve represents the contour of $\beta = 1$.

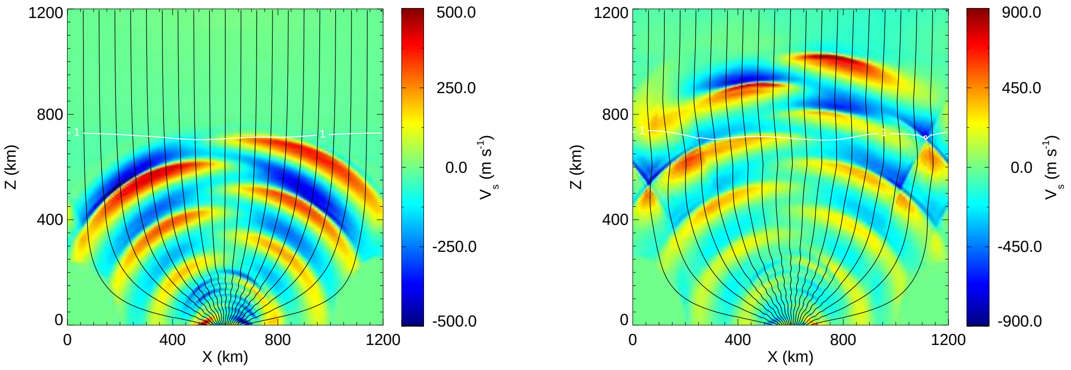

c) 100 s

d) 137 s

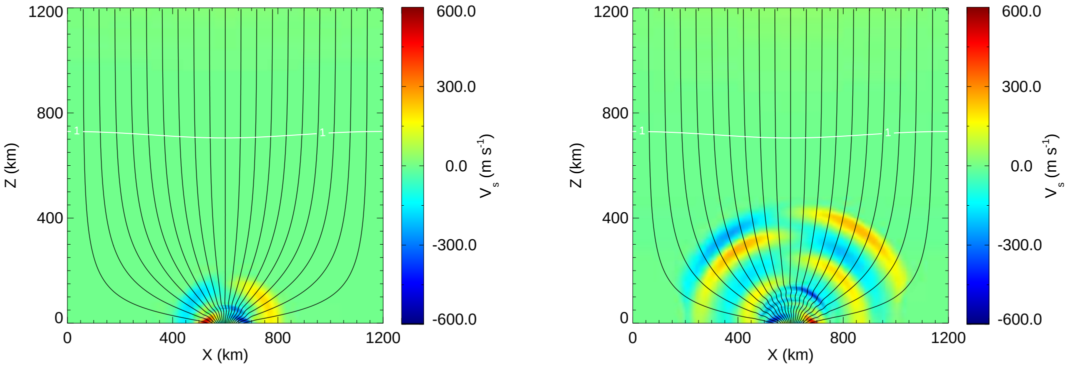

a) 27 s

b) 64 s

Figure 3.2: Parallel component of velocity for the potential field configuration. The colours show the quantities at 27, 64, 100, and 137 s after initiation of an periodic horizontal motion at the $z = 0$ boundary with an amplitude of 750 m s^{-1} and a period of $P = 24$ s. The thin black curves are field lines and the white curve represents the contour of $\beta = 1$.

the right boundary and *vice verse*.

Movie 3.1: Temperature fluctuations in a potential field configuration after initiation of a periodic horizontal motion of the lower boundary with an amplitude of 750 m s^{-1} and a period of P=24 s .

Movie 3.2: Parallel component of velocity in a potential field configuration after initiation of a periodic horizontal motion of the lower boundary .

Movie 3.3: Perpendicular component of velocity in a potential field configuration after initiation of a periodic horizontal motion of the lower boundary .

The $\beta = 1$ surface divides the domain into two regions: high-β (lower region) and low-β (upper region). The driving motion occurs in a low-β region. The periodic excitation at the flux tube base generate both slow (Alfvénic in character) and fast modes (acoustic) below the surface corresponding to $\beta = 1$. The fast mode waves in the lower boundary

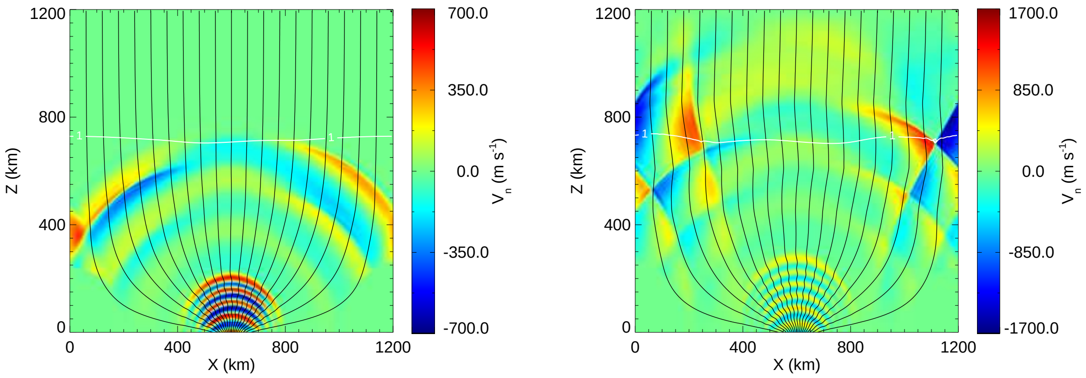

a) 100 s b) 137 s

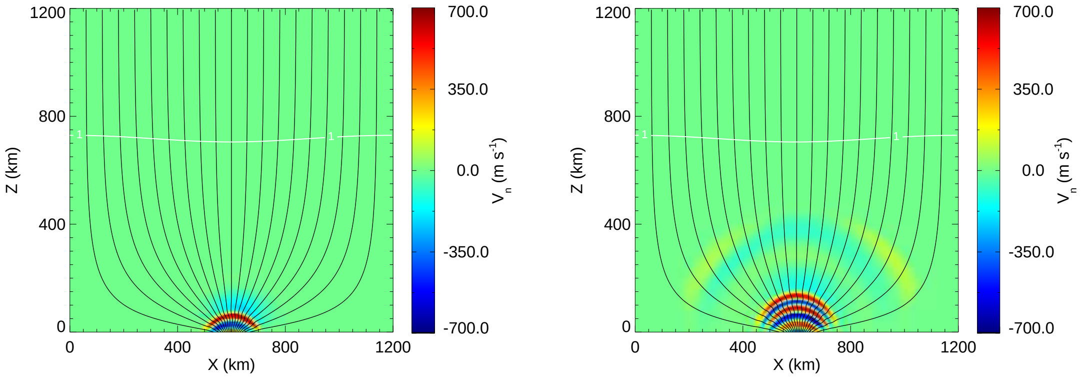

a) 27 s b) 64 s

Figure 3.3: Perpendicular component of velocity for the potential field configuration. The colours show the quantities at 27, 64, 100, and 137 s after initiation of an periodic horizontal motion at the $z = 0$ boundary with an amplitude of 750 $\mathrm{m\,s^{-1}}$ and a period of $P = 24$ s. The thin black curves are field lines and the white curve represents the contour of $\beta = 1$.

produce compressions and rarefactions that propagate ahead of the slow wave front. This can be clearly discerned from the ΔT snapshots (Fig. 3.1) and also in the V_s contours (Fig. 3.2). The compression and rarefactions are 180° out of phase on opposite sides of the axis. The slow modes are transverse to the field and produce distortions in the field lines. The slow modes can be easily seen in Fig. 3.3, that shows the perpendicular component of velocity V_n. Above the $\beta = 1$ layer, where the Alfvén speed is significantly higher than the sound speed, we see a longitudinal slow wave that is acoustic in nature, propagating at the acoustic speed. The lower part of the atmosphere (where $\beta > 1$), has both Alfvénic (transverse) and acoustic waves traveling almost isotropically and thereby transporting the energy in almost all directions.

Observations have shown that the G-band bright points can be mapped to their corresponding Ca II H & K bright points. Although the latter are seen to be more diffuse in nature than their counterparts in G-band, it is clear that the energy transport is channeled more along the flux tube than isotropically. From the results of simulations with a potential field model, we conclude that a potential field configuration does not provide a realistic model for the magnetic field in the network.

3.2.3 MAGNETOSTATIC FLUX TUBE

We now examine wave propagation in non potential field configurations of flux tube embedded in an atmosphere with typical photosphere and chromosphere like temperature profiles. The construction of the magnetostatic models were described in Chapter 2. We have studied different natures of excitation of these flux sheet to mimic various physical scenarios that are probable in a real atmosphere.

HORIZONTAL EXCITATION

Horizontal excitation refers to a simple impulsive excitation of the flux sheet in a horizontal plane. In a realistic atmosphere, this could be thought of as a buffeting of the tube by granular motions or by impact of traveling shocks. We examine wave propagation in a flux sheet embedded in chromosphere, with a sharp interface for two cases: the moderate and the strong field. We consider a uniform horizontal displacement of the bottom boundary for *half a period* after which the motion is stopped (this corresponds to the *impulsive* case treated by Hasan et al. (2005)

Moderate field

Let us consider a magnetic configuration in which the field strength at the axis of the flux sheet at $z = 0$ is 800 G. In this case the $\beta = 1$ contour is well above the bottom boundary in the atmosphere and hence all the magnetic field lines emerging from the base of the sheet cross this layer at some height. Waves are excited at $z = 0$, where $\beta > 1$ (on the axis $\beta = 1.8$), in the form of a fast (predominantly acoustic) wave and a slow (predominantly magnetic)[§] wave, which propagate respectively at the sound and the Alfvén speeds. On the sheet axis, the acoustic and Alfvén speeds at $z = 0$ are 7.1 and 6.0 km s^{-1}, respectively (see Table 2.3 in Chapter 2). The fast wave is created due to compression and rarefaction of the gas at the leading and trailing edge of the flux sheet, respectively: this can be

---

[§] For brevity we call modes in the following simply acoustic and magnetic depending on the predominance of the thermal and magnetic nature of their restoring forces.

clearly discerned in the snapshots of the temperature perturbation, ΔT (the temperature difference with respect to the initial value), shown in Fig. 3.4 at 40, 60, 80 and 120 s after start of the perturbation.

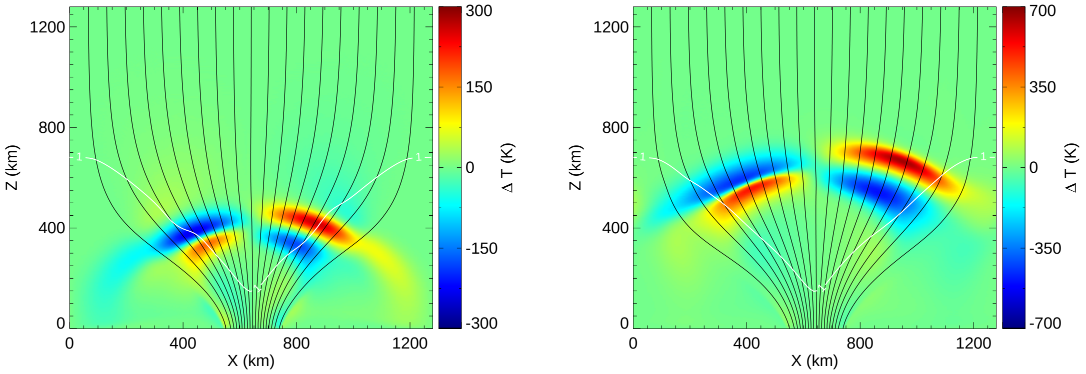

c) 80 s   d) 120 s

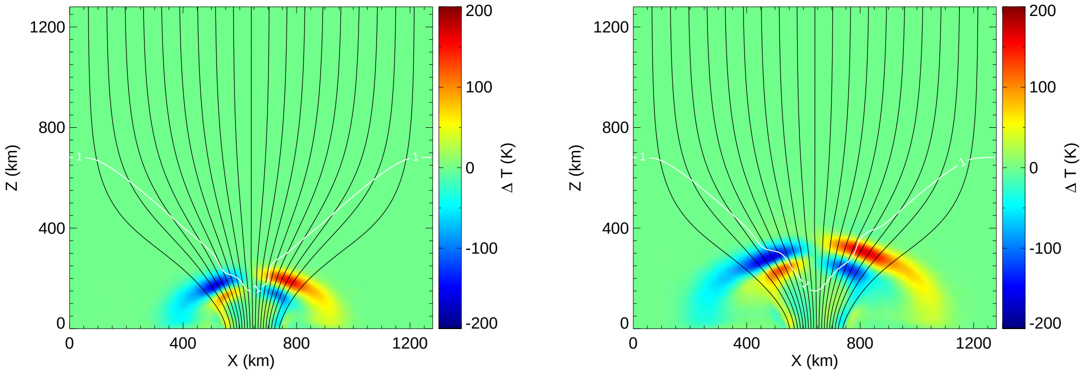

a) 40 s   b) 60 s

Figure 3.4: Temperature perturbations for the case in which the field strength at the axis at $z = 0$ is 800 G (moderate field). The colours show the temperature perturbations at 40, 60, 80, and 120 s after initiation of an impulsive horizontal motion at the $z = 0$ boundary of a duration of 12 s with an amplitude of 750 m s^{-1} and a period of $P = 24$ s. The thin black curves are field lines and the white curve represents the contour of $\beta = 1$.

Movie 3.4: Temperature perturbations in a magnetohydrostatic flux sheet of moderate field strength after the initiation of a impulsive excitation in the lower boundary with an amplitude of 750 m s^{-1} and a period of P=24 s

These and other panels in the following figures do not show the full height range of the computational domain but only up to 1280 km above the photosphere base. The black curves denote the magnetic field lines and the white curve depicts the $\beta = 1$ contour. The perturbations are 180° out of phase on opposite sides of the sheet axis. As these fast waves travel upwards they eventually cross the layer of $\beta = 1$, where they change their label from “fast” to “slow”, without changing their acoustic nature: this corresponds to a “mode transmission” in the sense of Cally (2007). The transmission coefficient depends (among others) on the “attack angle” i.e., the angle between the wave vector and the local direction of the magnetic field (Cally 2007). On the $\beta = 1$ layer, away from the sheet axis, where the wave vector is not exactly parallel to the magnetic field, we do not have complete transmission of the fast wave to a slow wave. Rather, there is a partial conversion of the mode from fast acoustic to fast magnetic, so that the energy in the acoustic mode is reduced correspondingly. Figures 3.5a and 3.5b shows the velocity components in the flow parallel (V_s) and perpendicular (V_n) to the field, respectively.

Movie 3.5: Parallel component of velocity in a magnetohydrostatic flux sheet of moderate field strength after the initiation of a horizontal impulsive excitation in the lower boundary .
Movie 3.6: Perpendicular component of velocity in a magnetohydrostatic flux sheet of moderate field strength after the initiation of a horizontal impulsive excitation in the lower boundary .

The velocity components are shown only in regions where the field is greater than 50 G since in the ambient medium with weak field this decomposition is no longer meaningful. In general the waves possess both longitudinal and transverse velocity components, but in regions where $\beta < 1$, the parallel component essentially corresponds to the slow (acoustic) wave that is guided upward along the field. This correspondence can be seen by comparing the parallel flow pattern (in Fig. 3.5a) with the temperature perturbation in Fig. 3.4.

The excitation at the bottom boundary also generates a slow (magnetic) wave with velocity perturbations normal to the magnetic field line. In order to visualize the slow wave, we show the velocity component normal to the magnetic field in Fig. 3.5b. The slow wave also encounters the layer of $\beta = 1$ and undergoes mode transmission and conversion. Above the layer of $\beta = 1$, the transmitted wave is a fast mode, which rapidly accelerates due to the sharp increase in Alfvén speed with height.

Strong field

We now consider the case in which the field strength on the sheet axis is 1600 G (at $z = 0$). Here, the contour of $\beta = 1$ approximately traces the boundary of the flux sheet. The transverse motion of the lower boundary generates slow (essentially acoustic) and fast (essentially magnetic) waves. Since the contour of $\beta = 1$ runs along the boundary of the flux sheet, waves generated in the sheet that travel upwards do not encounter this layer and

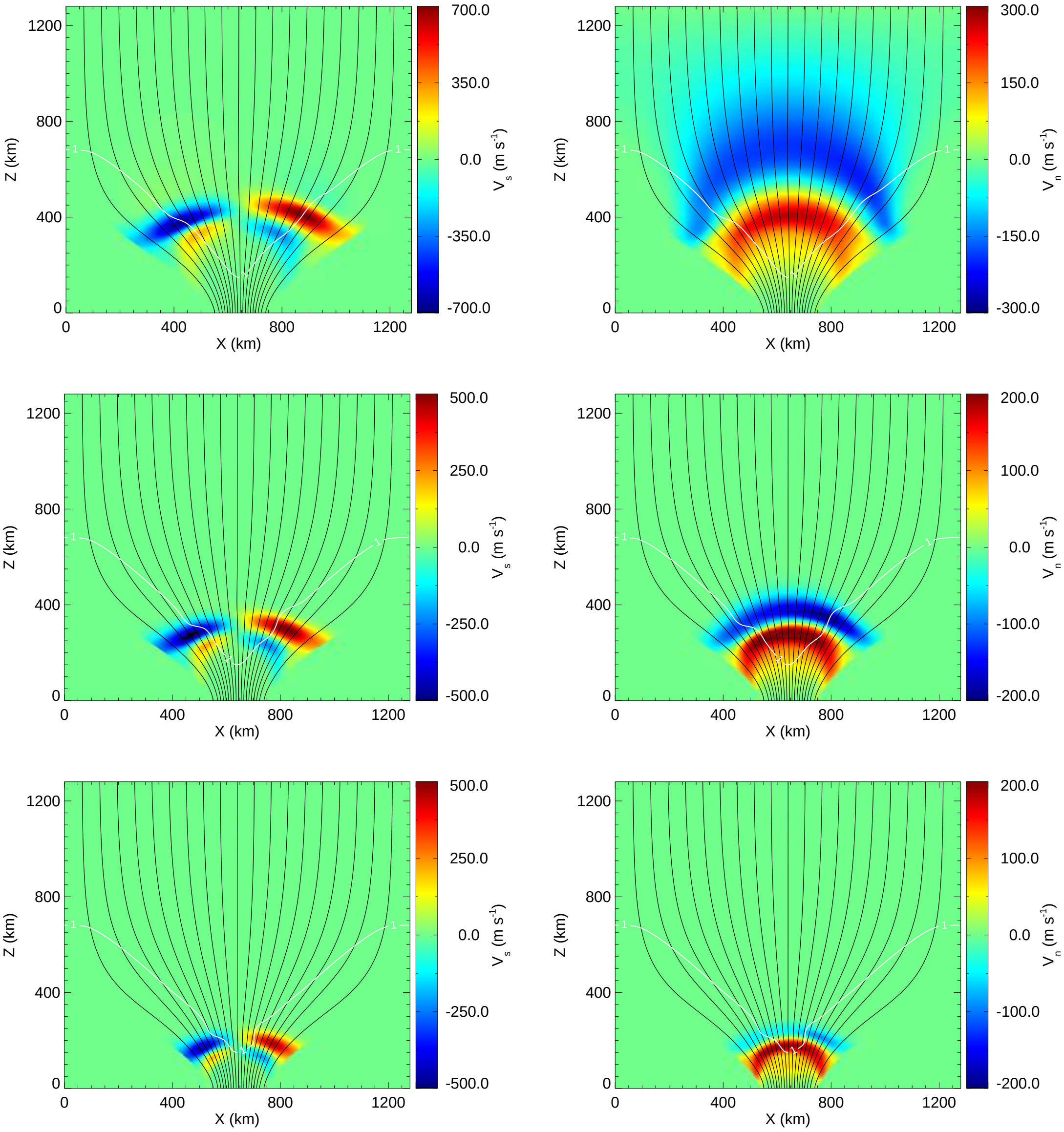

a) V_s b) V_n

Figure 3.5: Velocity components for the case in which the field strength at the axis at z=0 is 800 G (moderate field). The colours show the velocity components (a) V_s, along the field, and (b) V_n, normal to the field, at 40, 60, and 80 s (from bottom to top) after initiation of an impulsive horizontal motion at the $z = 0$ boundary of a duration of 12 s with an amplitude of 750 m s^{-1} and a period of $P = 24$ s. The thin black curves are field lines and the white curve represents the contour of $\beta = 1$. The field aligned and normal components of velocity are not shown in the regions where $B < 50$ G.

hence do not undergo mode conversion. Figure 3.6 shows the temperature perturbation

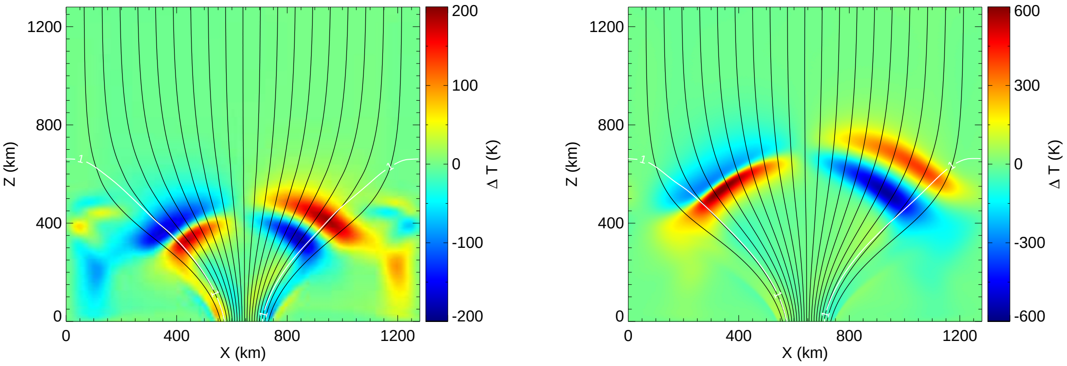

c) 80 s d) 120 s

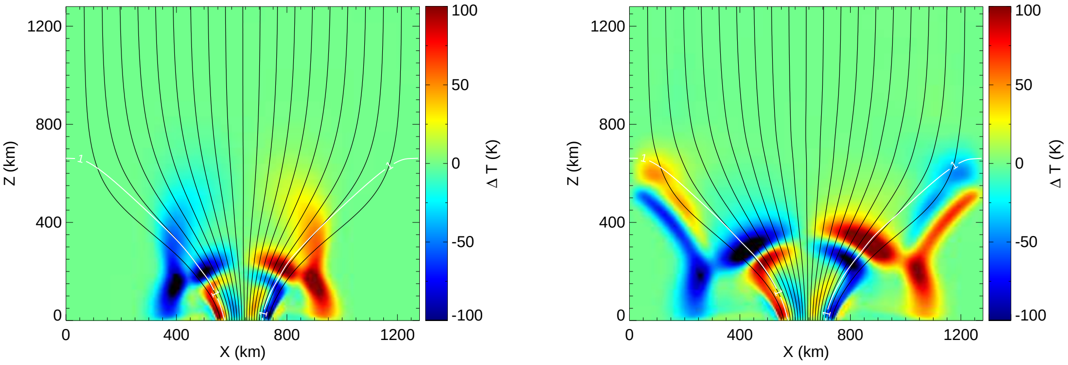

a) 40 s b) 60 s

Figure 3.6: Temperature Perturbations for the case in which the field strength at the axis at z=0 is 1600 G (strong field) for times t = 40, 60, 80, and 120 s. The coding corresponds to that of Fig. 3.4.

ΔT at 40, 60, 80, and 120 s.[¶]. Figure 3.7 shows the parallel and perpendicular components (with respect to the magnetic field) of the velocity.

Movie 3.7: Temperature perturbations in a magnetohydrostatic flux sheet of strong field strength after the initiation of a horizontal impulsive excitation in the lower boundary with an amplitude of 750 m s^{-1} and a period of P=24 s .

[¶] The temperature perturbations along the flux-sheet edges in the wake of the slow acoustic wave (red and blue ridges along the left and right boundary in the lower part of the flux sheet, respectively) do not pertain to a traveling wave. They are due to the finite shift of the flux sheet with respect to the initial, static configuration. This shift is compensated for by a corresponding shift of the unperturbed solution for the computation of energy fluxes in Sects. 4.4 and 4.4.1.

Movie 3.8: Parallel component of velocity in a magnetohydrostatic flux sheet of strong field strength after the initiation of a horizontal impulsive excitation in the lower boundary .

Movie 3.9: Perpendicular component of velocity in a magnetohydrostatic flux sheet of strong field strength after the initiation of a horizontal impulsive excitation in the lower boundary .

The slow (acoustic) wave is guided upwards along the field without changing character. On the other hand, the fast wave, which can travel across the field encounters the $\beta = 1$ contour at the boundary of the flux sheet. As the fast wave crosses this layer, it enters a region of negligible field and hence gets converted into a fast (acoustic) wave. This can be easily seen in the snapshot of temperature perturbations at an elapsed time of 40 s. The fast wave in the low-β region, which is essentially a magnetic wave, undergoes mode conversion and becomes an acoustic wave, which creates fluctuations in temperature visible as wing like features in the periphery of the flux sheet between approximately $z = 200$ to 500 km. The fast wave gets refracted due to the gradients in Alfvén speed higher up in the atmosphere. Furthermore, similar to Hasan et al. (2005), we find that the interface between the magnetic flux sheet and the ambient medium is a source of acoustic emission. It is visible in Fig. 3.6 as a wave of shell-like shape in the ambient medium that emanates from the base of the flux sheet and subsequently propagates, as a fast acoustic wave, laterally away from it.

Incidentally, the phase of transverse movement changes by 180° between the moderate and strong field case as can be seen comparing Fig. 3.5b with Fig. 3.7b. This is due to the development of a vortical flow from the high pressure leading edge of the flux sheet to the low pressure trailing edge that develops in the high-β photospheric layers of the moderately strong flux sheet but is largely suppressed in the strong field case, where it is from the beginning preceded by the fast (magnetic) wave that emerges right from the initial pulse. The development of a vortical flow in the moderate field case was also noticed in Hasan et al. (2005). Besides the fast and slow acoustic and the fast magnetic wave that emanate directly from the initial perturbation there is also a slow magnetic mode from this source, which propagates in the high-β surface layer of the flux sheet. It is visible in Fig. 3.7b as the yellow/red crescent-shaped perturbation, which trails the red and blue crescents pertaining to the fast magnetic mode. Different from the latter, which is maximal at the flux-sheet axis, the slow mode has maximal amplitude in the weak-field boundary-layer of the flux concentration. A similar but acoustic slow surface mode was found by Khomenko et al. (2008) when the driver was located in the high-β layers of the flux concentration. Here, this mode generates a remarkable amount of acoustic emission

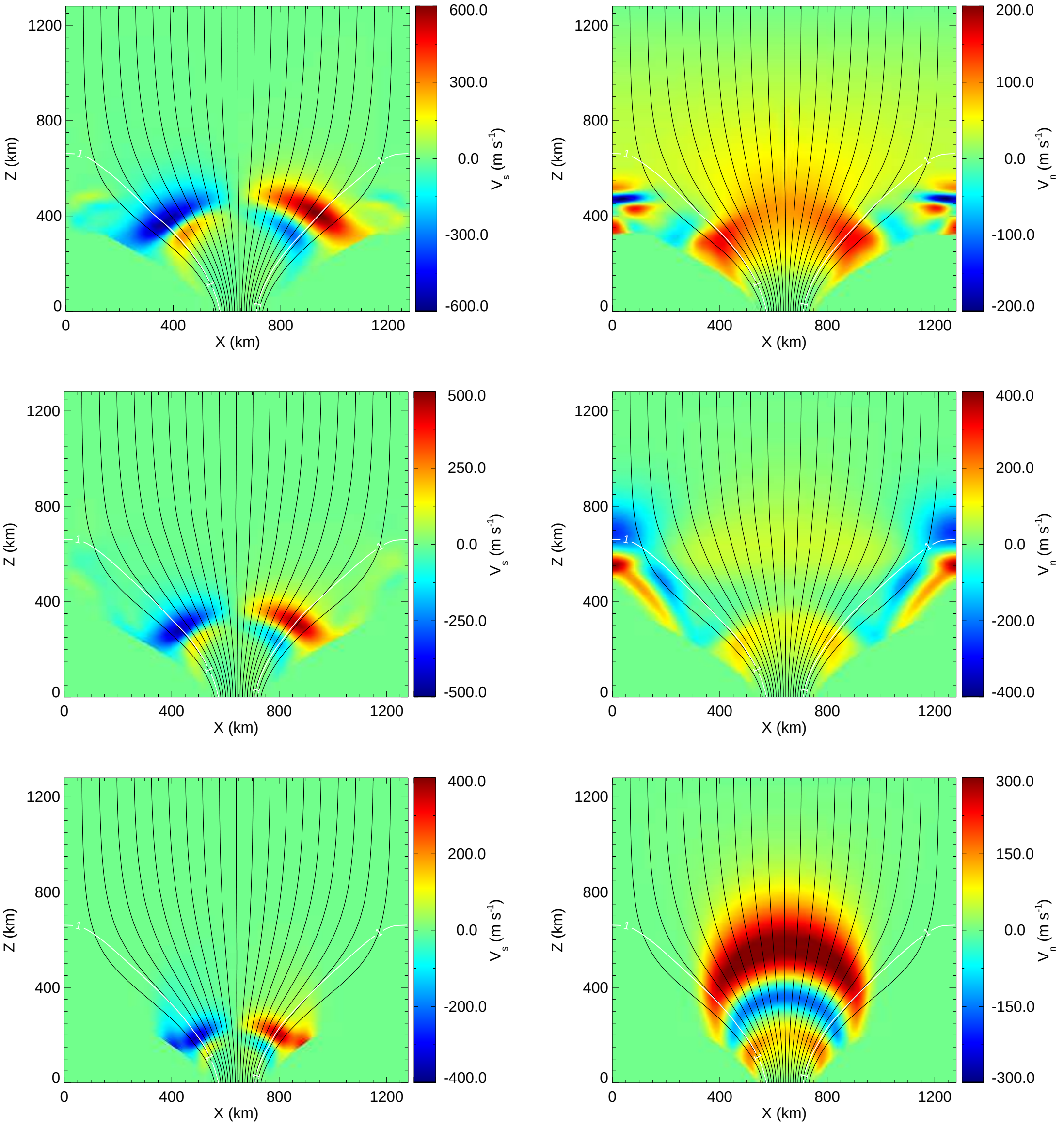

a) V_s

b) V_n

Figure 3.7: Velocity components for the case in which the field strength at the axis at z=0 is 1600 G (strong field) for times t = 40, 60, and 80 s. The coding corresponds to that of Fig. 3.5.

to the ambient medium as will be seen in Chapter 4.

HORIZONTAL EXCITATION WITH TWO PULSES

We now consider a horizontal displacement of the bottom boundary for a duration of *two periods* after which the motion is stopped. Wave propagation were studied in the “strong field" case with a sharp interface. This particular form of the driver was chosen in order to demonstrate the shock mergings that occur in a stratified atmosphere when a preceding wavefront crosses a wavefront traveling ahead of it.

The driving motion generates both slow and fast wave inside the flux sheet as seen in the case with impulsive excitation. The fast wave travels rapidly and is refracted. Figure 3.8 shows the temperature perturbations for times t = 40, 119, 160, and 190 s.

Movie 3.10: Temperature perturbations in a magnetohydrostatic flux sheet of strong field strength after the initiation of a horizontal excitation with two pulses with an amplitude of 750 m s^{-1} and a period of P=24 s .

The temperature perturbations are similar to that of the impulsive excitation, except that there is a additional wave following the initial one. The compressional front of this wave, which can be seen as a second temperature enhancement on the left of the axis, follows the leading front. This trailing front, with its enhanced temperature travels faster than its leading rarefaction front (in blue between the yellow arcs). It slowly starts merging with the leading front from the left side and continues to do until it is completely merged. The merging of the two fronts produces a intense shock front on the left side of the tube axis. At 190 s, after the simulation, the second merged front can be seen as a deep red coloured hump on the left part of the first front. The temperature enhancement is four times that on the right side, where the scenario is quite different. Here, the leading front has a temperature enhancement and hence travels faster than its trailing part, which has a lower temperature. The trailing front cannot over take the leading front, and they move away from each other and hence there is no mergings of the two fronts. Dissipation of these type of stronger shocks formed by the merging of two or more shocks can be possible candidates for the heating of magnetic network. The stronger asymmetry of the shock formation seen in this particular case is an important feature which is different from a simple impulsive excitation. The observational implications of above type of multiple excitation and stronger shock formation as a result of such mergings is that it can lead to asymmetrical brightening within the flux tube. We predict that high spatial and temporal resolution observations may reveal this asymmetric nature within a bright point.

Ulmschneider et al. (2005) showed that one dimensional calculations can lead to unrealistic shocks and artificial shock merging. They argued that the perfect alignment of shocks is an artefact that occurs in such calculations due to the dimensionality of the problem and hence, interpretation of observations in terms of one dimensional shock merging models is unreliable. Our two dimensional simulations have shown that shock merging are a natural consequence of multiple excitation, which are very likely to occur in a realistic atmosphere. Thus we emphasize that these representatives of chromospheric heating cannot be completely ruled out.

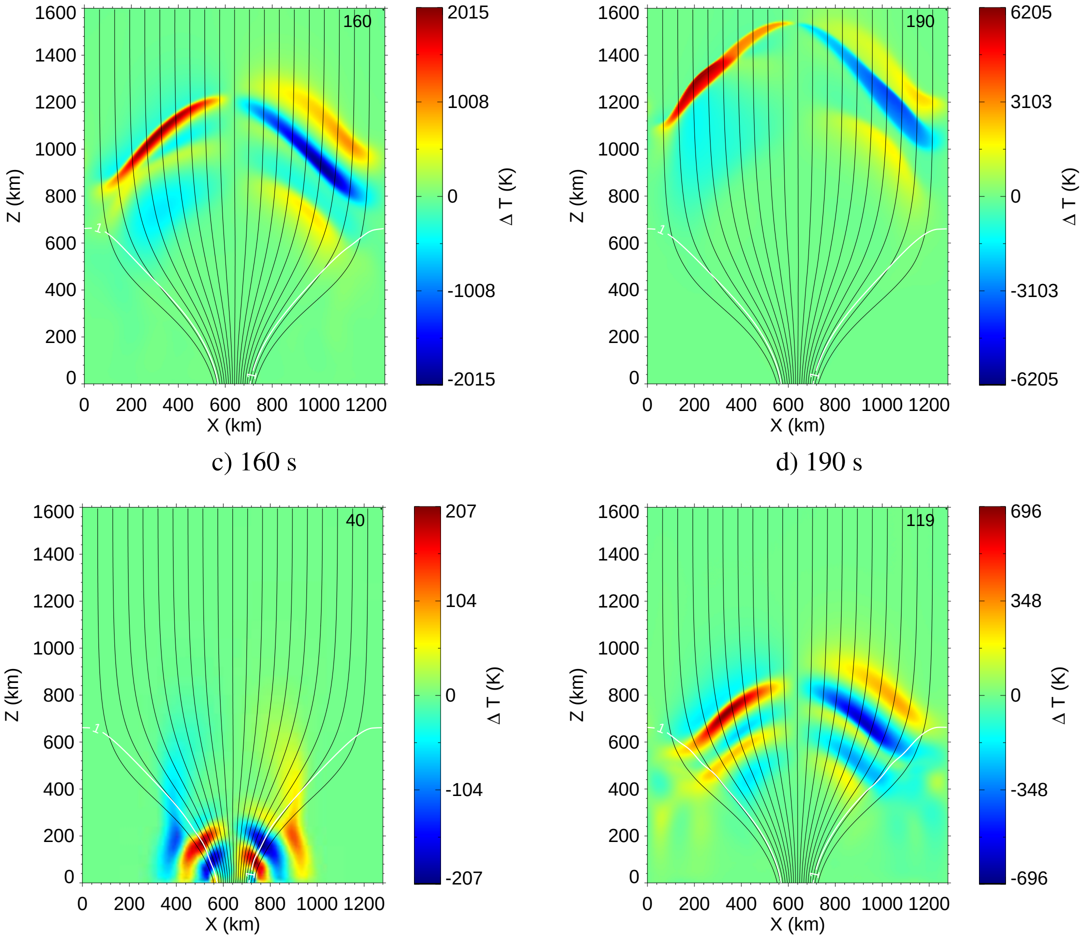

c) 160 s

d) 190 s

a) 40 s

b) 119 s

Figure 3.8: Temperature Perturbations for the case in which the field strength at the axis at z=0 is 1600 G (strong field) for times t = 40, 119, 160, and 190 s. The coding corresponds to that of Fig. 3.4.

HORIZONTAL EXCITATION OVER A WIDER RANGE

We consider a uniform horizontal displacement of the entire bottom boundary upto 150 km (which we term as narrow) and 300 km (wide) in a flux sheet embedded in a photosphere. This is to mimic the buffeting of the flux tubes by different sizes of granular blobs. The excitation corresponds to the *impulsive* case discussed in the earlier part.

We consider the case in which the field strength on the sheet axis is 1600 G (at $z = 0$). Here, the contour of $\beta = 1$ approximately traces the boundary of the flux sheet. The transverse motion of the lower boundary generates slow (essentially acoustic) and fast (essentially magnetic) waves. Since the contour of $\beta = 1$ runs along the boundary of the flux sheet, waves generated in the sheet that travel upwards do not encounter this layer and hence do not undergo mode conversion. Figure 3.9 shows the temperature perturbation ΔT at 40, 60, 80, and 120 s for the two excitations.

Movie 3.11: Temperature perturbations of a flux sheet with strong field strength after the initiation of a horizontal excitation over a height of 150 km .
Movie 3.12: Temperature perturbations of a flux sheet with strong field strength after the initiation of a horizontal excitation over a height of 300 km .

We see that in both cases, since the excitation takes place on a flux sheet in a region with low-β, the slow (acoustic) wave is guided upwards along the field without changing character. On the other hand, the fast wave, which can travel across the field encounters the $\beta = 1$ contour at the boundary of the flux sheet. As the fast wave crosses this layer, it enters a region of negligible field and hence gets converted into a fast (acoustic) wave as can be easily seen in the snapshot of temperature perturbations at an elapsed time of 40 s. The fast wave in the low-β region, which is essentially a magnetic wave, undergoes mode conversion and becomes an acoustic wave, which creates fluctuations in temperature visible as wing like features in the periphery of the flux sheet. The refraction of the fast wave due to the gradients in Alfvén speed higher up in the atmosphere and the eventual mode conversion is very prominent in the wide excitation case. This can be hardly seen in the case where the flux sheet is shaken over a narrow region. This is due to the fact that an excitation over a larger range in a flux tube embedded in a low-β region imparts more energy to the fast (magnetic) wave. Due to the gradients in Alfvén speed, this mode gets refracted and returns back to a region with high-β and this energy is transferred to the fast (acoustic) wave producing larger temperature fluctuations. With an excitation confined to a horizontal plane, we have seen that, the nature of modes excited depends on the plasma β of the region where the excitation occurs. Here we see that depending upon the extent of the region of excitation energy imparted to different modes vary. This has implications in a realistic atmosphere, where granular blobs of different sizes are likely to impact on the deep rooted flux tubes and excite waves in them. A larger area impact on a flux tube with strong field will transfer more energy to the fast (magnetic) mode, but the non-magnetic atmosphere gains back this energy in the form of a fast (acoustic) wave due to the refraction and mode conversion. Whereas, if the area of impact is smaller, then most of the energy goes into the slow (acoustic) wave, which is channeled up along the flux tube and eventually dissipates by shock formation.

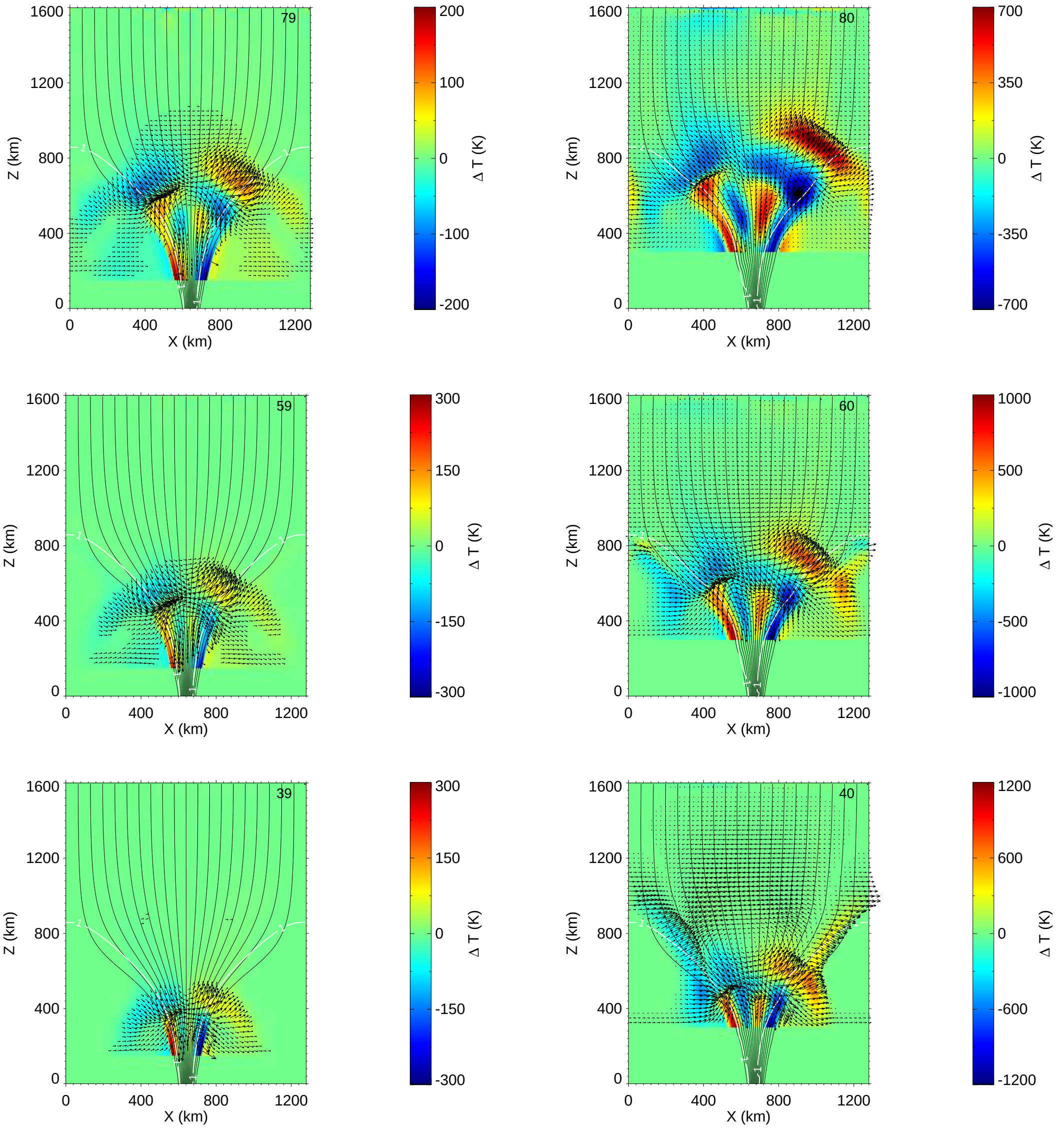

(a) Narrow (a) Wide

Figure 3.9: Temperature perturbations for a narrow and wide excitations in a flux tube in which the field strength at the axis at $z = 0$ is 1600 G. The colours show the temperature perturbations at 40, 60, 80 s (from bottom to top) after initiation of an impulsive horizontal motion in a wider region from the $z = 0$ boundary upto $z = 150$km (for narrow) and $z = 300km$ (wide) of a duration of 12 s with an amplitude of 750 $\mathrm{m\,s^{-1}}$ and a period of $P = 24$ s. The thin black curves are field lines and the white curve represents the contour of $\beta = 1$.

3.3 LOCAL HELIOSEISMIC EXPERIMENTS WITH HIGH FREQUENCY WAVES[‖]

We have carried out a series of two-dimensional MHD-simulations of the propagation of high frequency waves through a magnetically structured, realistic atmosphere. This simulations were carried out using a new, optionally 3-D, magneto radiation hydrodynamics code: CO5BOLD. This work was carried out in the wake of the new possibilities to obtain the three-dimensional topography of the 'magnetic canopy' in and around active regions, inspired from the method employed by Finsterle et al. (2004) Their method bears considerable potential for the exploration of the magnetic field in the solar atmosphere by helioseismological means.

Our simulation was carried out in a two-dimensional computational domain of 4900 km width and spanning a height range of 2900 km, of which 1300 km reach into the convection zone and 1600 km above the average level of optical depth unity. The MHD simulation starts with a homogeneous, vertical, unipolar magnetic field of a flux density superposed on a previously computed, relaxed model of thermal convection. This flux density is thought to mimic magnetoconvection in a very quiet network-cell interior. The magnetic field is constrained to have vanishing horizontal components at the top and bottom boundary but lines of force can freely move in the horizontal direction, allowing for flux concentrations to extend right to the boundaries. Subsequent to superposition of the magnetic field, flux expulsion from the granule centres takes place, the magnetic field concentrates in narrow sheets and small knots near the surface of optical depth unity with field strengths up to approximately 1 kG. Occasionally, these magnetic flux concentrations extend down to the bottom boundary at a depth of 1400 km but more often, they disperse again at a depth of less than 1000 km leaving flux concentrations of a strength of a few hundred Gauss only.

A mean magnetic flux density of 10 G and 100 G is added, so that the magnetic structures that form in the course of time represent magnetic fields in a very quiet network cell interior and in the magnetic network, respectively. We introduce a velocity perturbation of given frequency and amplitude at the bottom of the computational domain with which we generate a monochromatic, plane parallel wave that propagates within a time span of about 200 s across the height range of the computational domain.

The arrival time of the wave front at three different heights in the atmosphere that roughly corresponds to heights of maximal Doppler response of the spectral lines Ni textsci

---

[‖] see Steiner et al. (2007)

6768 Å at 200 km, K I 7699 Å at 420 km, and Na I 5890 Å at 800 km (Finsterle et al. 2004) were determined. The travel time between these heights were then calculated. The travel times are thought to be modified through the presence of magnetic fields in the sense that a strong magnetic field reduces the travel time.

In the following we consider the time span from $t = 1200$ s to $t = 1400$ s of a simulation that started with a homogeneous vertical field of 100 G at $t = 0$ s. Fig. 3.10 and 3.11 shows a snapshot of the instant $t = 1368$ s.

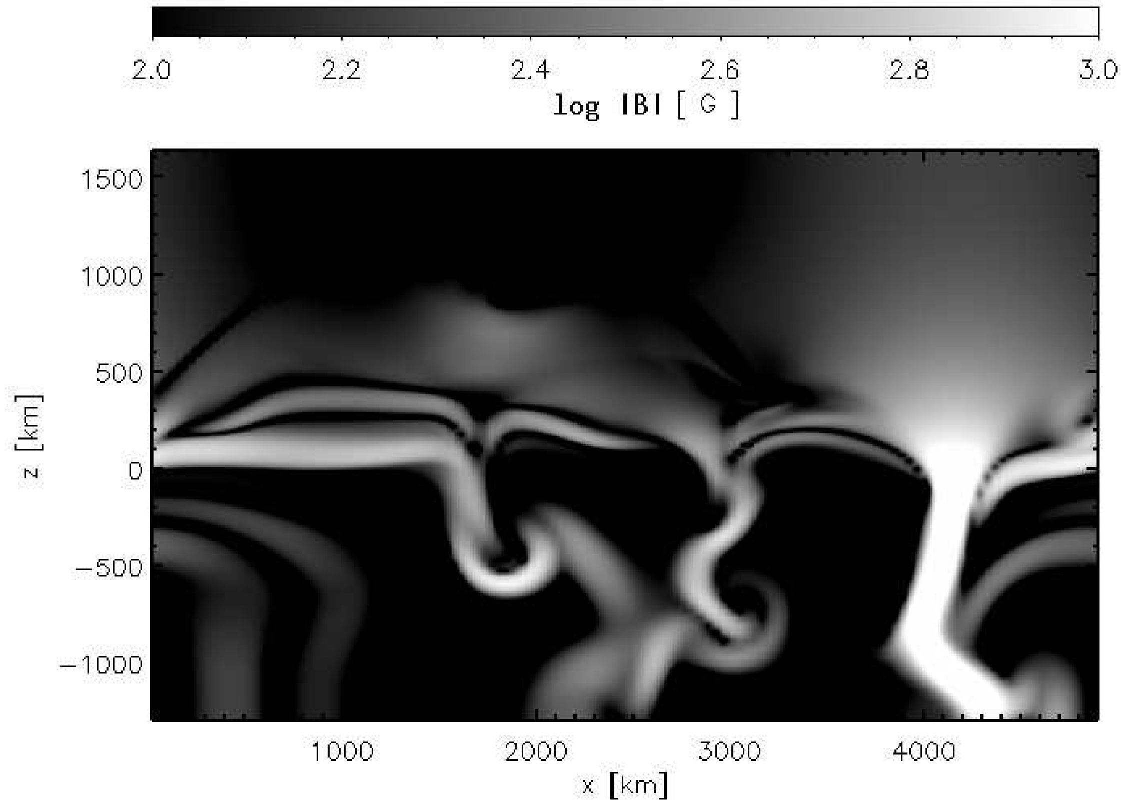

Figure 3.10: Snapshots showing the logarithmic magnetic flux density from a time series for the instant $t = 1368$ s after starting with an initial homogeneous vertical field of 100 G.

Figure 3.10 shows the logarithmic magnetic flux density, where the values of the field in Gauss are indicated in the grey-scale bar in the top margin of the figure. A strong magnetic flux sheet has formed near $x = 4000$ km. It leads to a dip in the surface of optical depth unity, visible in the Fig 3.11. There, also the contour of $\beta = 1$, where $\beta = p_{\mathrm{gas}}/(B^2/2\mu)$, i.e., the contour of equipartition of thermal and magnetic energy density, is indicated. The magnetic flux concentration causes a funnel of low β.

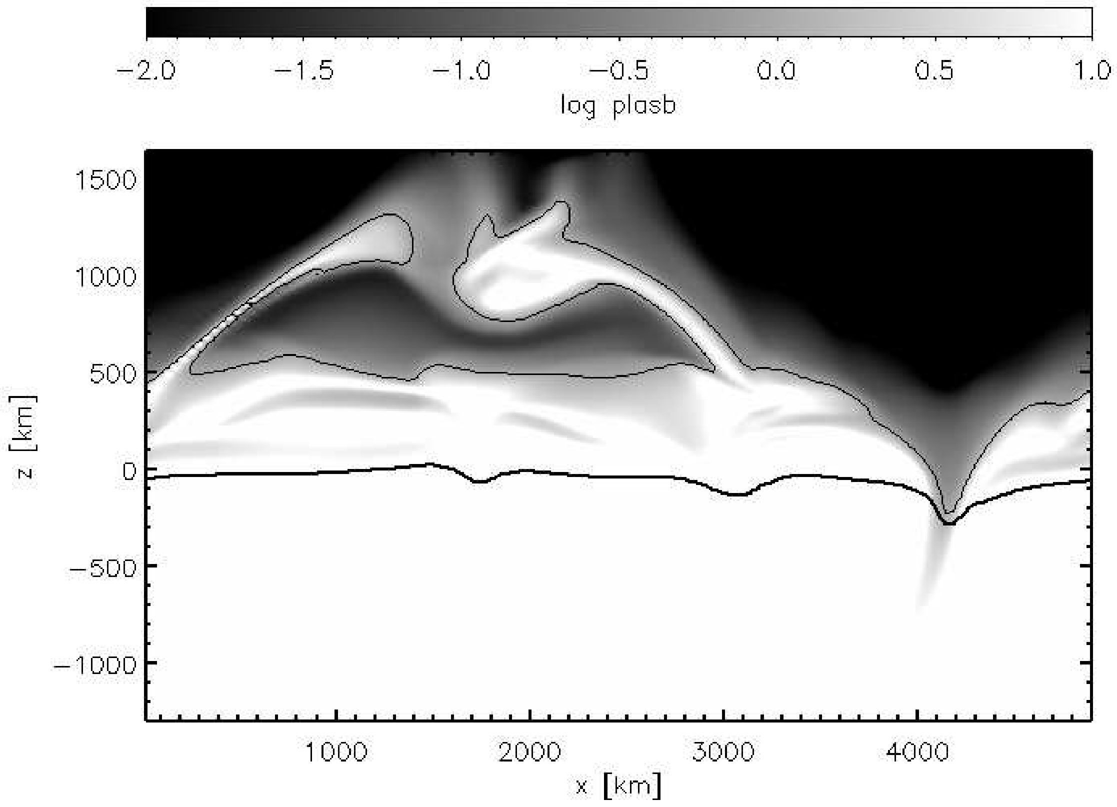

Figure 3.11: Snapshots showing the logarithm of the ratio of thermal and magnetic energy density from a time series for the instant $t = 1368$ s after starting with an initial homogeneous vertical field of 100 G. Also shown are the contour of $\beta = 1$ (thin curve) and the surface of optical depth unity, $\tau_{5000\,\text{Å}} = 1$. A strong magnetic flux sheet has formed near $x = 4000$ km that causes the funnel of low β visible in the right hand panel.

Once the magnetic field, which may be concentrated in small tubes and sheets in the deep photosphere, has expanded to completely fill the available space, it cannot further expand and its strength remains essentially constant with height. Therefore, β decreases with height so that with increasing height the atmosphere becomes magnetically dominated. Correspondingly, the $\beta = 1$ contour in Fig. 3.11 extends in a more or less horizontal direction at a height of 500 km with the exceptions of the location of the strong flux sheet, where it dips even below $z = 0$, and two islands higher up in the atmosphere, caused by chromospheric shock waves.

The $\beta = 1$ contour also marks the region of wave transmission and conversion as discussed in the earlier sections. This effect is visible in Fig. 3.12, which shows, from bottom to top, a time sequence of a plane wave traveling through the magnetically structured and simultaneously evolving atmosphere of Fig. 3.10 and 3.11. In order to visualize the wave we have run the simulation twice from $t = 1200$ s to $t = 1400$ s, once without perturbation and once with a velocity perturbation at the bottom of the computational domain of the form

$$v_z(t) = \mathrm{v}_0 \sin(2\pi(t - t_0)\nu)\,, \tag{3.20}$$

where v_0 was chosen to be 0.05 km s^{-1} and $\nu = 20$ mHz. The two runs were carried out with identical time stepping. Following that, the two velocity fields are subtracted, which then reveals the wave perturbation that travels on top of the non-stationary evolving convective motion.

Initially the wave front is retarded at the location of the flux concentration (at $x \approx$ 4000 km) because of the lower temperature of the plasma within the flux concentration, hence the lower sound speed (bottom panel, 100 s after start of the perturbation). It undergoes acceleration when entering the funnel of $\beta < 1$ so that the wave within the funnel is now leading 148 s after start of the perturbation (middle panel). At the same time the wave becomes fast magnetic in character and starts to refract. Thus, the wave front becomes inclined until aligned with the vertical direction and it further turns until traveling into the downward direction. In the top panel, only 20 s later, the wave front in the low-β funnel (extending horizontally from $x = 2400$ km to 3400 km and vertically from $z = 500$ km to 1500 km) has already completely turned around and travels back *into* the atmosphere. Therefore, we can speak of a reflection of the magnetic wave in the low-β region. A similar fanning out of the wave front occurs around $x = 1400$ km when it reaches the 'canopy'-height where $\beta = 1$ at about 500 km.

We see that the travel time for the wave in the low-β region is much smaller than elsewhere. Fig. 3.13 shows the travel time between the line formation heights of Ni I, 6768 Å at 200 km and K I 7699 Å at 420 km (thick solid curve) as a function of horizontal distance, x. The time axis is given on the left hand side. Superposed on this plot is the contour of $\beta = 1$ (dash-dotted curve), where the height in the atmosphere is given by the z-axis on the right hand side. Clearly, the travel-time curve follows the dip of the β-contour at the location of the flux concentration, which demonstrates that a mapping of the $\beta = 1$ surface by helioseismic methods is in principle possible.

Because of the spurious velocity noise in the region of very low β, we were unable to reliably determine the wave-front arrival at the line-formation height of Na I D2, 5890 Å at 800 km. But we expect for the travel time difference between 800 and 420 km an even more pronounced dip at the location of the magnetic flux concentration than for the difference between 200 and 420 km.

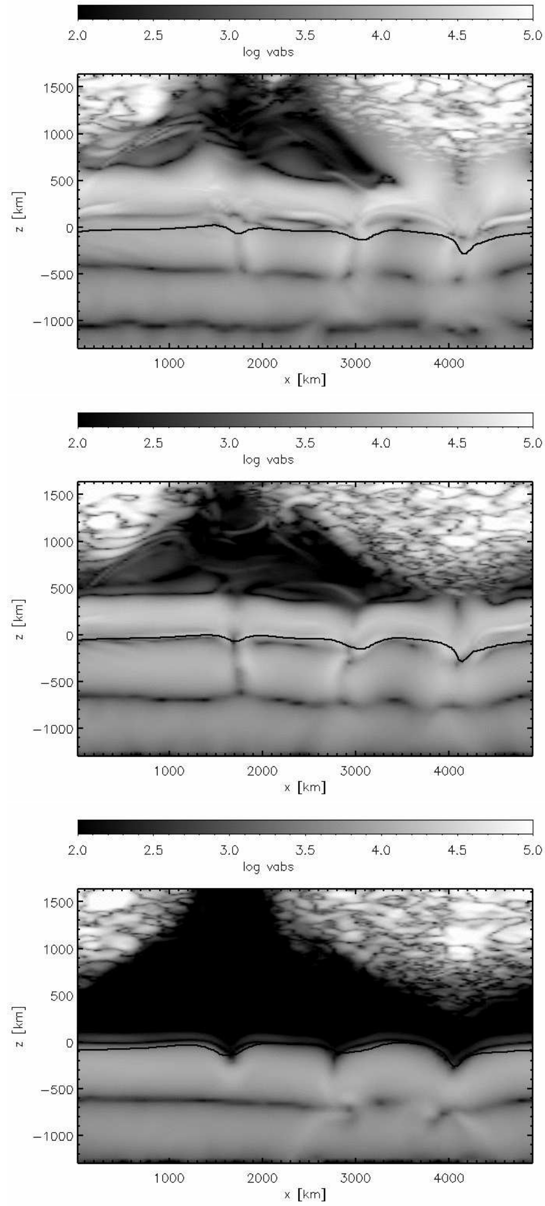

Figure 3.12: A plane parallel wave with frequency 20 mHz travels through convecting plasma into the magnetically structured photosphere and further into the low β (magnetically dominated) chromosphere. The three panels show the difference in absolute velocity between the perturbed and the unperturbed solution 100 s, 148 s, and 168 s (from bottom to top) after the start of the perturbation (Eq. 3.20). Magnetic field and plasma β corresponding to the instant of the top panel are given in Fig. 3.11. The horizontally running black curve near $z = 0$ indicates optical depth $\tau_{5000\,\text{Å}} = 1$.

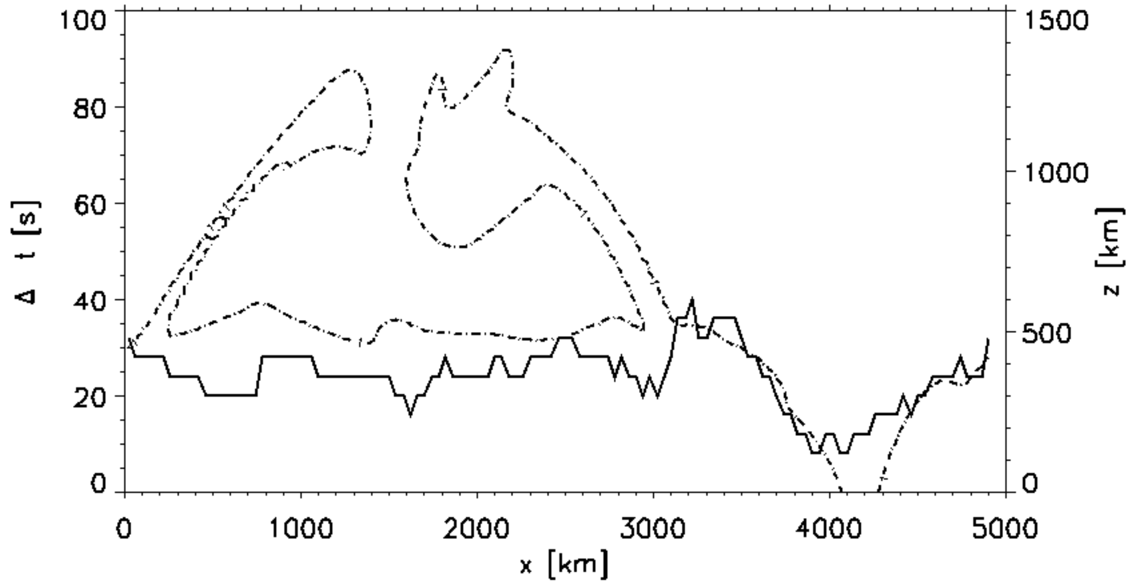

Figure 3.13: Wave travel time across the layer from $z = 200$ km to $z = 420$ km as a function of horizontal distance (thick solid curve). Superposed is the contour of $\beta = 1$ (magnetic and thermal equipartition), for which the height is indicated in the right hand side ordinate (dash-dotted curve). Note that the travel time markedly decreases where the low β region intrudes this layer.

We show that the wave travel-time between two fixed levels in the atmosphere bears information on the nature of the wave and consequently on the magnetic field. The travel time is reduced in regions of low β (strong magnetic field). For a monochromatic wave of frequency 20 mHz we demonstrate with Fig. 3.13 that the travel time between the heights of 200 and 420 km in seconds times 15 matches approximately the height of the $\beta = 1$ surface in km. In particular, the travel-time curve delineates a funnel of low β that is caused by a local magnetic flux concentration.

The region and magnetic structure considered in the present simulation is much smaller than the active region observed by Finsterle et al. (2004) and we use 20 mHz waves, instead of the 7 mHz employed by Finsterle et al. (2004). Also, by using plane parallel waves we assume the wave coherence to be always larger than the magnetic structure under investigation. Subject to these reservations, the numerical experiments carried out support the conclusions of Finsterle et al. (2004) and their proposition using high frequency waves for mapping the magnetic topography in the chromosphere.

CHAPTER 4

HEATING*

4.1 BACKGROUND

The outer envelope of our Sun is much hotter than its surface. This is contrary to our understanding that the temperature should decrease when we go away from a hot source. Clearly some additional source of heating is required to produce the temperature rise in the upper atmosphere of the Sun.

The evidence for a hotter chromosphere and corona came during the late 1930s, when Grotrian (1939) and Edlen (1942) concluded that the presence of emission lines of Fe X and Fe XIV, are due to gas at a temperature of 1 - 2 $\times$ 10^6 K. This difference in temperature between the surface and the outer atmosphere cannot be accounted by transport of thermal energy through radiation, convection or conduction as it contradicts the second law of thermodynamics. The reason for the temperature increase must be due to some non-thermal process, which maintains an energy balance between radiation and the mechanical heating. Any mechanism to explain the observations has to provide a way to inject energy at a rate that is equal to the rate of heat loss of the corona (about 6×10^{18} W). In the absence of such a heating source, the chromosphere would cool down to a state of radiative equilibrium on a radiative relaxation time of 10^3 s.

The observations of Grotrian (1939) and Edlen (1942) forced researchers to find a mechanism responsible for heating in these layers by non-thermal energy transport, such as waves or electric currents. The first such step to explain the observations was taken by Schwarzschild (1948) (also independently by Biermann 1948). He postulated that a hot corona can be maintained through heating by acoustic waves generated by the underlying

---

[*] Part of publication: Vigeesh et al. (2009)

turbulent convection zone. He proposed that the acoustic waves generated by the turbulent motions of the granules transport mechanical energy to upper layers providing ample energy to compensate the heat loss, with an upper limit of

$$E = \rho v^2 c_S \times \frac{1}{10} 4\pi R^2 = 10^{23} \text{ W} \tag{4.1}$$

where, $v = 0.5$ km s^{-1} (average granular velocity), c$_S$=7 km s^{-1} is the sound speed in the photosphere and assuming that the about 10% of the solar surface is covered with rising granules.

Photographs in Hα taken during solar eclipses show irregular spike like features called "spicules" in chromosphere with an average lifetime of around 4-5 minutes and a velocity of 30 km s^{-1}. (Roberts 1945). These observations were interpreted as superthermic jets occurring in a laterally bound region (Thomas 1948). The presence of the magnetic field and the realization of its role in heating the upper layers was initiated by the pioneering works of Alfvén (1947) who studied the effect of magnetohydrodynamic waves generated by granules. Observational evidence came from the finding that bright features in Ca II K line coincide with strong magnetic field concentrations (Babcock & Babcock 1958; Howard 1959; Leighton 1959). A comprehensive study on the heating of chromosphere and corona by magnetohydrodynamic waves in a plane parallel solar atmosphere was carried out by Osterbrock (1961). Stein (1968) estimated the fluxes generated by acoustic waves emitted from the convection zone (Lighthill-Stein mechanism) and obtained 10^3 - 10^4 W m^{-2} in agreement with Osterbrock (1961).

This and the plethora of works that followed to explain the heating have been reviewed by many authors in the field. While most the reviewers focused on a particular mechanism, a very comprehensive review describing a spectrum of different mechanisms that has been proposed was provided by Narain & Ulmschneider (1990, 1996). Some of the heating mechanisms discussed in their review act on a global scale, but some of them are very specific to certain regions of the solar atmosphere.

In Table 4.1, we provide a tabular summary of the different mechanisms that have been proposed.

4.2 INTRODUCTION TO CHROMOSPHERIC HEATING

The chromosphere, named because of the reddish ball that the sun exhibits during a solar eclipse, is hotter than the underlying photosphere. The quiet chromosphere can be qual-

Table 4.1: Various mechanisms to explain the heating of the chromosphere and corona

Mechanism	Mode of dissipation
Acoustic waves	Shocks
Fast and slow magnetoacoustic body waves	Shocks
Alfvén body waves	mode coupling, Landau damping, phase mixing
Fast and slow magnetoacoustic surface waves	Resonant absorption
Current dissipation	Joule heating, magnetic reconnection

itatively separated into magnetic and non-magnetic regions corresponding broadly with the supergranulation cell interior and magnetic network on the cell boundary respectively.

It has been proposed that, in the case of non-magnetic regions of chromosphere, acoustic wave heating by shock dissipation is the most dominant process. They form the background heating source called “basal heating” generally in stars with an outer convection zone (Schrijver 1995). This hypothesis was questioned by Judge et al. (2003) and others who claimed that intensities of Ca II lines depend on magnetic structures. The observations of Howard (1959) and Leighton (1959) had already shown that the Ca emission from the solar surface is associated with enhanced magnetic fields.

The overall radiative losses of roughly 5×10^3 W m^{-2} must be balanced by some form of heating. The chromospheric temperature rise can be thought of as due to the shock formations at these heights. The upper boundary of the chromosphere is influenced by the Lyman limit, where the complete ionization of hydrogen results in no option for further radiative cooling and hence a sudden rise in temperature. The main mechanisms responsible for chromospheric heating are still not clearly understood and an explanation of the chromospheric temperature rise is still an unsolved problem. The present consensus is that there might be more than one mechanism responsible for the temperature increase. These processes can be broadly categorized as follows:

1. Acoustic wave heated chromosphere models;
2. Indirect magnetic heating, in which the magnetic field only acts as a secondary source;
3. Direct magnetic heating by reconnections.

The first category of processes takes place in non-magnetic regions. The heating in these models is by dissipation of shocks that are formed by upward traveling acoustic wave in a stratified atmosphere (Musielak et al. 1994). The validity of these models have been questioned by several authors (Ulmschneider et al. 2005; Fossum & Carlsson 2005). The second type of process may be more realistic since they require the presence of a magnetic field which fully permeates the solar atmosphere especially in the upper regions. In Chapter 3 we showed that network fields can provide a channel to carry MHD waves generated deeper in the photosphere to higher layers, where they transfer their energy into different wave modes by mode coupling. Also network fields can excite acoustic waves in the field free regions surrounding them. These waves most likely form shocks as they propagate upwards. The quantitative estimate of the total energy that these waves carry and deposit in the higher layers will be discussed in the following sections. The third category of processes has gained some attention lately but will not be considered in the present study (Tritschler et al. 2007).

4.3 WAVE ENERGY

The MHD equations discussed in Chapter 2 expresses the conservation of mass, momentum, energy and magnetic flux. From the MHD equation, we can derive the conservation equation for the total energy, in the form:

$$\frac{\partial E}{\partial t} + \nabla \cdot J = 0 \tag{4.2}$$

where, E is the sum of the kinetic, gravitational, internal and magnetic energies per unit volume given as,

$$E = \frac{1}{2}\rho v^2 + \rho\phi + \rho e + \frac{B^2}{2\mu} \tag{4.3}$$

and ϕ is the gravitational potential defined as $\boldsymbol{g} = -\nabla\phi$ and J is the sum of the corresponding fluxes

$$J = (\frac{1}{2}\rho v^2 + \rho\phi + \rho e + p)\mathbf{v} + \frac{\boldsymbol{B}}{2\mu} \times (\boldsymbol{v} \times \boldsymbol{B}), \tag{4.4}$$

where, $e = p/\rho(\gamma - 1)$ is the internal energy of the gas per unit mass and the last term is the Poynting flux (Bray & Loughhead 1974).

Using the full non-linear expression for the energy flux, it is not easily possible to calculate the energy carried by the acoustic and magnetic waves. It has been shown by Bogdan et al. (2003) that the total flux is *dominated by a stationary but still oscillatory flow of energy that is essentially local or circulatory in character and does not contribute to the net transport of energy by wave like disturbances*. The energy density and the energy flux carried by the wave can be derived from the linearised MHD equations discussed in Chapter 3. By multiplying Eq.(3.2) with p_1/ρ_0, taking the scalar product of Eq.(3.3) with $\mathrm{v}_\mathbf{1}$ and Eq.(3.4) with $\boldsymbol{B}_\mathbf{1}/2\mu$ and multiplying Eq.(3.5) with $p_1/\rho_0 c_S^2$ and adding the resulting equations we can derive an equation for the conservation of wave energy in the form (see Chapter 6 of Bray & Loughhead 1974):

$$\frac{\partial W}{\partial t} + \nabla \cdot Q = 0 \tag{4.5}$$

where, W is the sum of kinetic energy, pressure energy and the magnetic energy associated with the wave motion given as,

$$W = \frac{1}{2}\rho_0 v^2 + \frac{p_1^2}{2\rho_0 c_S^2} + \frac{B_1^2}{2\mu}. \tag{4.6}$$

Q is the sum of the corresponding fluxes given as,

$$Q = p_1 \boldsymbol{v}_1 + [(\frac{\boldsymbol{B}_0}{\mu} \cdot \boldsymbol{B}_\mathbf{1})\boldsymbol{v}_1 - (\boldsymbol{v}_1 \cdot \boldsymbol{B}_\mathbf{1})\frac{\boldsymbol{B}_\mathbf{0}}{\mu}]. \tag{4.7}$$

In order to study how much energy is being transported by waves we need to consider the fluxes associated with the wave motion.

4.4 ENERGY TRANSPORT BY WAVES

We now consider the transport of energy in the various wave modes. Following Bogdan et al. (2003), we consider the wave flux using the expression given by Eq. (4.7) that represents the net transport of energy into the atmosphere:

$$\boldsymbol{F}_{\mathrm{wave}} = \Delta p \boldsymbol{v} + (\frac{\boldsymbol{B}_0}{\mu} \cdot \Delta \boldsymbol{B})\boldsymbol{v} - (\boldsymbol{v} \cdot \Delta \boldsymbol{B})\frac{\boldsymbol{B}_0}{\mu}. \tag{4.8}$$

The first term on the right hand side of the equality sign is the net acoustic flux, and the last two terms are the net Poynting flux. The operator Δ gives the perturbations in the variable with respect to the initial equilibrium solution and B_0 refers to the unperturbed magnetic field.

POTENTIAL FIELD

To begin with, consider the wave excitation in a potential field configuration as described in Chapter 3. We examine the energy fluxes carried away by the wave like disturbances using Eq. (4.8). Figure 4.1 shows the acoustic and Poynting fluxes at 27, 64 and 100 s after initiation of a periodic horizontal motion at $z = 0$ boundary with an amplitude of 750 m s^{-1} and a period of $P = 24$ s. The driving motion in the low-β region excites fast (acoustic) waves and slow (magnetic) waves in the region. The acoustic flux corresponds to the energy carried by acoustic wave and the Poynting flux to the energy in the magnetic mode. The sound speed in the region where the excitation takes place (low-β) is larger than the Alfvén speed, and hence the acoustic energy fluxes (Fig. 4.1a) are transported faster than the Poynting fluxes (Fig. 4.1b). As already discussed in Chapter 3, the energy transport (acoustic or Poynting) is isotropic.

Movie 4.13: Acoustic fluxes in a potential field configuration after initiation of a periodic horizontal motion at $z = 0$ boundary with an amplitude of 750 m s^{-1} and a period of $P = 24$ s .
Movie 4.14: Poynting fluxes in a potential field configuration after initiation of a periodic horizontal motion at $z = 0$ boundary .

MAGNETOSTATIC FLUX TUBE

We now consider the energy transport by wave like disturbances in a magnetostatic flux tube for the two cases discussed in Chapter 3. Figures 4.2a and 4.2b show the magnitude of the acoustic (left panels) and the Poynting flux (right panels) at 40, 60, and 80 s (from bottom to top) for the moderate field case. Since in the ambient medium the field strength is weak, the Poynting fluxes are not shown in this region. The Poynting flux is essentially the wave energy that is carried by the magnetic mode, which as expected, is localized to the flux sheet. On the other hand, the energy transport in the acoustic-like component is more isotropic. At $t = 40$ s, we find from Fig. 4.2a that the wave has just crossed the $\beta = 1$ contour. Thereafter, it propagates as a slow wave guided along the field at the acoustic speed within the flux sheet and as a fast spherical-like wave in the surrounding quasi field-free medium. Inside the flux sheet, the energy in the magnetic component (Poynting flux) and the acoustic component is of the same order of magnitude.

Movie 4.15: Acoustic fluxes in a magnetostatic flux tube with a moderate field strength after the initiation of a horizontal impulsive excitation at the lower boundary with an amplitude of 750 m s^{-1} and a period of $P = 24$ s .
Movie 4.16: Poynting fluxes in a magnetostatic flux tube with a moderate field strength after the initiation of a horizontal impulsive excitation at the lower boundary .

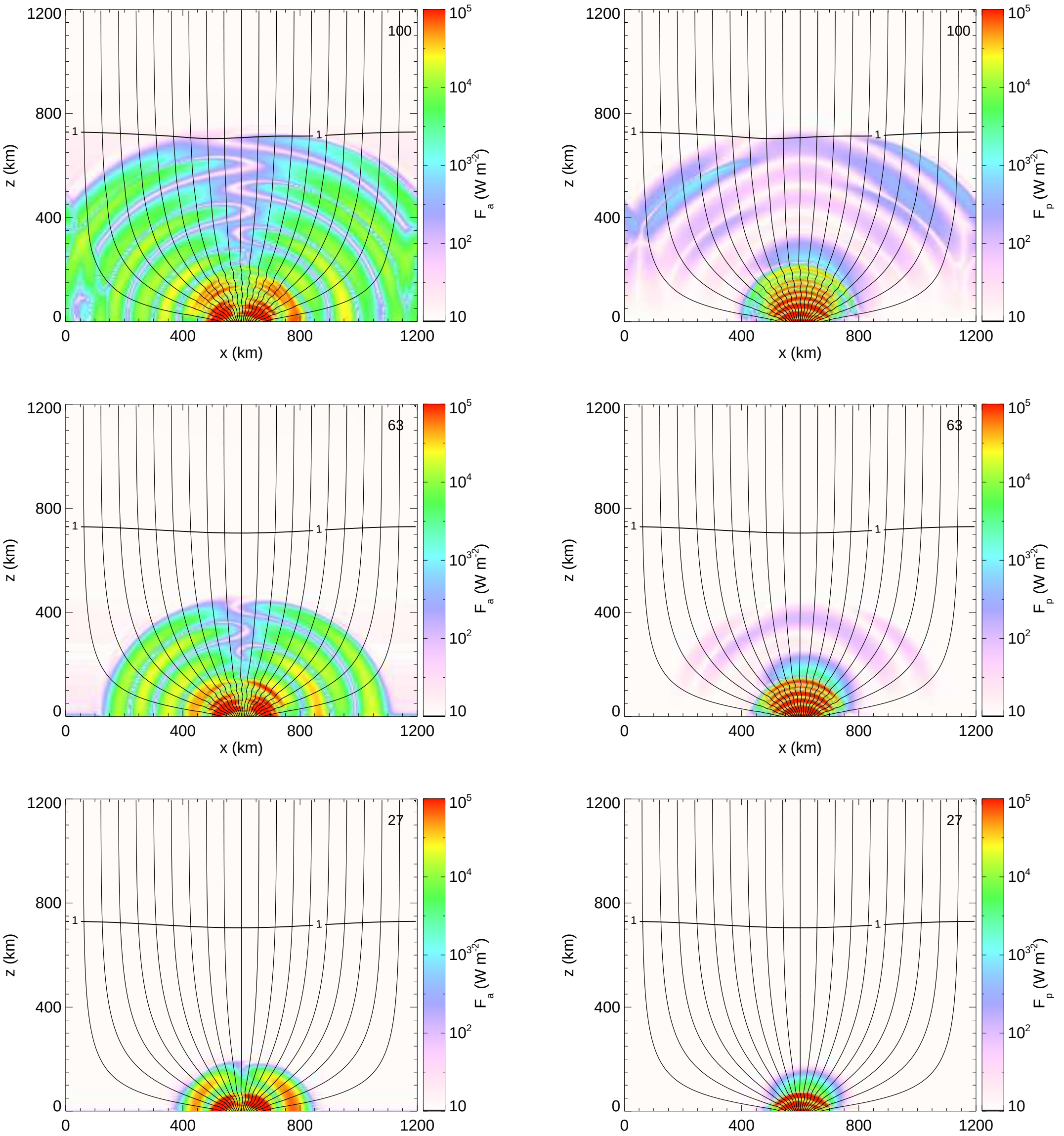

(a) Acoustic

(b) Poynting

Figure 4.1: (a) Acoustic, and (b) Poynting flux for the potential field configuration. The colours show the quantities at 27, 64 and 100 s (from bottom to top) after initiation of an periodic horizontal motion at the $z = 0$ boundary with an amplitude of 750 m s^{-1} and a period of $P = 24$ s. The thin black curves are field lines and the thick black curve represents the contour of $\beta = 1$.

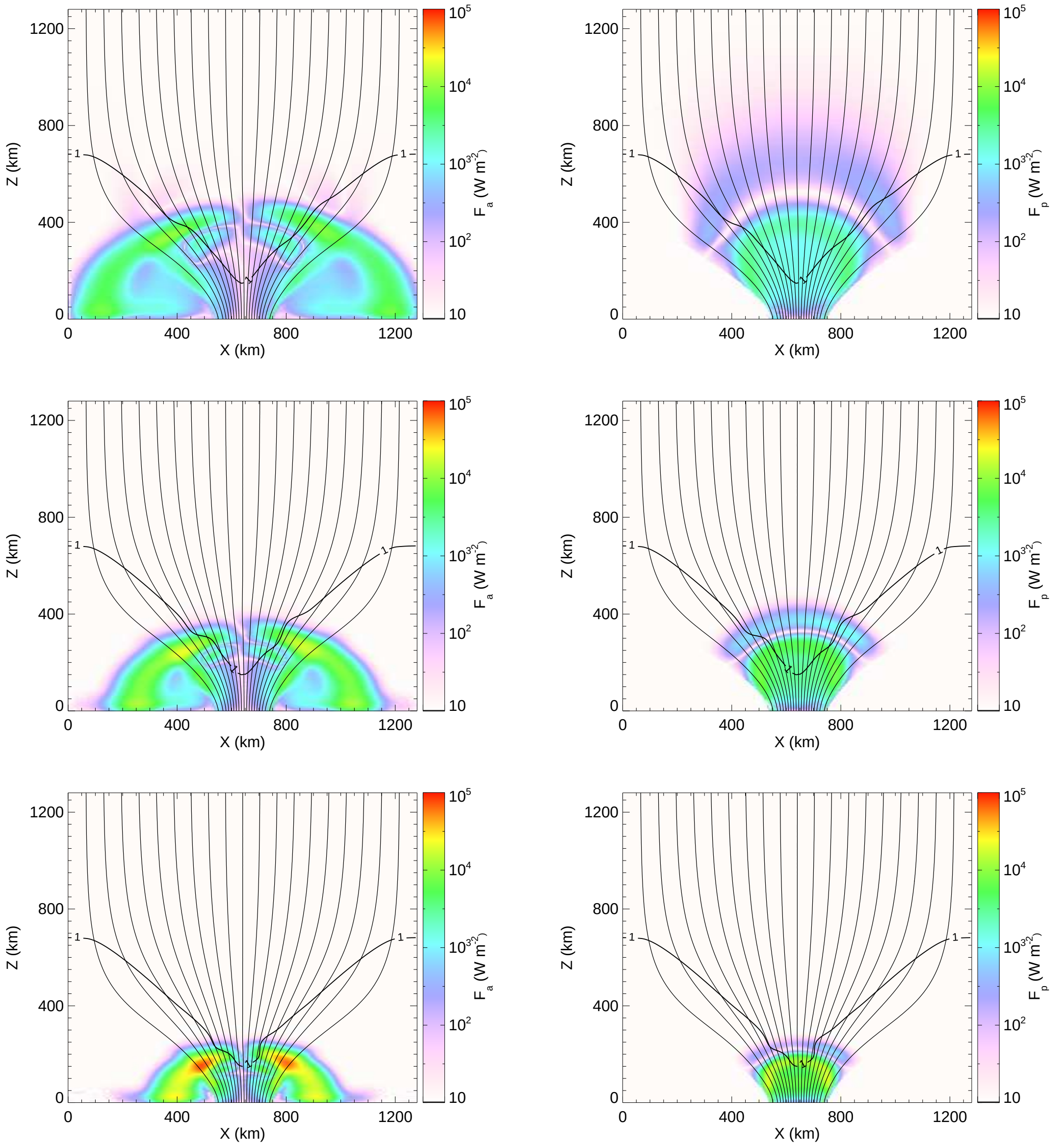

a) Acoustic

b) Poynting

Figure 4.2: Wave-energy fluxes (absolute values) for the case in which the field strength at the axis at $z = 0$ is 800 G (moderate field). The colours show (a) the acoustic flux, and (b) the Poynting flux, at 40, 60, and 80 s (from bottom to top) after initiation of an impulsive horizontal motion at the $z = 0$ boundary of a duration of 12 s with an amplitude of 750 m s^{-1} and a period of $P = 24$ s. The thin black curves are field lines and the thick black curve represents the contour of $\beta = 1$. The Poynting fluxes are not shown in the ambient medium where $B < 50$ G.

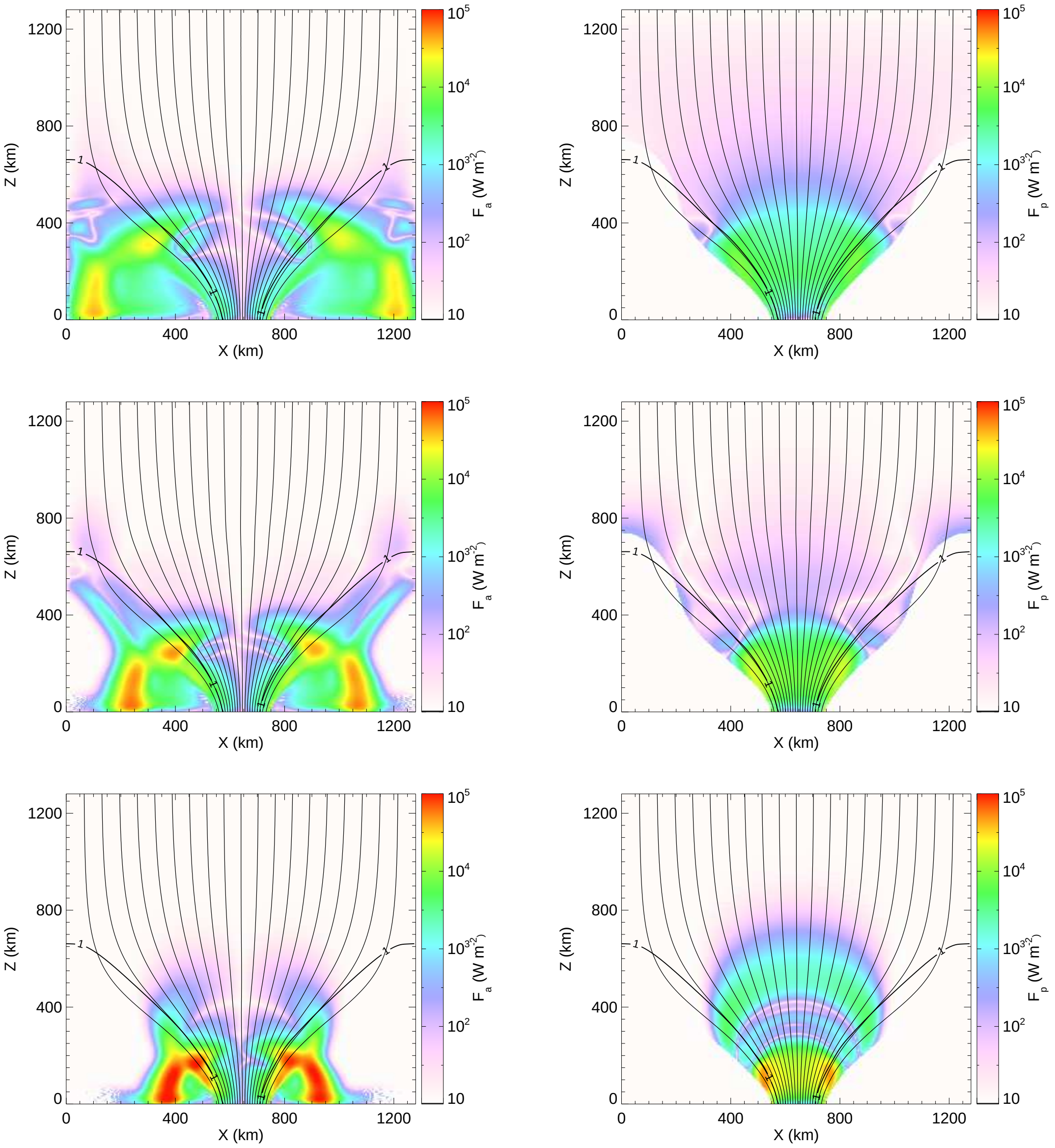

a) Acoustic

b) Poynting

Figure 4.3: Wave-energy fluxes for the case in which the field strength at the axis at $z = 0$ is 1600 G (strong field) for times $t = 40$, 60, and 80 s. The coding corresponds to that of Fig. 4.2. The Poynting fluxes are not shown in the ambient medium where $B < 200$ G.

Movie 4.17: Acoustic fluxes in a magnetostatic flux tube with a strong field strength after the initiation of a horizontal impulsive excitation at the lower boundary with an amplitude of 750 m s^{-1} and a period of $P = 24$ s .

Movie 4.18: Poynting fluxes in a magnetostatic flux tube with a strong field strength after the initiation of a horizontal impulsive excitation at the lower boundary .

A comparison of these results with those for the strong field case (Fig. 4.3) shows that in the latter case energy is transported by the fast wave much more rapidly, especially in the central regions of the flux sheet. This is due to the sharp increase of the Alfvén speed with height above $z > 200$ km. At $t = 40$ s we find that the wave front associated with the magnetic component has already reached a height of about 500 km (close to the sheet axis), while the acoustic wave reaches this level only at about $t = 80$ s.

From the contour plots of Figs. 4.2 and 4.3, we see that the fluxes in the ambient medium for the strong field case is still close to 10^5 W m^{-2}, while for the moderate field, it is almost an order of magnitude less, suggesting that the flux sheets with strong fields are a more efficient source of acoustic fluxes into the ambient medium. The "mode transmission" from fast (acoustic) to slow (acoustic) that takes place in the case of a moderate field, as explained in Sect. 3.2.3, can be seen in Fig.4.2a. Since the "attack angle" in this case is close to zero, a significant amount of acoustic transmission takes place across the layer of $\beta = 1$ (Cally 2007). Another feature that we see in the plots of wave-energy fluxes is the "mode conversion" that takes place in the strong field case. The fast magnetic wave, which is generated inside the flux sheet can travel across the magnetic field. This mushroom like shape, which is expanding, can be easily discerned in the 40 s snapshot of the Poynting flux shown in Fig. 4.3b. As this wave crosses the $\beta = 1$ contour, it is converted into a fast (acoustic) wave. The wing like feature that can be seen in the 60 s snapshot of the acoustic fluxes (Fig. 4.3a) are due to the fast waves that have just undergone a "mode conversion" from magnetic to acoustic.

Next we consider a field line to the left of the flux sheet axis, which encloses a fractional flux of 50%. The field aligned and the normal component of the wave-energy fluxes are calculated along this particular field line. Figs. 4.4 and 4.5 shows the positive, field aligned component of acoustic flux for the moderate and strong field case as a function of time and spatial coordinate z along the field line. The dotted curves in the figure show the space time position of a hypothetical wavefront that travels with Alfvén speed (steeper slope) and sound speed along this magnetic field line. With the help of this plots it is easy to separate the energy fluxes in the slow and the fast wave modes. The evolution of the $\beta = 1$ layer is shown for the moderate field case. The perturbation of this layer as the wave crosses it can be seen clearly around 40 seconds. It moves down due to the decrease in pressure caused by the rarefaction front and then moves up when the compression front passes it. A major fraction of the flux lies parallel to the line that corresponds to the hypothetical acoustic wave, which is a slow mode in the region where $\beta < 1$. In the strong field case, above approximately $z = 800$ km and for epochs $t \gtrsim 120$ s, the acoustic flux carried in the compressive (trailing) phase starts to catch up the slightly slower moving expansive

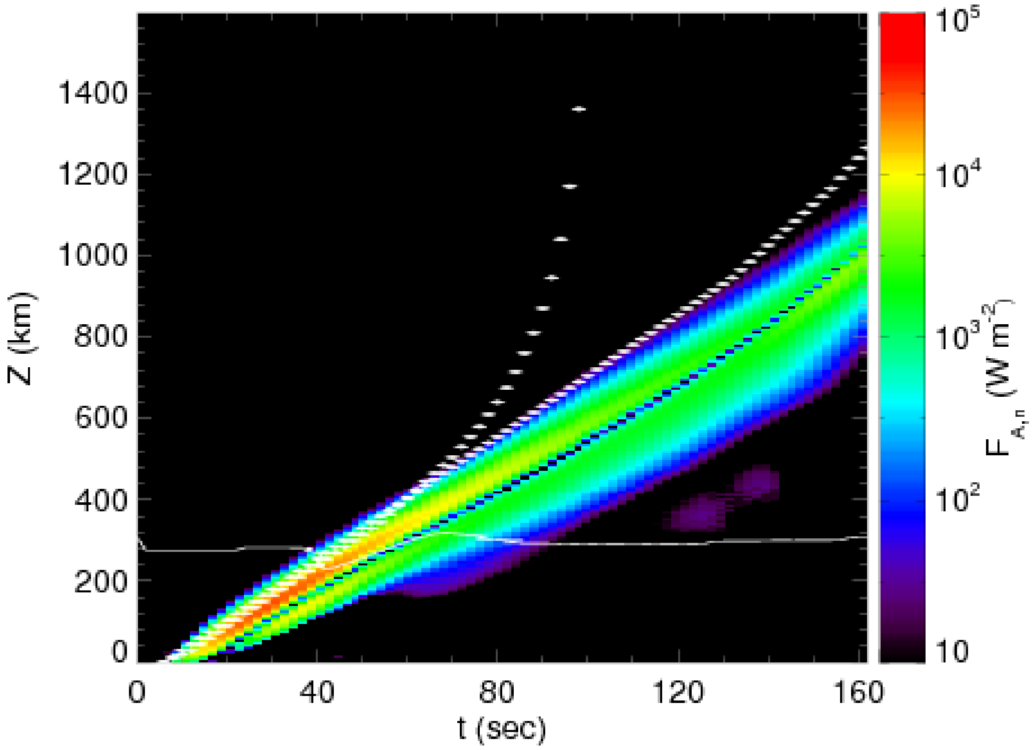

Figure 4.4: The field aligned positive (upwardly directed) component of acoustic wave-energy flux as a function of time on a field line on the left side of the axis that encloses a fractional flux of 50% for the case in which the field strength at the axis at $z = 0$ is 800 G (moderate field).

Table 4.2: Temporal maximum of the horizontally averaged, vertical component of the wave-energy fluxes (in units of 10^3 W m^{-2}).

	$F_{A,z}$ (10^3 W m^{-2})			$F_{P,z}$ (10^3 W m^{-2})		
Initial Excitation	z = 100 km	z = 500 km	z = 1000 km	z = 100 km	z = 500 km	z = 1000 km
0.75 km s^{-1}, 24s	11.36	1.96	1.33	29.38	1.08	0.14
0.75 km s^{-1}, 120s	35.75	27.70	4.02	134.29	0.79	0.07
0.75 km s^{-1}, 240s	20.90	8.58	3.30	131.84	0.36	0.02
1.50 km s^{-1}, 24s	44.55	7.68	3.34	115.79	4.29	0.57
3.00 km s^{-1}, 24s	168.41	30.40	6.22	434.03	16.90	2.31

phase and the flux gets confined into a narrow shock forming region. This is also visible in the case of the moderately strong field. This behaviour is not present along the corresponding field line to the right of the sheet axis (not shown here), where the compressive phase is leading so that the compressive and expansive phase of the perturbation slightly diverge with time. The acoustic fluxes are of the order of 10^4 W m^{-2}. The Poynting

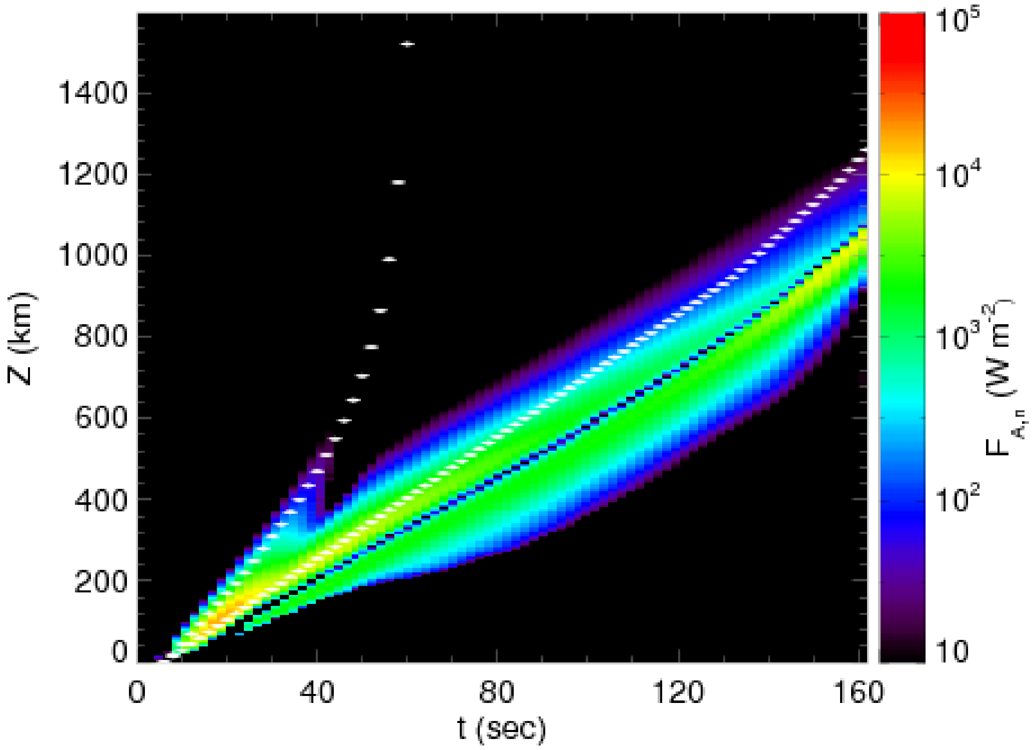

Figure 4.5: The field aligned positive (upwardly directed) component of acoustic wave-energy flux as a function of time on a field line on the left side of the axis that encloses a fractional flux of 50% for the case in which the field strength at the axis at $z = 0$ is 1600 G (strong field).

fluxes carried by the fast mode in this region can be identified by the coloured contours that gather along the dotted lines corresponding to the hypothetical Alfvén wave (Fig. 4.6 & 4.7). Comparing the two fluxes, it is clear that the acoustic flux carried by the slow mode is larger than the Poynting flux, especially in the moderate field case. The Poynting flux rapidly weakens with time and height because it is not guided along the field lines like the slow mode but rapidly diverges across the field and part of the Poynting flux gets converted to acoustic again as explained in Sect. 3.2.3. Also from Figs. 4.6 & 4.7 it can be seen that while the magnetically dominated fast mode starts right from the excitation level at $z = 0$ in the strong field case, it starts in the weak field case only after about 40 s when the fast acoustic wave reaches the conversion layer where $\beta \approx 1$ and undergoes partial mode conversion. Therefore, the fast (magnetic) mode is from the beginning weaker in the moderate as compared to the strong field case.

Table 4.2 shows the temporal maximum of the horizontally averaged vertical compo-

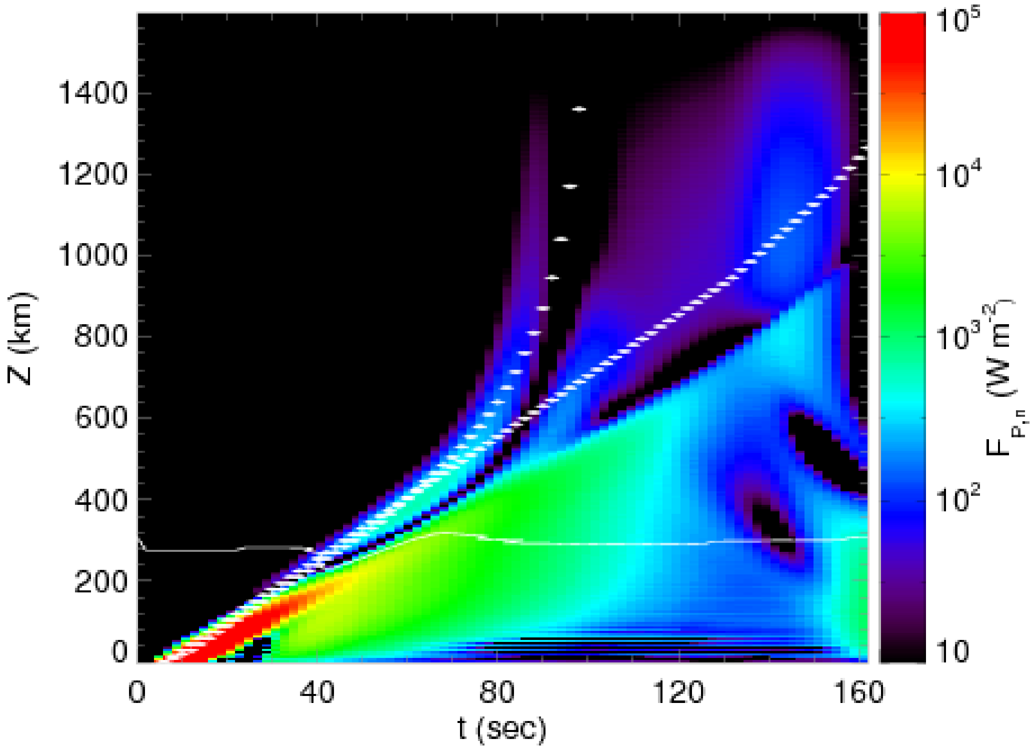

Figure 4.6: The field aligned positive (upwardly directed) component of the Poynting flux as a function of time on a field line on the left side of the axis that encloses a fractional flux of 50% for the case in which the field strength at the axis at $z = 0$ is 800 G (moderate field).

nents of acoustic and Poynting fluxes at three different heights for the strong field case. We have considered three different amplitudes and periods for the initial excitations. Although the field aligned acoustic fluxes on the specific field line considered in Figs. 4.4 & 4.5 reach values of the order of 10^4 W m^{-2} at a height of $z = 1000$ km, the horizontally averaged fluxes are typically an order of magnitude less, depending upon the amplitude of the initial excitation. The Poynting fluxes shown in the table are the maximum value that the fluxes reach in the interval between the start of the simulation until the time when the fast wave reaches the top boundary (around 60 s). Hence these fluxes correspond to the fast mode for $z = 500$ km and $z = 1000$ km, since within this time limit the slow mode has not yet reached these heights. The Poynting fluxes associated with the fast mode are relatively lower in magnitude compared to the acoustic fluxes. It should be noted that there is also considerable Poynting flux associated with the slow mode, since these waves also perturb the magnetic field. The acoustic fluxes of the moderate field case reach only

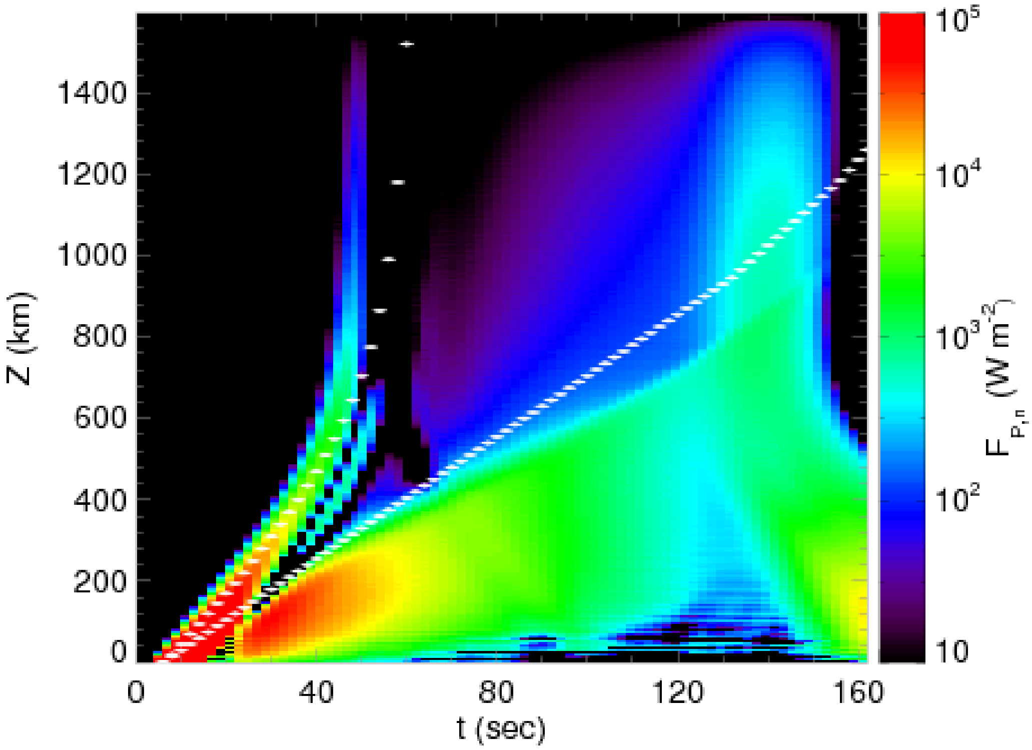

Figure 4.7: The field aligned positive (upwardly directed) component of the Poynting flux as a function of time on a field line on the left side of the axis that encloses a fractional flux of 50% for the case in which the field strength at the axis at z = 0 is 1600 G (strong field).

less than 70% of that of the strong field configuration and the Poynting fluxes are negligible in in this case. But, it is lower than the Poynting flux that is transported with the fast mode as can be seen from Fig. 4.7.

4.4.1 EFFECTS OF THE BOUNDARY-LAYER WIDTH

We now study the acoustic emission of the magnetic flux concentrations into the ambient medium by varying the width of the boundary layer between the flux sheet and ambient medium. This is carried out by comparing the result of simulations with a sharp interface of width 20 km to that with a width of 80 km (see Fig. 2.11), where the width can be varied by choosing appropriate values of ψ_1 and ψ_2 in Eq. (2.28).

We examine the acoustic emission from the two peripheral (control) field lines to the left and to the right of the flux-sheet axis that encompass 90% of the magnetic flux. These

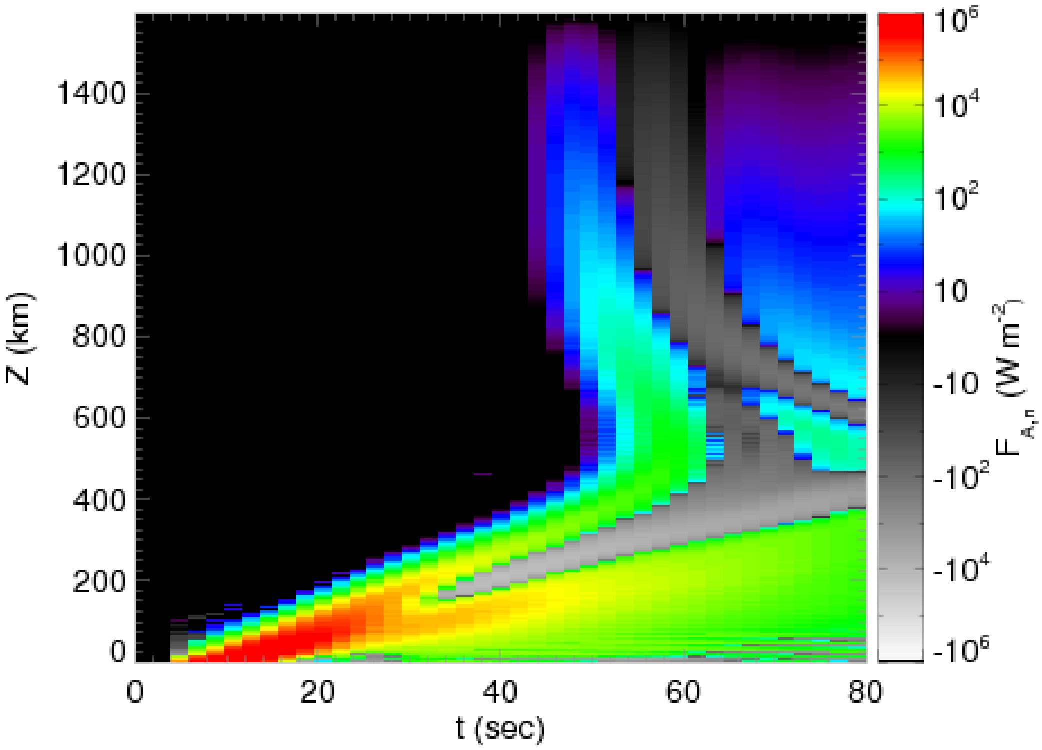

Figure 4.8: Acoustic flux perpendicular to the peripheral field lines that encompass 90% of the magnetic flux as a function of time and height along the field line for a strong field case with a sharp interface between flux-sheet interior and ambient medium. Only the outwardly directed flux is shown.

correspond to the outermost field lines that are plotted in Figs. 3.4 to 4.3. These field lines are located in the high-β region with $\beta >> 1$, all the way from the base to the merging height, where the flux sheet starts to fill the entire width of the computational domain. The acoustic emission from the peripheral field line to the right and to the left of the flux-sheet axis is practically identical.

Figures 4.8 and 4.9 shows the acoustic emission from the flux sheet into the ambient medium for the peripheral field line to the left of the flux sheet with the strong field (B_0 = 1600 G) and the cases of the sharp interface (Fig. 4.8) and the wide interface (Fig. 4.9). Concentrating on the case with the sharp interface first, we see that acoustic flux is initially generated by the fast mode that stems from the transversal motion of the flux sheet to the right hand side, which causes a compression and expansion to the right and left side of the flux-sheet edge, respectively. This movement generates a net acoustic flux away from the flux sheet on both sides. It is visible in Figs. 3.6 and 4.3 as the shell-

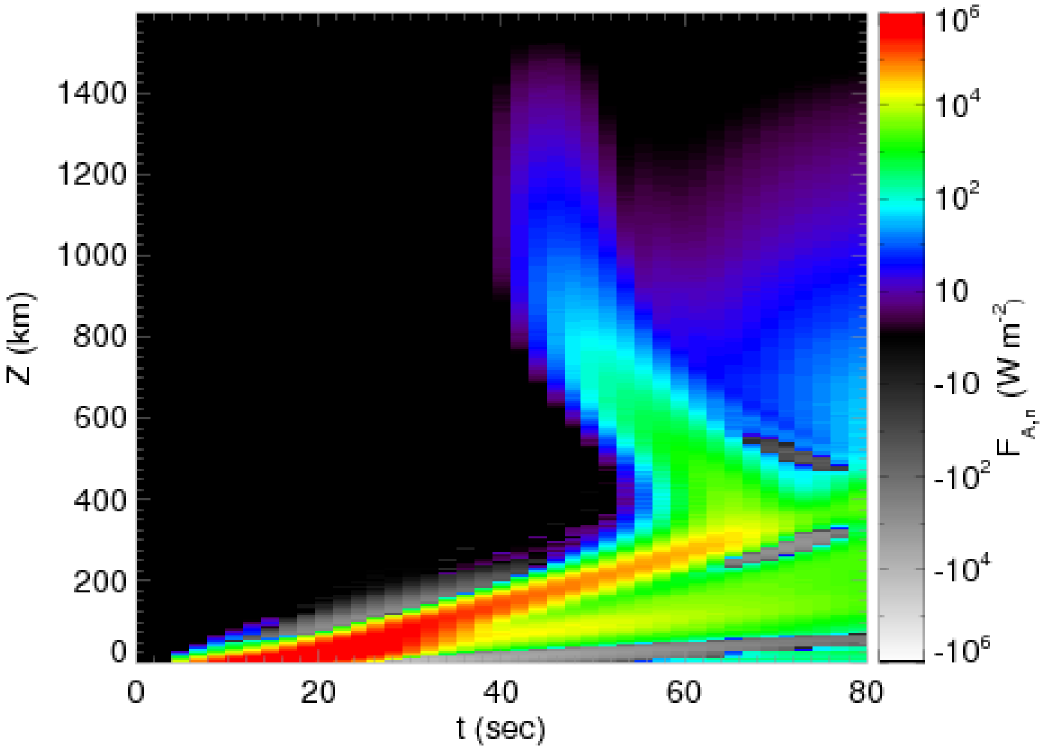

Figure 4.9: Acoustic flux perpendicular to the peripheral field lines that encompass 90% of the magnetic flux as a function of time and height along the field line for a strong field case with a wide interface between flux-sheet interior and ambient medium. Only the outwardly directed flux is shown.

like antisymmetric wave that emanates from the base of the flux sheet propagating into the ambient medium. At a height of z = 100 km the peak value of this flux is 3×10^5 W m^{-2} for the sharp interface but only 1.2×10^5 W m^{-2} for the wide interface. This is because the sharp interface acts like a hard wall that pushes against the ambient medium, while for the wide interface the action is less intense.

Near the flux-sheet boundary this wave seamlessly connects to the tips of the crescent-like fast (magnetic) mode of the flux-sheet interior as can be best seen when comparing the first two snapshots of Figs. 3.6 and 3.7b. There, acoustic flux is generated by continuous leakage and conversion from the magnetic mode, giving rise to the steeper of the two horizontally running, inclined ridges of acoustic flux, visible in the lower part of both Figs. 4.8 & 4.9. This leakage is more efficient in the case of the wide interface than in the case to the sharp interface so that the corresponding ridge extends over a longer period of time in the former compared to the latter case. However, it cannot compensate for the larger initial flux that emanates from the more confined (sharp) boundary.

Starting at about $t = 25$ s in case of the sharp interface, one can see a less steep and weaker branch of acoustic flux that is connected to the slow (magnetic) mode that propagates in the high-β boundary-layer of the flux sheet. Obviously it creates a non-negligible source of acoustic flux to the ambient medium. It is also present in case of the wide interface.

The two horizontally running ridges of acoustic flux in the case of the sharp interface (Fig. 4.8) is slightly more inclined compared to the case with the wide interface (Fig. 4.9), where the peripheral (control) field line expands more in the horizontal direction so that the wave travels a longer distance to reach it.

At approximately $t = 45$ s we start to see acoustic flux appearing at a height of about $z = 1000$ km. This flux originates from the refracted fast (magnetic) wave within the flux sheet. Since this wave quickly accelerates and refracts with height, it reaches the flux-sheet boundary sooner at $z = 1000$ km than in the height range $500 \text{ km} < z < 800$ km. This wave undergoes conversion from fast, predominantly magnetic to fast, predominantly acoustic as it crosses the region where $\beta = 1$. Because it travels essentially perpendicular to the field near the flux-sheet boundary, the conversion is particularly efficient. While this ridge of acoustic flux originates from the leading phase of the fast (magnetic) wave that corresponds to a movement to the right (red big crescent in the 40 s snapshot of Fig. 3.7b), a second, parallel running negative ridge, stems from the following phase, corresponding to a movement to the left (blue crescent in the 40 s snapshot of Fig. 3.7b).

Table 4.3 shows the total acoustic emission to the ambient medium, still from and perpendicularly across the field lines that encompasses 90% of the total magnetic flux for cases with 3 different boundary layer widths. The energy is computed by integration of the perpendicular flux along the peripheral control field lines to the left and to the right over the full height range of the computational domain and from $t = 0$ s to $t = 64$ s for unit width. The total acoustic energy leaving the flux sheet with the wide interface is only 35% of that with the sharp interface. In this sense, a flux sheet with a sharp interface is more efficient in providing acoustic flux to the ambient medium than a flux sheet with a wide interface as conjectured by Hasan et al. (2005).

4.5 ENERGY TRANSPORT AND DISSIPATION

The energy losses in the magnetic network at chromospheric heights are of the order of 10^4 W m^{-2}. Even though the acoustic energy flux produced by the transverse excitation

Table 4.3: Total acoustic emission from the flux sheet into the ambient medium for different boundary layer widths.

Boundary-layer width	Total acoustic emission (10^{11} J m^{-1})
20 km (sharp)	23.40
40 km (medium)	13.22
80 km (wide)	8.13

movement can temporarily reach this value at certain locations, the spatially averaged values in Table 4.2 show that the acoustic energy flux generated in our model cannot balance the energy losses. This conclusion is borne out by the fact that the values of Table 4.2 are temporal maxima: the temporal mean would be lower. Recent observations of the chromospheric network are suggestive of Ca II network grains associated with plasma with quasi-steady heating at heights between 0.5 and 1 Mm inside magnetic flux concentrations (Hasan & van Ballegooijen 2008). In order to be compatible with the observed quasi-steady Ca emission the injection of energy needs to be in the form of sustained short duration pulses as argued by (Hasan & van Ballegooijen 2008) but these pulses could probably not maintain the maximum values of acoustic flux quoted in Table 4.2.

Possibly with the exception of the case corresponding to the last row in Table 4.2, the transverse excitation considered here correspond to the “random walk phase” of the model by Cranmer & van Ballegooijen (2005). Excitations corresponding to the “jump phase” with even higher velocity amplitudes than considered in the present paper might temporarily be capable of providing the required energy flux. However, with a mean interval time of 360 s these jump events are probably not responsible for the heating observed in Ca II network grains, which requires a more steady or high frequency source.

We have not considered photospheric radiative losses, which would damp the waves before they reach chromospheric heights (Carlsson & Stein 2002). If these radiative losses are taken into account, the fluxes would be lowered further. Also not all of the acoustic energy flux would be available for balancing the radiative energy loss in the chromosphere depending on the details of the NLTE process. This implies that acoustic waves generated by transverse motions of the footpoints of magnetic network elements cannot fully match the chromospheric energy requirements of network regions.

This conclusion cannot be expected to drastically change when turning to three spatial dimensions. The details of the mode coupling and the partition of energy fluxes to the various modes would become more complex but the share of energy that resides in the acoustic mode is unlikely to be much larger than in the two-dimensional case. On the contrary, the energy flux generated at the footpoint of the magnetic element would have to be distributed to a larger area in three spatial dimension so that the spatial mean at z = 1000 km would probably be lower.

Multiple excitation can form shocks that follow and overtake one another, thereby increasing the shock strength and hence the dissipation. Our simulation results show that, among the fluxes associated with the slow mode, the Poynting fluxes dominate over the acoustic fluxes by an order of magnitude. The shock dissipation of Poynting fluxes associated with slow shocks can be a possible candidate for contributing to the enhanced emission in the network.

We have only considered single, short duration, transverse pulses for the wave excitation. A more realistic driver with sustained pulses of varying lengths, velocities, and time intervals would give rise to highly non-linear dynamics, which might yield increased acoustic fluxes. Also we have not considered longitudinal wave excitation, which would be available primarily from global p-mode oscillations. The latter are expected to provide low frequency slow mode waves to the outer atmosphere via magnetic portals in the presence of inclined strong magnetic fields, where they would be available for dissipation through shock formation (Michalitsanos 1973; Suematsu 1990; Hansteen et al. 2006; Jefferies et al. 2006). In fact, this mechanism would also work in the periphery of a vertically oriented flux tube, where the field is strongly inclined with respect to the vertical direction. Another source of energy that was not considered here may come from direct dissipation of magnetic fields through Ohmic dissipation.

CHAPTER 5

SYNTHESIS OF SPECTRAL LINES*

The information about the Sun's atmosphere comes from the interpretation of the spectrum of light it emits. The spectral lines are generally studied to get insight into the properties of the atmosphere in which they are formed. The magnetic fields in the atmosphere of the sun adds its imprint on lines by modifying polarization state of the light emerging from the surface. A wealth of information about the structure and dynamics of the magnetized regions of sun is hidden in the polarized light. The polarization of light is described by specifying the direction of the electric field of the electromagnetic wave. Sir George Gabriel Stokes in 1852 introduced a convenient way to parametrize the polarization of light. He introduced four parameters (called Stokes parameters), which completely specify the polarization state of light. The four Stokes parameters are denoted as *I, Q, U* and *V* and defined as,

$$
\begin{aligned}
I &= \frac{I}{I_c}, && (5.1)\\
Q &= \frac{I_x - I_y}{I_c}, && (5.2)\\
U &= \frac{I_a - I_b}{I_c}, && (5.3)\\
V &= \frac{I_l - I_r}{I_c}. && (5.4)
\end{aligned}
$$

where I is the intensity of the light in that wavelength, I_c is the intensity of the continuum, I_x and I_y are the intensity of the linearly polarized light from a orthogonal linear polarizers. I_a and I_b are the linearly polarized light from the above orthogonal linear polarizers

---

*In preparation

turned 45°. I_l and I_r are the left and right circular polarized intensities.

The theory of line formation in the presence of magnetic field was first worked out by Unno (1956) and Rachkovsky (1962). Staude (1972) showed that in the case of magnetoactive line formation, different Stokes components are formed at different height in the magnetized atmosphere, which might help in constructing magnetic vector field in the regions where these different lines are formed. The formation heights of the Stokes parameters for different LTE lines originating in photospheric umbral region were studied by Wittmann (1974) and Grossmann-Doerth et al. (1988b). Gurtovenko et al. (1974) pointed out the importance of accurate values of the average optical depth of formation of Fraunhofer lines to study the depth dependent effects like motions, magnetic fields, damping effects etc., arguing that a clear distinction should be made in photospheric regions of the origin of the "emergent radiation" and the region where the "line depression" is mainly formed. The depth of formation of a spectral line can be studied using the contribution function which gives the relative contribution of the different atmospheric layers to the observed quantity. The contribution function of the emergent radiation and the contribution function of the line depression are not the same. In case of a weak line, the contribution function of the emergent radiation is the same for different lines. On the other hand, the contribution function of the line depression varies considerably for strong lines, showing that analysis based on the line depression is more reliable for studying depth variation of velocities, magnetic field and other properties of the atmosphere rather than the contribution function of the emergent intensity. Landi Degl'Innocenti & Landi Degl'Innocenti (1977) introduced the concept of "response function" for the Stokes parameters. A response function measures the response of some observed quantity to a given perturbation. Depth of formation of a spectral line can be studied in two different ways; using the contribution function and response function, depending upon the problem (Magain 1986). For instance the effect of a temperature fluctuation effects the response function rather than the contribution function. Polarized light emerging from the magnetic regions makes it more difficult to interpret the contribution function and response function. A more precise way in terms of Magain (1986)'s argument over the importance of "line depression" over "emergent intensity" prompted Grossmann-Doerth et al. (1988a) to derive the Stokes "line depression" contribution function and also the response function. The Stokes line depression response function can be used to study the effect of temperature perturbations, velocity fields etc. in a magnetized atmosphere.

5.1 STOKES *V*

Present telescopes are still not capable of resolving small scale magnetic structures completely. Observations in Stokes I alone cannot fully reveal properties of the magnetic features, since the contribution to the I profile not only comes from the magnetic field but also from the surrounding plasma. But Stokes V profiles give us the properties of the polarized light that emerge only from the magnetic structures. So the most sensitive method to study the magnetic atmosphere is by analysing the Stokes V spectra emerging from them (see for a review Sigwarth 2000).

ASYMMETRY OF STOKES *V*

Under LTE conditions, the Stokes V profile is antisymmetric with respect to the zero crossing wavelength λ_V and profiles are unshifted with respect to the position of the line core in Stokes I (Auer & Heasley 1978). Auer & Heasley (1978) discussed the transfer equation for polarized light using *Mueller matrices* and argued that the symmetries present in a static atmosphere results in a zero net circular polarization and thereby the profiles remain unshifted. Using the Fourier Transform Spectrometer (FTS) as a polarimeter at the Kitt Peak McMath Telescope, Stenflo et al. (1984) showed that there is a net circular polarization in plages and network regions. But observations by Stenflo & Harvey (1985) did not show any zero-crossing shift. The asymmetries between the red and blue wing amplitudes (a_r and a_b) and areas(A_r and A_b) defined as,

$$\text{amplitude asymmetry} \quad \delta a = \frac{|a_b| - |a_r|}{|a_b| + |a_r|} \tag{5.5}$$

and

$$\text{area asymmetry} \quad \delta A = \frac{|A_b| - |A_r|}{|A_b| + |A_r|} \tag{5.6}$$

cannot be explained by static models. Figure 5.1 illustrates a typical asymmetric Stokes V profile with the various quantities used to quantify the asymmetry. At disc centre the amplitude and area of the blue wing is larger than that of the red wing, that is both δa and δA are positive with $\delta a > \delta A$ especially for Fe I lines (Solanki & Stenflo 1984).

Several authors proposed different mechanisms to explain the observed asymmetry. These included effects due to gradients in velocity and magnetic field along the line of sight within the magnetic element, or velocity gradients along the line of sight passing through a inclined magnetic field, or oscillations within the unresolved element, or even due to departures from LTE (see Solanki 1993). Using a 1-D model, Solanki & Pahlke

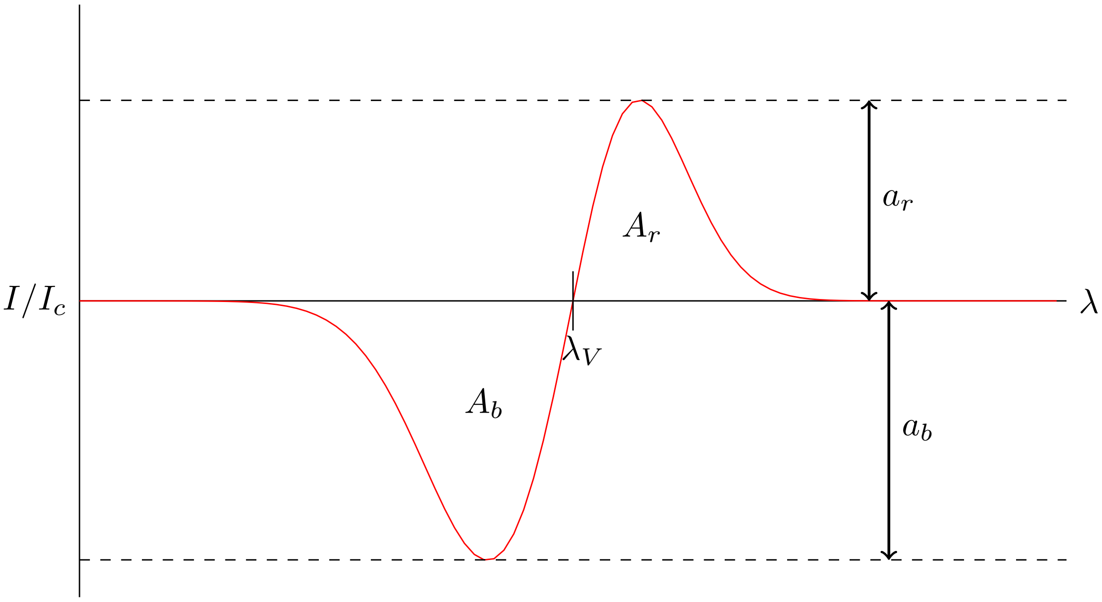

Figure 5.1: Illustration of an asymmetric Stokes *V* profile. A_r and A_b are the areas and a_r and a_b are the amplitudes of the red and blue lobes respectively. λ_V is the zero crossing wavelength.

(1988) showed that a positive asymmetry cannot be contemplated without a stationary flow. Grossmann-Doerth et al. (1988b, 1989) showed that the observed area asymmetry without a shifted Stokes λ_V can occur when a line of sight traverses both a static magnetic and a spatially separated, field-free region in motion. But later observations by Grossmann-Doerth et al. (1996) and others showed that the Stokes *V* profiles are highly asymmetric and also show strong zero crossing shifts. The numerical simulation by Steiner et al. (1998) showed significant velocities within the flux tube which could explain the zero crossing shifts. Observations (Sigwarth et al. 1999) with $0.8''$ resolution showed that a variety of asymmetrical profiles existed and even some of them were extremely asymmetric. Steiner (2000) gave a comprehensive atlas of variety of asymmetric Stokes V profiles formed due to line of sights containing two components with different magnetic and velocity properties, occur in the presence of a magnetopause.

FORMATION OF ASYMMETRIC STOKES *V* PROFILE

One of the many ways in which a asymmetric Stokes *V* profile can originate is when the line-of-sight traverses a two layer atmosphere with different flow and magnetic properties. We borrow the configuration described by Steiner (2000) to explain the formation of an asymmetric Stokes V profile. In their model the atmosphere is divided into two layers at an optical depth of τ_1. The bottom layer is field-free and extends from $\tau = \tau_1$ to $\tau = \infty$. The material in this layer has velocity with a line of sight component v_s. The top layer is embedded with a magnetic field but without any flows and it extends from $\tau = \tau_1$ to $\tau = 0$. Depending upon the flow velocities of the bottom layer, the absorption line emerging from this layer is Doppler shifted with respect to the symmetry axis of the two Zeeman component of the same line formed in the top layer. This leads to the partial suppression of the polarization signal in the direction of the Doppler shift leading to an asymmetry. The graphical account of the formation of an asymmetric Stokes V profile as described by Steiner (2000) is depicted in Fig. 5.2. Inspired by the observations and numerical simulations and driven by the need to find possible observational signatures of wave propagation and various other features that has been discussed in the earlier chapter, we have attempted to study the feasibility of using the Stokes profiles obtained from our simulation to diagnose waves. In what follows, we have tried to explain the various properties of the emergent Stokes profiles associating it with the two layer model of Steiner (2000). Extremely asymmetric profiles can also be formed when regions of opposite polarity and of different flow properties are within a single resolution element.

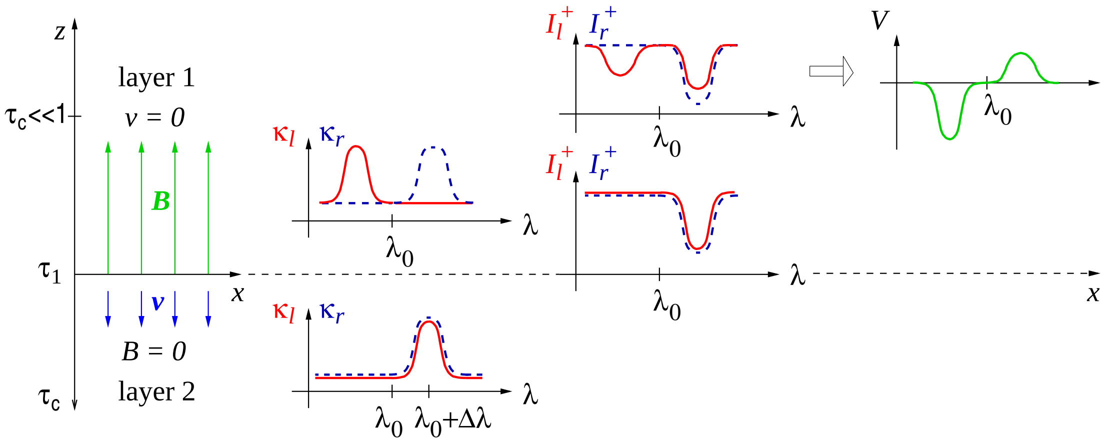

Figure 5.2: The formation of an asymmetric Stokes V profile (green curve) in an atmosphere with two layers of separate flow and magnetic properties. The magnetopause is located at optical depth τ_1. I denotes the intensity and κ denotes the opacity, r;l denote the right (blue-dashed curve) and left (red-solid curve) circularly polarized light. The Doppler shift in the layer 1 results in suppression of the red-lobe leading to an asymmetric Stokes V profile. *(Courtesy of Steiner 2000)*

Table 5.1: Atomic parameter of the selected lines

Ion	Wavelength (Å)	Excitation Potential (eV)	log(gf)	g_{eff}	Lower Level	Upper Level
Fe I	5250.21	0.121	-4.938	3.0	$^5D_0$	$^7D_1$
Fe I	5247.05	0.087	-4.946	2.0	$^5D_2$	$^7D_3$
Fe I	6301.50	3.654	-0.718	1.67	$^5P_2$	$^5D_2$
Fe I	6302.49	3.686	-1.235	2.5	$^5P_1$	$^5D_0$

5.2 STOKES *V* SYNTHESIS AND DIAGNOSTICS

We have computed the emergent Stokes *V* profiles from the top of our simulation box for the case of a photospheric flux tube with field strength of 1000 G and 1600 G using the Stokes profile code DIAMAG (Grossmann-Doerth et al. 1988a). This numerical code calculates the normalized Stokes parameters by solving the Unno-Rachkovsky equations. The Stokes parameters for each wavelength are obtained by integrating the “line depression” contribution function. The program requires the temperature, gas pressure, magnetic field strength, velocity to be specified on every grid point along the line of sight to calculate the opacities. The calculations were done for a set of four Fe I lines viz. 5250.2 Å, 5247.05 Å, 6301.5 Å, 6302.5 Å. The atomic parameters of the selected lines are listed in Table 5.1.

The Table 5.1 lists the wavelengths of the lines, the excitation potentials of the lower level, oscillator strengths (log (gf)) and the effective Landé g-factor (g_{eff}). The two pairs of lines were selected due to the fact that they are formed under similar conditions in the atmosphere, since they have similar excitation potential and oscillator strengths, which means very similar opacities. But the difference in Landé g-factor for these lines makes them useful for measuring the magnetic field strength. These lines are very commonly used to study solar magnetic field through the line ratio technique (Stenflo 1973). Socas-Navarro et al. (2008) have confirmed the reliability of using these four lines for the diagnostics of quiet sun magnetic field. Effect of propagating waves on the Stokes *V* profiles of Ca II infrared triplet were studied by Pietarila et al. (2006). They saw a clear time-dependent behaviour of the Stokes *V* profiles as a result of wave propagation and shock formation occuring in the numerically simulated atmosphere. Even though they were able to reproduce the atmospheric dynamics in the form of observational signatures in the Stokes profile, their work was limited to the weak field case. The effect of varying magnetic field in the atmosphere and the spectral signatures of wave propagation in these model have not been studied so far.

We have attempted a study of the atmospheric dynamics in atmospheres containing magnetic structures with varying field strength. In order to study the effects of wave propagation in the four Fe I lines, we use snapshots of the numerical simulation runs discussed in Chapter 3. The Stokes spectra for every vertical line-of-sights separated by a distance of 10 km were computed for each time step. Here we present the analysis of the Stokes *V* spectra for the two cases with a moderate and a strong field case.

5.2.1 MODERATE FIELD CASE

The Stokes *V* profiles were computed along vertical lines of sight by integration of the radiative transfer equation for polarized light. The profiles emerging from the top boundary were spatially averaged spanning the whole width of the box. This is illustrated in Fig. 5.3. The top middle panel in Fig. 5.3 shows the spatially averaged Stokes *V* profiles for the whole width of the simulation (1280 km). The snapshot of temperature perturbation (ΔT) at $t = 80$ s is shown below for illustrative purpose. Each curve represents the Stokes *V* at a particular instance. They are shifted in the vertical direction to show the evolution of the profiles with time. These profiles do not show significant variation with time revealing no sign of wave propagation inside the box. This is different in the case when the horizontal integration is carried out over only a narrow spatial window on the two sides of the flux tube axis. The left top panel (and similarly the right panel) shows the Stokes *V* profile averaged over a small slice (200 km) covering a horizontal distance from $x = 410$ km to $x = 610$ km ($x = 670$ km to $x = 870$ km for the right slice). Looking at profiles averaged over a narrow bundle of line-of-sights on either side of the axis, we clearly see left and right asymmetry, showing signatures of wave propagation.

The above illustration shows that it is necessary to observe with high spatial resolution in order to successfully study the effect of wave propagation in spectral lines of polarized light. An averaged profile covering both halves of flux tube is less likely to show any signature of wave propagation. This is due to the fact that the antisymmetric flow patterns on both sides of the flux tube will average out to give zero net contribution. Line-of-sights that cover only one half of the symmetric axis or a small part of it gives more information about the wave activity in the domain. In order to quantitatively study the signatures of wave propagation we look at the evolution of area and amplitude asymmetries according to the Eq. (5.5 - 5.6).

Figures 5.4 & 5.5 shows the snapshots of Stokes *V* profiles of Fe I λ 5250.2, 5247.06, 6301.5 & 6302.5 Å, at $t = 40$ s after the start of the simulation. Figure 5.4 shows the Stokes *V* profiles averaged over a horizontal distance from $x = 410$ km to $x = 610$ km

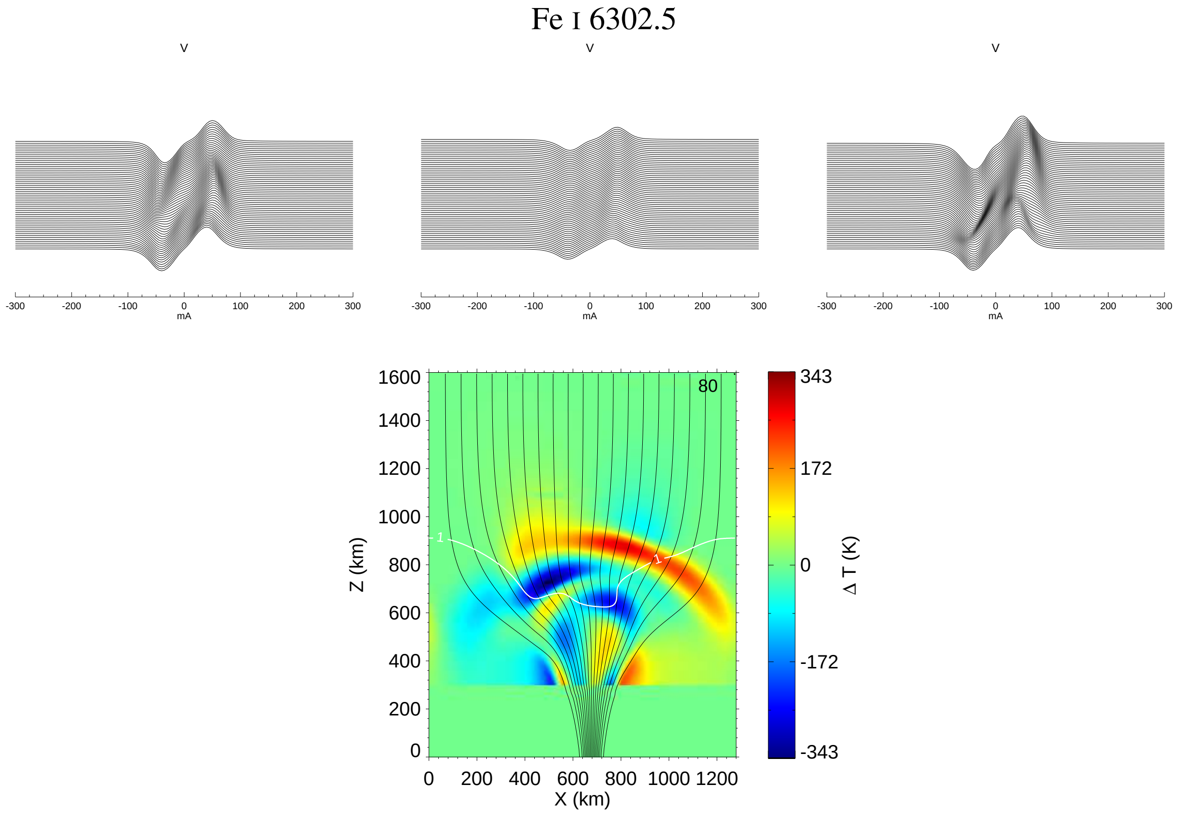

Figure 5.3: The temperature perturbation at 80 s for the case with field strength of 1000 G at $z = 0$ on the axis. The top three panel shows the evolution of the Stokes V profiles emerging from a small strip on the left side of the axis (top left panel), from the entire top boundary (middle) and the from a small strip on the right side of the axis (right).

and the Figure 5.5 shows the profiles averaged over $x = 670$ km to $x = 870$ km. The lines Fe I λ 5250.2Å and Fe I λ 5247.06Å belong to the same multiplet of iron, and have the same line strength, excitation potential and wavelength but the effective Landé g-factor are 3 and 2 respectively. Hence the Stokes V amplitudes are different for the two lines and scale approximately according to the ratio given by the Landé g-factor as 3:2. This can be seen in the plots shown in Fig. 5.4, where the amplitudes of the Fe I λ 5247.06Å is lower than Fe I λ 5250.2Å. Similarly the amplitudes of Fe I λ 6301.5Å and Fe I λ 6302.5 Å scale according to the Landé g-factor of 1.67 and 2.5, respectively. The amplitude ratios are not strictly according to the Landé g-factor ratios in strong-field regime. (for details, see Stenflo 1994).

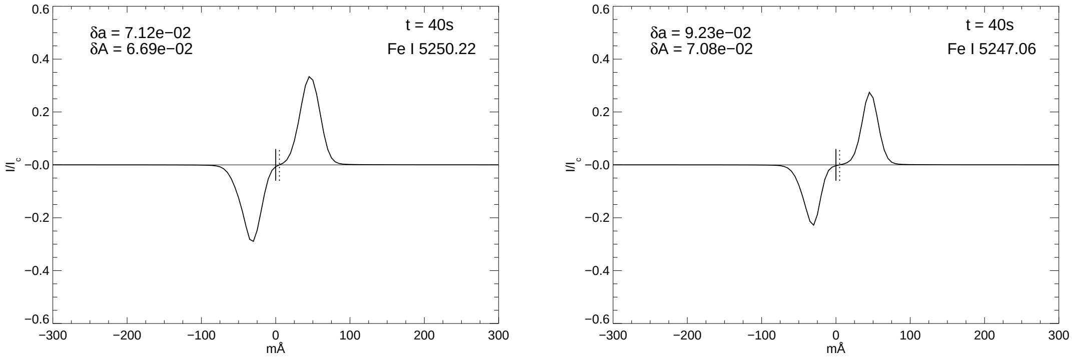

a) Fe I λ 5250.2Å b) Fe I λ 5247.06Å

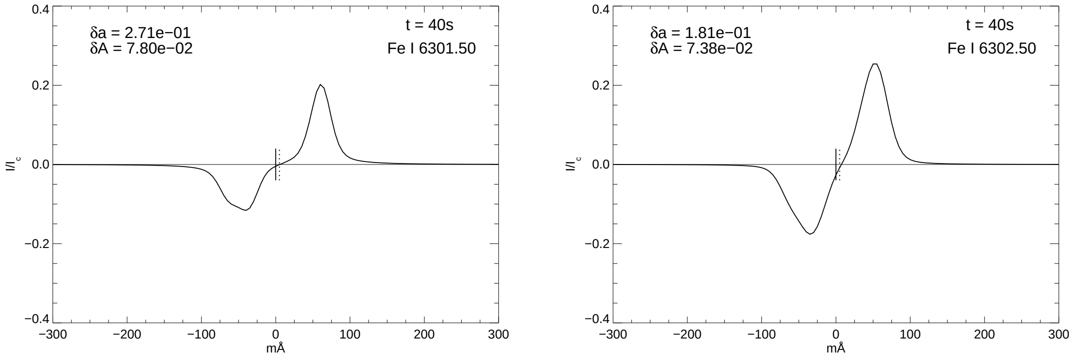

c) Fe I λ 6301.5Å d) Fe I λ 6302.5 Å

Figure 5.4: Stokes *V* profiles of Fe I a) λ 5250.2Å, b) λ 5247.06Å, c) λ 6301.5Å and d) λ 6302.5 Å at an elapsed time of 40 s in a vertical slice from $x = 410$ km to $x = 610$ km (left of the axis) for a configuration with a field strength of 1000 G on the axis at $z = 0$

Movie 5.19: Evolution of Stokes *V* profiles of Fe I λ 5250.2, 5247.06, 6301.5 & 6302.5 Å from a LOS situated on the left side of a flux sheet with moderate field strength after the initiation of a horizontal impulsive excitation in the bottom layer .

Movie 5.20: Evolution of Stokes *V* profiles of Fe I λ 5250.2, 5247.06, 6301.5 & 6302.5 Å from a LOS situated on the right side of a flux sheet with moderate field strength after the initiation of a horizontal impulsive excitation in the bottom layer .

Movie 5.21: Temperature perturbations with velocity vectors for a flux sheet with moderate field strength after the initiation of a horizontal impulsive excitation in the bottom layer .

The height of formation of the spectral lines depends on the line strength, which in turn depends on the excitation potential and the log (*gf*). The region of formation spans a wide range and is affected by the presence of the magnetic field. In a strong magnetic field the formation regions for the four Fe lines typically peaks at the following heights (e.g. Khomenko & Collados 2007): *a*) Fe I 6301.5 Å: ~ 250 – 300 km; *b*) Fe I 6302.5 Å: ~ 100 – 200 km; *c*) Fe I 5247.1 Å: ~ 250 – 350 kmand *d*) Fe I 5250.2 Å: ~ 280 – 370 km.

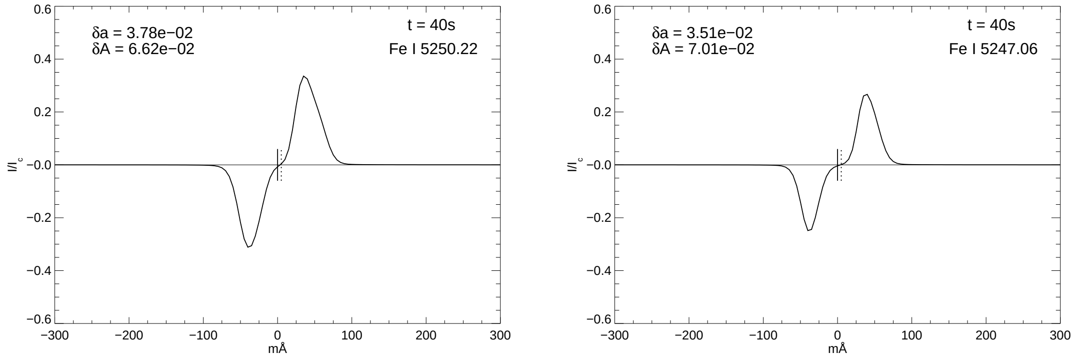

a) Fe I λ 5250.2Å

b) Fe I λ 5247.06Å

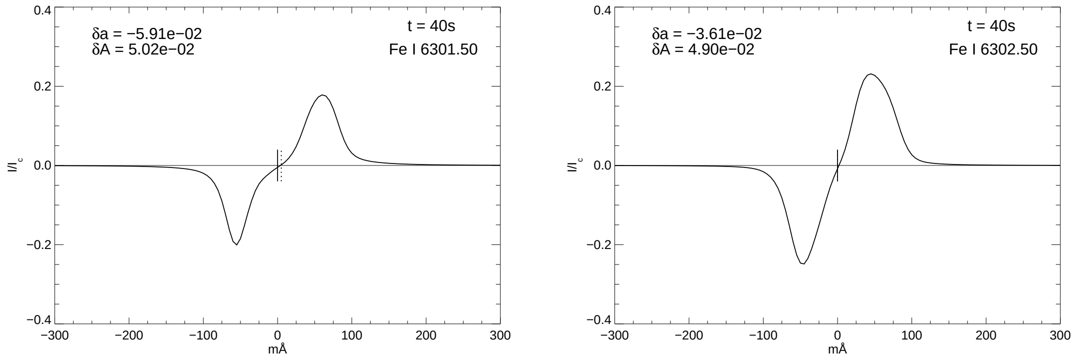

c) Fe I λ 6301.5Å

d) Fe I λ 6302.5 Å

Figure 5.5: Stokes V profiles of Fe I a) λ 5250.2Å, b) λ 5247.06Å, c) λ 6301.5Å and d) λ 6302.5 Å at a elapsed time of 40 s in a vertical slice from x = 670 km to x = 870 km (right of the axis) for a configuration with a field strength of 1000 G on the axis at $z = 0$

It should be noted that Fe I 6302.5 has two peaks, one of which forms lower in the atmosphere.

The asymmetry in the Stokes V profiles after 40 s can be clearly seen in the Fe I 6301.5 & 6302.5 Å lines plotted in Fig. 5.4 & 5.5. The effect of the wave propagation is first felt by these lines as they are formed lower in the atmosphere than the other two lines. The Stokes V asymmetries as a function of time for the above four lines give a more clear picture. Figure 5.6 shows the Stokes V a) amplitude asymmetry and b) area asymmetry for the 4 Fe I lines as a function of time. The red and blue colours represents a narrow line-of-sight on the two sides of the flux tube axis. The blue solid curve is for a line-of-sight spanning x = 410 km to x = 610 km (left) and the blue dashed curve is for x = 120 km to x = 320 km. Similarly, on the right side, the red solid curve is for x = 670 km to x = 870 km (right) and the red dashed curve is for x = 960 km to x = 1160 km. In order to explain Fig. 5.6 it is important to show the temperature perturbation and the velocity field of the simulation which is shown in Fig. 5.7. The colours represent the value of ΔT

and the arrows show the velocity vectors at time 20, 30, 40 and 50 s.

Initially, there are no velocities inside the domain and hence the Stokes profiles are symmetric and therefore δA and δa are zero. After the start of the simulation, velocities start building up in the domain, consequently, giving rise to symmetries in the Stokes profiles. Let us now consider the strip on the right side of the axis. After 20 s, we see that there is a small updraft within the line-of-sight in the magnetic region. This leads to a blue shift of the Zeeman split line that forms in this region like Fe I 6301.5 and 6302.5 Å lines. The unsplit line emerging from the layer below together with the blue shifted Zeeman component gives a Stokes V profile with a suppressed red lobe, consequently the amplitude asymmetry tends to become more positive. The amplitude asymmetry slowly starts rising and reaches a peak at around 50 s, after which a strong downdraft in the lower layers starts dominating making the red lobe strong again and the amplitude asymmetry to drop. On the other hand, the line-of-sight on the left side of the axis shows a inverse profile. After 20 s into the simulation, there is a strong downdraft within the LOS, and the Zeeman split lines are red shifted, suppressing the blue lobe and thereby the amplitude asymmetry starts dropping towards negative values. This trend is seen until slightly after 40 s when the updraft due to a vortical motion occurs in these regions. In the case of lines formed higher in the atmosphere, like Fe I 5250.2Å & 5247.06Å, we see that the profiles are phase shifted, depending on the arrival time of the perturbations due to the wave propagation in these regions. We see a delay of 10 s between the two pairs of lines corresponding to roughly a distance of 60 km, since the sound speed at these height is around 6 km s^{-1}.

The gradients in velocity and the magnetic field are the main cause for the asymmetry. A thumb-rule to calculate the sign of the area asymmetry, δA for a purely longitudinal component has been provided by Solanki & Pahlke (1988) (see also Steiner 1999)

$$\frac{d|B(\tau)|}{d\tau} \cdot \frac{d\mathrm{v}(\tau)}{d\tau} = \begin{cases} < \;\; 0 & \Rightarrow \delta A > 0 \\ > \;\; 0 & \Rightarrow \delta A < 0 \end{cases} \tag{5.7}$$

By convention, $\mathrm{v}(\tau)$ is taken to be positive for flows in direction of increasing optical depth and *vice versa*, where v is the line-of-sight velocity. In case of a expanding flux tube with height, a LOS within the tube will have $dB(\tau)|/d\tau > 0$. But, if the line of sight traverses an interface region, where, with increasing optical depth the field drops suddenly, we get $dB(\tau)|/d\tau < 0$. This is the case with LOSs far away from the flux sheet axis. Here, a positive δA is realized if $dv(\tau)/d\tau > 0$, which means if there is a accelerated downflow, for instance, when there is no velocity inside the flux-sheet but a downflow in the field-free region, or, an upflow within the flux sheet and no flow in the outside field-free region.

We now consider LOSs far away from the flux tube axis. These are depicted as blue dashed vertical lines in Fig. 5.7. The perturbations become more stronger in this region after 50 s just as the first front arrives. On the right side of the tube, we see that the velocities are directed upward. This suppresses the blue lobe making the amplitude asymmetry more positive. Whereas, in the case of left side of the flux tube, the downward velocities shifts the amplitude asymmetry towards less positive values. The phase shift between the two profiles of the amplitude asymmetry for the two LOS in the left side of the tube axis gives a value of ∼25 s, corresponding to a distance of ∼150 km. The centres of these LOSs are separated by 190 km.

i) Fe I λ 5247.06 Å

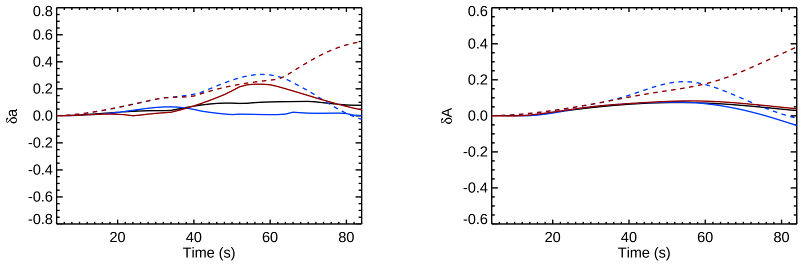

ii) Fe I λ 5250.2 Å

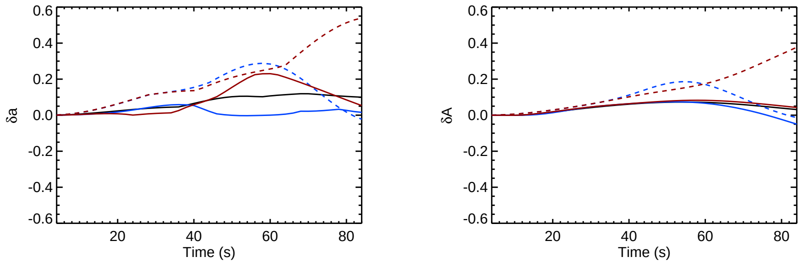

iii) Fe I λ 6301.5 Å

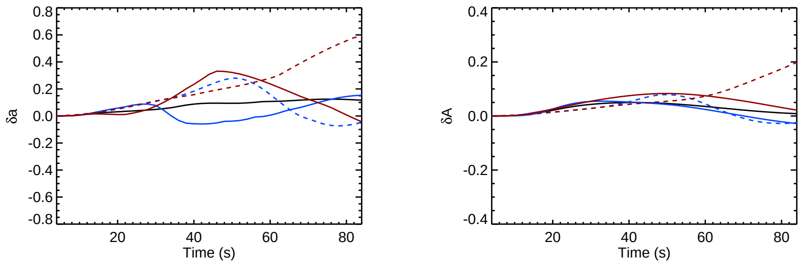

iv) Fe I λ 6302.5 Å

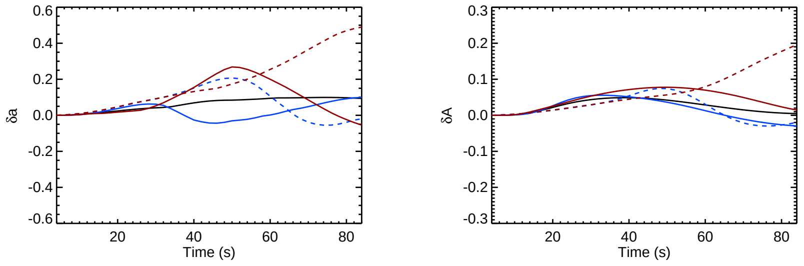

a) Amplitude Asymmetry b) Area Asymmetry

Figure 5.6: The Stokes *V* a) amplitude asymmetry and b) area asymmetry for the four Fe I lines as a function of time for the moderate field case with 1000 G. The red solid curve represents the slice on the right side of the the axis. The red dashed curve represents the slice on the far right. Blue solid curve is for the left slice and blue dashed curve is for the far left slice.

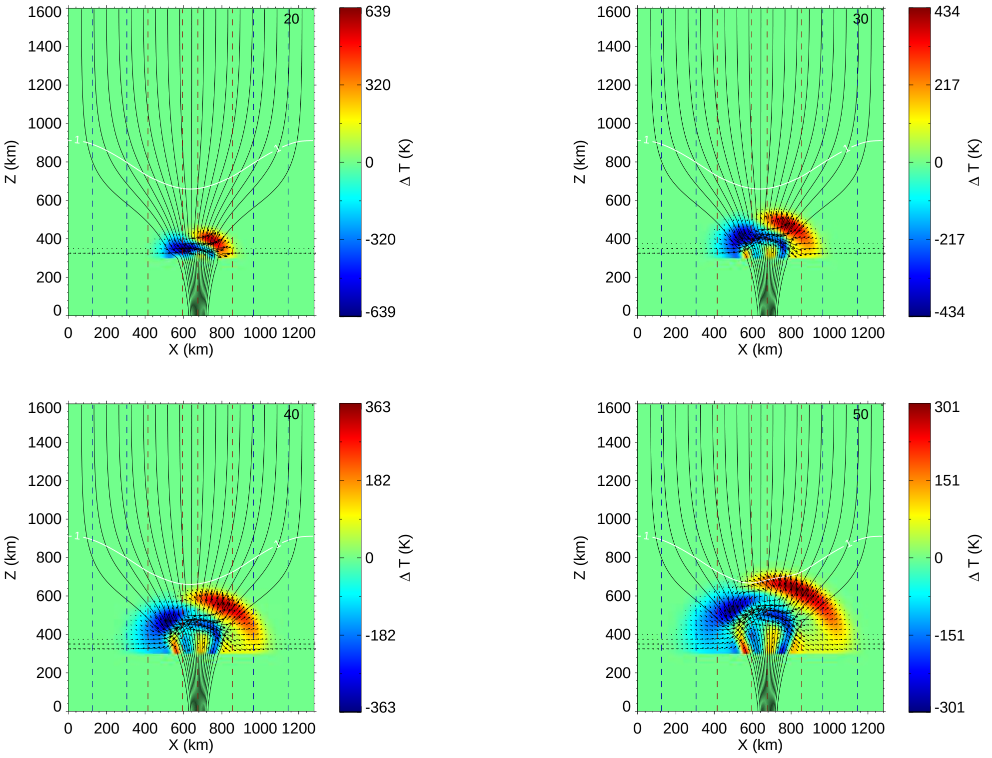

Figure 5.7: Temperature perturbations and velocity field of a flux tube in which the field strength at the axis at $z = 0$ is 1000 G at time 20, 30, 40 and 50 s after initiation of an impulsive horizontal motion of the entire region below $z = 300$ km with an amplitude of 5 km s^{-1} and a period of $P = 24$ s.

5.2.2 STRONG FIELD CASE

The emergent Stokes V profiles were computed for a flux tube with a magnetic field strength of 1600 G on the axis at $z = 0$ km. The Stokes V profiles emerging from the top boundary were spatially averaged spanning the whole width of the box. Similar to the case with a field strength of 1000 G, these profiles also do not show significant variation with time revealing no sign of wave propagation inside the box. The averaged profiles over smaller slices on either side of the axis show signs of wave propagation. An illustration similar to Fig. 5.3 is shown in Fig. 5.8.

We have already seen that when we average over only one half of the flux sheet or a small part of it, we get a clearer wave signature. Here we carry out a similar study of the evolution of the Stokes V asymmetries for the 1600 G case as was done for the 1000 G case. Figures 5.9 & 5.10 show the snapshots of Stokes V profiles of the four set of Fe I lines under study at $t = 40$ s. Figure 5.9 shows the Stokes V profiles averaged over a

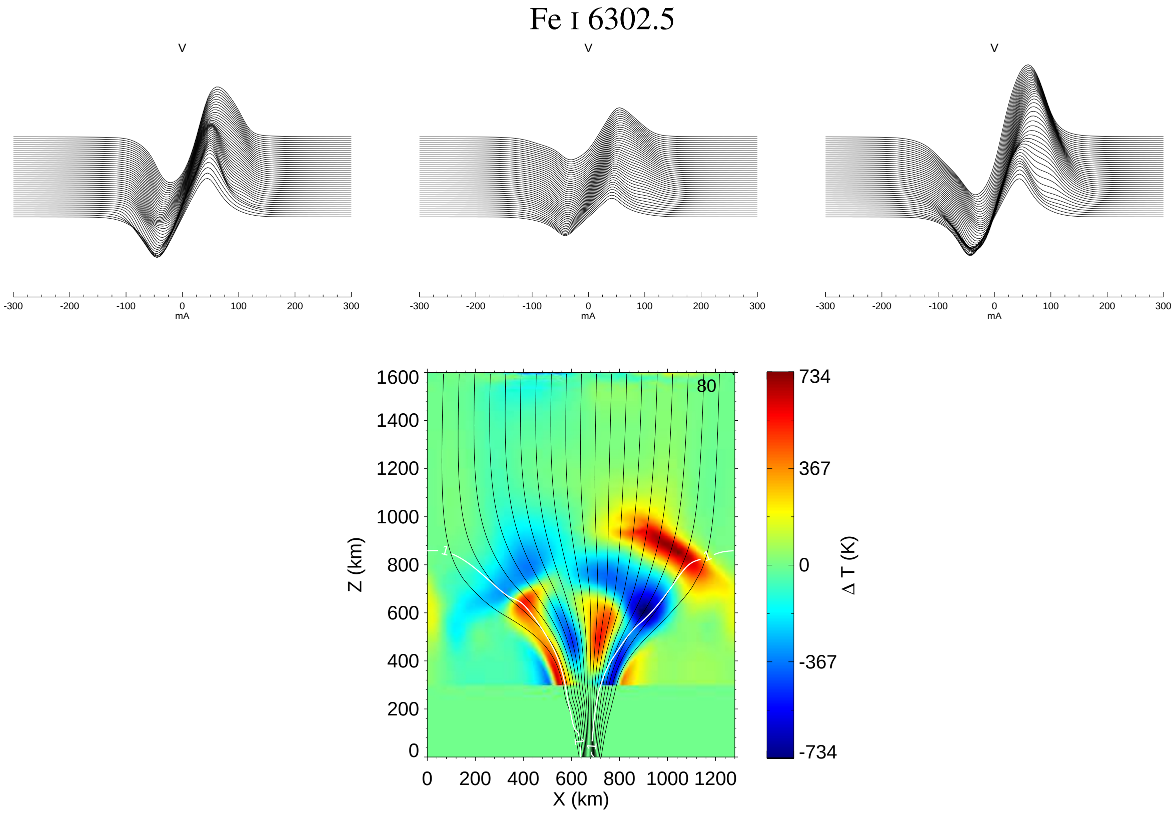

Figure 5.8: The temperature perturbation at 80 s for the case with a field strength of 1600 G at $z = 0$ on the axis. The top panel shows the evolution of the Stokes V profiles emerging from a small strip on the left side of the axis (top left panel), the complete top boundary (middle) and the right side of the axis (right).

horizontal distance from $x = 410$ km to $x = 610$ km and the Fig. 5.10 shows the profiles averaged over $x = 670$ km to $x = 870$ km. Comparing it with Fig. 5.4 & 5.5, we see that the Stokes V profiles are stronger in this case due to a stronger magnetic field.

The Stokes V amplitude asymmetry and area asymmetry as a function of time for these lines are shown in Fig. 5.11. The colour coding is the same as in Fig. 5.6. The temperature perturbation and the velocity field for different time instances is shown in Fig. 5.12. The colours represent the value of ΔT and the arrows show the velocity vectors at times 20, 30, 40 and 50 s.

A very strong velocity at the interface between the flux sheet and the ambient medium can be seen in Fig. 5.12, which is an artefact that cannot be attributed to any wave propagation. Due to this, the interpretation of the shifts in asymmetry is unreliable for the LOSs which are close to the axis of the flux tube. Henceforth, we will concentrate on the LOSs that span $x = 120$ km to $x = 320$ km (far left) and $x = 960$ km to $x = 1160$ km (far right) shown as blue dashed vertical lines in Fig. 5.12. Unlike, the case with 1000 G, here we have a *mode conversion* taking place when the fast magnetic mode gets refracted and enters in the field free domain thereby converting into a fast acoustic wave. This can be clearly seen in the temperature perturbations in the wing-like feature that extends from $z = 600$ km to $z = 1000$ km on both sides of the flux sheet at $t = 40$ s. The velocities associated with the wave results in the shift and the asymmetries of the Stokes V profiles.

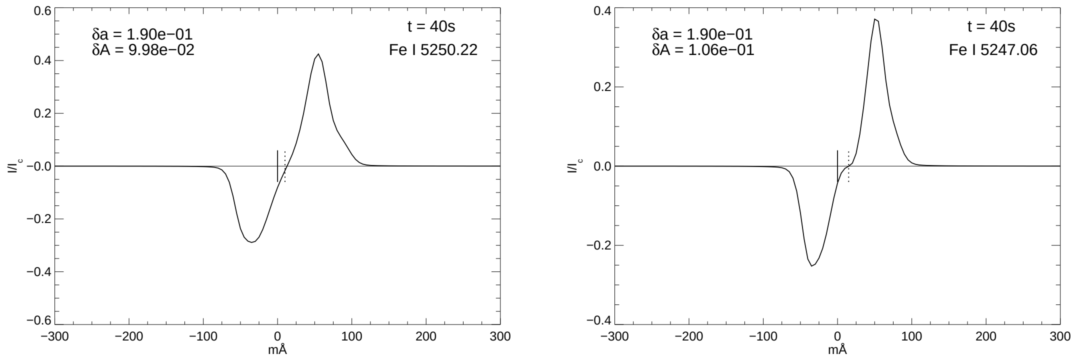

a) Fe I λ 5250.2Å b) Fe I λ 5247.06Å

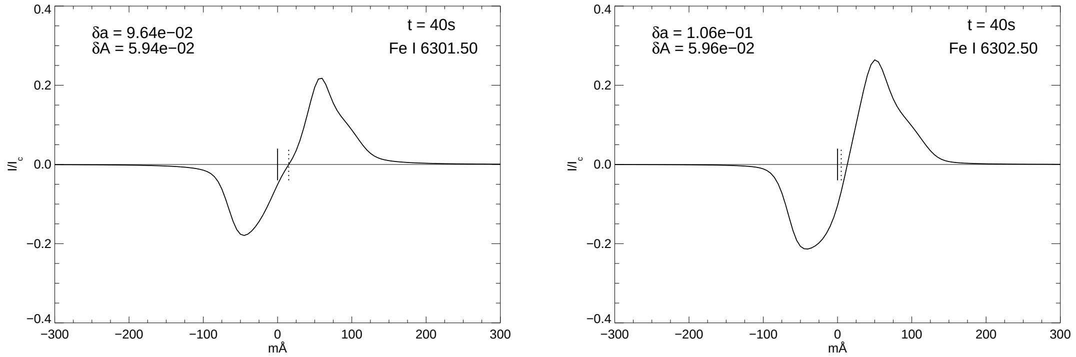

c) Fe I λ 6301.5Å d) Fe I λ 6302.5 Å

Figure 5.9: Stokes V profiles of Fe I a) λ 5250.2Å, b) λ 5247.06Å, c) λ 6301.5Å and d) λ 6302.5 Å at a elapsed time of 40 s in a vertical slice from $x = 410$ km to $x = 610$ km (left of the axis) for a configuration with a field strength of 1600 G on the axis at $z = 0$

In the following we consider a bundle of lines of sight on the far left side of the flux tube axis. Here, the rarefaction front of the *mode converting* wave arrives at a $t = 40$ s. The velocities are directed upwards in the magnetic region resulting in a blue shifted Zeeman splitted line, giving rise to a suppressed red lobe leading to a positive asymmetry (Fig. 5.11.). At $t = 60$ s, this upflow is pushed out into the field-free region while within the magnetic region a downflow evolves. These two flows give rise to a negative asymmetry leading to a strong negative bump of the blue dashed curve around $t = 60$ s. This feature is different from the 1000 G case shown in Fig. 5.6 wherein the velocities are mainly downward directed but in the non-magnetic region. The LOS on the right hand side of the flux tube axis is more interesting as we see here a dip in the profile of the amplitude asymmetry unlike that in Fig. 5.6. This can be explained as follows: At $t = 30$ s the mode converting wave enters into the LOS. The velocities are downward directed within the magnetic region, giving red shifted Zeeman components. Thus, the blue lobe is slightly suppressed and the asymmetry is shifted towards being less positive. This trend changes as soon as the fast magnetic wave gets converted into a fast acoustic wave by entering the non magnetic region. Here the downward velocities result in a red shifted spectral line giving rise to a shortening of the red lobe leading to a strong positive asymmetry. This trend is taken up by the slow wave which enters the LOS in the magnetic region at ~50 s, with the velocities mainly directed upwards.

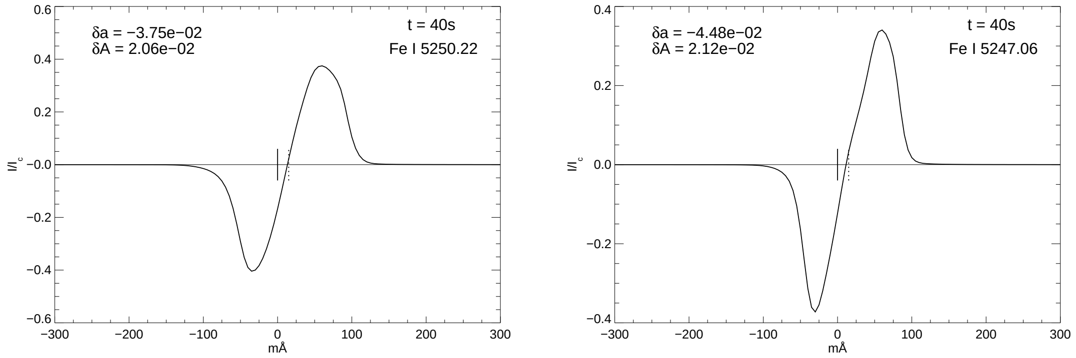

a) Fe I λ 5250.2Å

b) Fe I λ 5247.06Å

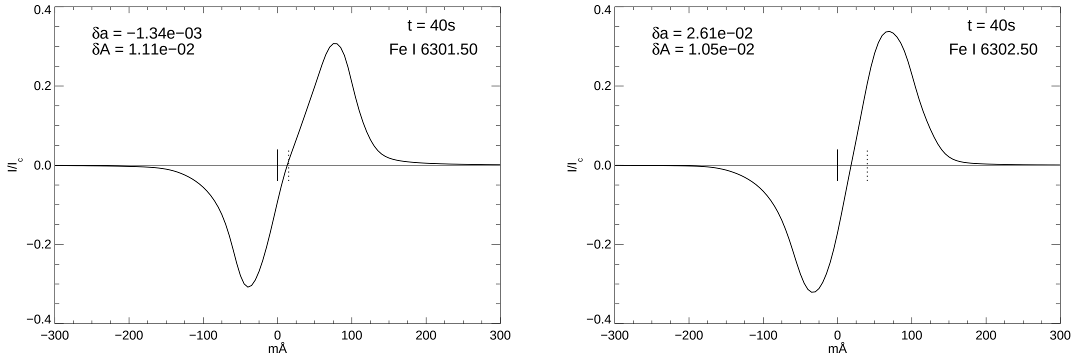

c) Fe I λ 6301.5Å

d) Fe I λ 6302.5 Å

Figure 5.10: Stokes *V* profiles of Fe I a) λ 5250.2Å, b) λ 5247.06Å, c) λ 6301.5Å and d) λ 6302.5 Å at a elapsed time of 40 s in a vertical slice from $x = 670$ km to $x = 870$ km (right of the axis) for a configuration with a field strength of 1600 G on the axis at $z = 0$

Movie 5.22: Evolution of Stokes V profiles of Fe I λ 5250.2, 5247.06, 6301.5 & 6302.5 Å from a LOS situated on the left side of a flux sheet with strong field strength after the initiation of a horizontal impulsive excitation in the bottom layer .

Movie 5.23: Evolution of Stokes V profiles of Fe I λ 5250.2, 5247.06, 6301.5 & 6302.5 Å from a LOS situated on the right side of a flux sheet with strong field strength after the initiation of a horizontal impulsive excitation in the bottom layer .

Movie 5.24: Temperature perturbations with velocity vectors for a flux sheet with strong field strength after the initiation of a horizontal impulsive excitation in the bottom layer .

5.3 CONCLUSION

Previous chapters focussed on the dynamics and the energy transport that occur in intense flux tubes. We used the results of our simulation to compute the Stokes profiles that emerge from the top of our simulation box in order to find signatures of wave propagation inside the tubes. We see that, while the average profile over the whole domain does not show any significant variation with time, a clear evidence of wave phenomena can be seen when we look at more resolved line-of-sights on either sides of the flux tube. Depending on the direction of excitation, Stokes-V profiles become asymmetric with opposite behaviour on opposite sides of the flux-sheet axis. Furthermore, effects of refraction of waves in the case of stronger fields are clearly visible in the Stokes analysis. Our results show signatures of mode conversion from fast (magnetic) to fast (acoustic) wave in these profiles. We come to the conclusion that signatures of wave propagation in magnetic elements can be observed with spatial resolutions when the magnetic concentrations are clearly resolved and observations in different regions within the flux concentrations is possible. Observations with higher resolution will not only resolve individual flux tubes/sheets but looking at various lines of sight around the flux concentration will also reveal effects like mode coupling. This chapter has highlighted the importance of using the Stokes V asymmetries as a possible diagnostic tool to study wave propagation in magnetic structures. The analysis in this chapter is based on the photospheric lines which are formed in local thermodynamic equilibrium (LTE). Hence our conclusions are not valid for line formed in the chromosphere, since LTE approximation is no longer valid in this region. A more realistic modelling should be done in 3-D and include NLTE effects.

i) Fe I λ 5247.06 Å

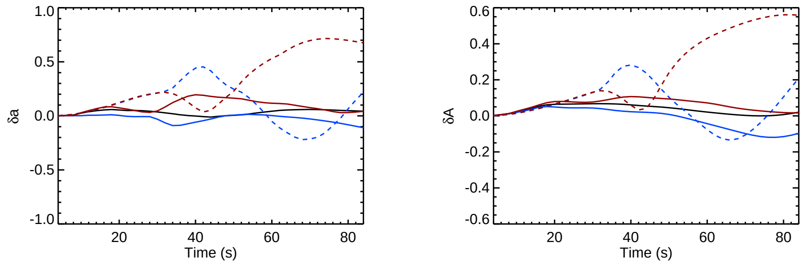

ii) Fe I λ 5250.2 Å

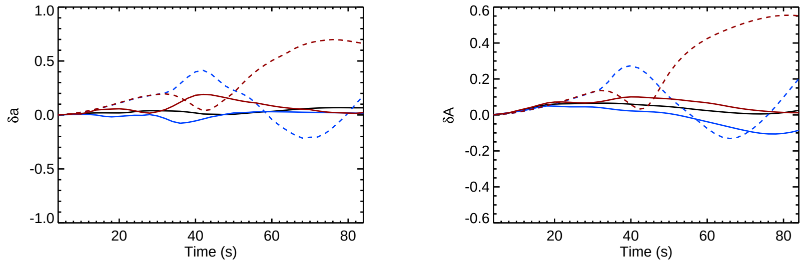

iii) Fe I λ 6301.5 Å

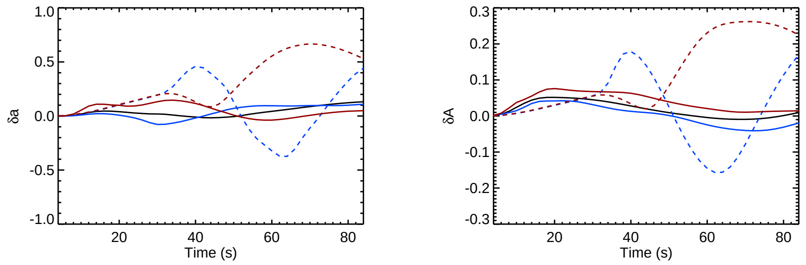

iv) Fe I λ 6302.5 Å

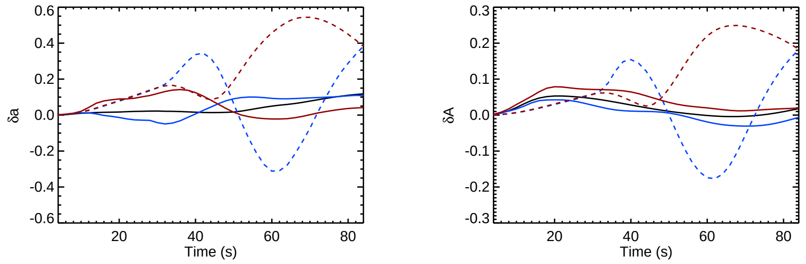

a) Amplitude Asymmetry b) Area Asymmetry

Figure 5.11: The Stokes V a) amplitude asymmetry and b) area asymmetry for the 4 Fe I lines as a function of time for the strong field case with 1600 G. The red solid curve represents the slice on the right side of the the axis. The red dashed curve represents the slice on the far right. Blue solid curve is for the left slice and blue dashed curve is for the far left slice.

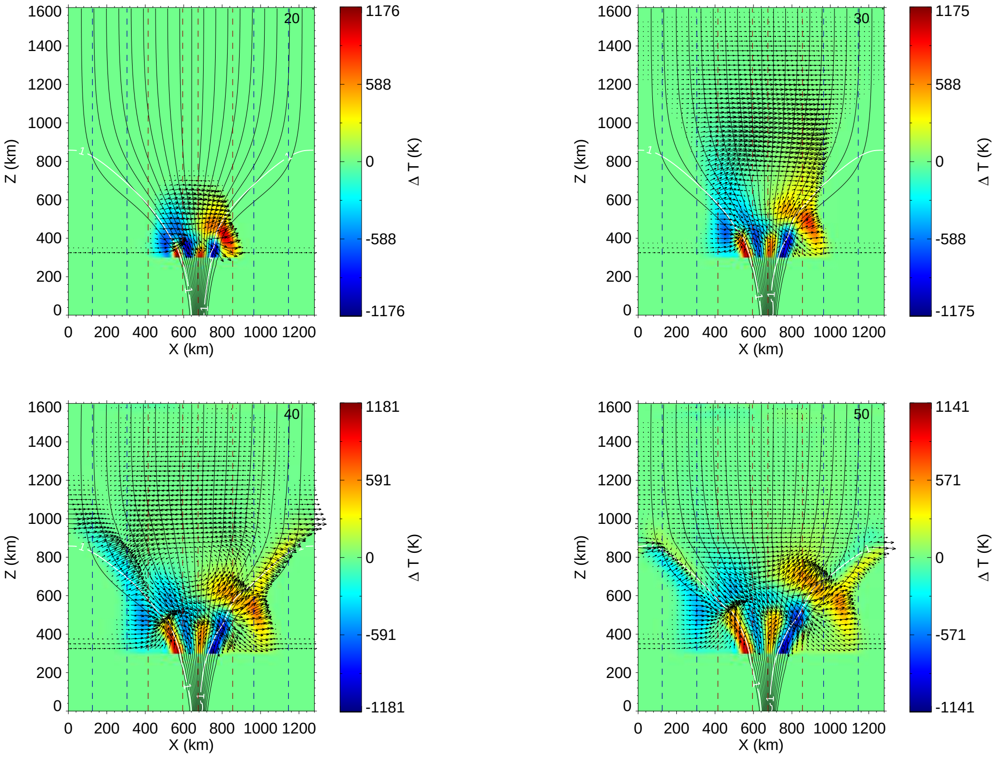

Figure 5.12: Temperature perturbations and velocity field in a flux tube in which the field strength at the axis at $z = 0$ is 1600 G at time 20, 30, 40 and 50 s after initiation of an impulsive horizontal motion of the entire region below $z = 300$ km with an amplitude of 5 km s^{-1} and a period of $P = 24$ s.

CHAPTER 6

CONCLUSION AND OUTLOOK

A study of the fundamental processes in the solar atmosphere associated with magnetic fields is vital in understanding their role in the heating of the chromosphere and corona. This thesis focusses on the propagation of waves, the accompanying transport of energy, and its observable signatures in magnetic flux concentrations in the solar atmosphere. A major thrust of this investigation is to shed light on the heating of the chromospheric network, one of the important unresolved issues in solar physics. The coupling of various wave modes in and around flux tubes and the identification of the regions where they occur is a topic that is of general interest not only to solar physicists, but also to the wider astrophysical community.

This thesis has significantly extended the works of Hasan et al. (2005) and Hasan & van Ballegooijen (2008) who showed that the displacements of magnetic flux tubes embedded in the photosphere generate transverse and longitudinal waves within the field concentrations and acoustic waves in the ambient medium. The latter are possible sources for the heating of network elements. The present work builds on the previous calculations to consider the effects of wave excitation in flux sheet with varying field strengths. We also estimate the energy carried by the waves and furthermore examine the effect on the acoustic emission by varying the thickness of the tube-ambient medium interface.

We have found that the nature of the modes excited depends upon the value of β (ratio of gas to magnetic pressure) in the region where the driving motion occurs or the extent of the region of excitation. When β is large (corresponding to a weak field), a slow wave which is a transverse magnetic mode that propagates along the field lines, is excited undergoing mode transmission as it crosses the $\beta = 1$ layer. In this case, the wave only changes label from slow to fast, but remains magnetic in character throughout the flux sheet. In addition a fast mode is excited, which propagates almost isotropically, undergoes both mode conversion and transmission at the $\beta = 1$ surface depending on the "attack angle", the angle between the wave vector and the magnetic field. On the other hand, in the case of a strong magnetic field (low-β case), where the level of $\beta = 1$ is below the driving region, the fast (magnetic) and slow (acoustic) modes propagate through the flux sheet atmosphere without changing character.

We find that the magnetically dominated fast wave within the low-β region of the flux sheet undergoes strong refraction so that it finally leaves the flux sheet in the lateral direction, where it gets partially and mainly converted to a fast, acoustically dominated wave. This effect is particularly visible in the case of a flux sheet with strong magnetic field.

We also see an asymmetry in the wave structure on both sides of the flux sheet axis. This comes because the leading front of the predominantly acoustic mode is compressional on the one hand side and expansive on the other side and vice versa for the following phase. Since the compressive phase travels faster as the sound speed is larger, the two phases move either apart from each other or converge. This asymmetry gives rise to observable signatures and has been confirmed by analysing the Stokes V spectra that emerge from highly resolved line-of-sights. The energy

IMPACT OF THE THESIS

This thesis provides further insight of the structure, dynamics and energy transport in small scale magnetic elements which are considered to be the building blocks of solar magnetism. It highlights the influence of the region of excitation in the generation of various MHD wave modes and also the importance of the wave mode conversion zone. We have for the first time given a quantitative estimate of the energy fluxes carried by the various wave modes and have shown that the acoustic waves generated by transverse motions of the footpoints of magnetic network elements cannot balance the chromospheric energy requirements of network regions. We have also predicted possible observational signatures of wave activity in magnetic elements.

LIMITATIONS AND FUTURE PROSPECTS

The numerical simulations described in this thesis are limited by the fact that they use simple idealistic pulses for the wave excitation. Various limitations of this simulation, like unavailability of a more realistic source of waves, can be overcome in a "realistic simulation". In a realistic simulation, the velocity fields that are already present in the non stationary atmosphere can interact with the flux concentration and excite waves. We have only considered single, short duration, transverse pulses for the wave excitation. A more realistic driver with sustained pulses of varying lengths, velocities, and time intervals would give rise to highly non-linear dynamics, which might yield increased acoustic fluxes. Also we have not considered longitudinal wave excitation, which would be available primarily from global p-mode oscillations. Ohmic dissipation is another source of energy that was not considered here which may come from direct dissipation of magnetic fields. Another point this thesis does not take into consideration is the photospheric radiative losses, which would damp the waves before they reach chromospheric heights. Furthermore, we have considered only two spatial dimensions. Introducing one more dimension would result in an additional intermediate wave (the Alfvén wave) and therefore one would have transmission and conversion between three types of waves. The details of the mode coupling and the partition of energy fluxes to the various modes would become more complex. The broad conclusion of the thesis cannot be expected to drastically change when turning to three spatial dimensions. However, the details of the mode coupling and the partition of energy fluxes to the various modes would become more complex but the share of energy that resides in the acoustic mode cannot be much larger than in the two-dimensional case. On the contrary, the energy flux generated at the footpoint of the magnetic element would have to be distributed to a larger area in three spatial dimension so that the spatial mean at reaching upper layers would be lower.

A new era of discovery is anticipated with the advent of forthcoming ground telescopes like the National Large Solar Telescope (NLST) and Advanced Technology Solar Telescope (ATST) and space telescopes like Solar Dynamics Observatory (SDO). Unprecedented simultaneous multi-spectral imaging with high temporal cadence capability of the NLST and ATST will result in a better understanding of the structure and dynamics of the magnetized solar atmosphere. The highly ambitious goal of SDO to pin-point the source of solar irradiance variability to the underlying magnetic features will try to solve the mystery of the heating of the upper atmosphere. These missions will provide a platform to test the results of this thesis and for further research in this growing field.

APPENDIX A

NUMERICAL SOLUTION OF THE LAPLACE'S EQUATION

The general Laplace equation in 2-D Cartesian coordinates is given as,

$$\frac{\partial^2 \psi}{\partial x^2} + \frac{\partial^2 \psi}{\partial y^2} = 0. \tag{A.1}$$

Using the finite difference representation with central difference form, the derivatives can be written as,

$$\frac{\partial^2 \psi}{\partial x^2} = \frac{\psi_{i+1,j} - 2\psi_{i,j} + \psi_{i-1,j}}{(\Delta x)^2}, \tag{A.2}$$

$$\frac{\partial^2 \psi}{\partial y^2} = \frac{\psi_{i,j+1} - 2\psi_{i,j} + \psi_{i,j-1}}{(\Delta y)^2}, \tag{A.3}$$

The numerical form of the Laplace equation then becomes,

$$\frac{\psi_{i+1,j} - 2\psi_{i,j} + \psi_{i-1,j}}{(\Delta x)^2} + \frac{\psi_{i,j+1} - 2\psi_{i,j} + \psi_{i,j-1}}{(\Delta y)^2} = 0. \tag{A.4}$$

The above equation is discretized on a rectangular grid and solved with appropriate boundary conditions using numerical procedures like Thomas' algorithm which is used to solve a tridiagonal system of equations.

NUMERICAL SOLUTION OF THE GRAD-SHAFRANOV EQUATION

The construction of a magnetostatic flux tube proceeds by considering the parallel and normal component of the magnetostatic force balance (Eq. (2.23)) along a field line.

Taking a scalar product of Eq. (2.23) with $\boldsymbol{B}$ we get,

$$\boldsymbol{B} \cdot (\nabla p - \rho \boldsymbol{g}) = 0. \tag{A.5}$$

If θ is the angle between the $\boldsymbol{B}$ and z with $\boldsymbol{g} = -g\hat{z}$ and s is the distance along the field line then, Eq. (A.5) can be written as,

$$\frac{\mathrm{d}p}{\mathrm{d}s} + \rho g \cos\theta = 0. \tag{A.6}$$

Using Eq. (2.11), it becomes,

$$\frac{\mathrm{d}p}{p} = -\frac{\mu g}{\mathcal{R}T} \cos\theta \, ds = 0. \tag{A.7}$$

Writing $\cos\theta \, ds = dz'$, and the pressure scale height $H = \mathcal{R}T/\mu g$, solution of the Eq. (A.8) along the surface of constant ψ is,

$$p(\psi, z) = p_0 e^{-\int_0^z \frac{1}{H(\psi, z')} dz'}. \tag{A.8}$$

By specifying the initial temperature in the whole computational domain, the pressure, p can be calculated using the above equation (Eq. (A.8)), and consequently the density ρ.

Taking a vector product of Eq. (2.23) with $\boldsymbol{B}$ we get,

$$\boldsymbol{B} \times (\boldsymbol{J} \times \boldsymbol{B}) = \boldsymbol{B} \times (\nabla p - \rho \boldsymbol{g}). \tag{A.9}$$

For an axisymmetric field it reduces to,

$$\boldsymbol{J} = \frac{\boldsymbol{B}}{B^2} \times (\nabla p - \rho \boldsymbol{g}). \tag{A.10}$$

Assuming a 2-D Cartesian coordinates, the magnetic field (using Eq. (2.27)) can be written as,

$$\boldsymbol{B} = -\frac{\partial \psi}{\partial z}\hat{\boldsymbol{i}} + \frac{\partial \psi}{\partial x}\hat{\boldsymbol{k}}. \tag{A.11}$$

Hence Eq. (A.10) becomes,

$$\boldsymbol{J} = \frac{1}{B^2}\left[-\frac{\partial \psi}{\partial z}\left(\frac{\partial p}{\partial z} + \rho g\right) - \frac{\partial \psi}{\partial x}\left(\frac{\partial p}{\partial x}\right)\right]\hat{\boldsymbol{j}}. \tag{A.12}$$

which can be further simplified using Eq. (A.8) and Eq. (A.11) to,

$$\boldsymbol{J} = -\left.\frac{\partial p}{\partial \psi}\right|_z \hat{\boldsymbol{j}}. \tag{A.13}$$

Eq. (2.24) thus reduces to,

$$\frac{\partial^2 \psi}{\partial x^2} + \frac{\partial^2 \psi}{\partial z^2} = \mu_m \left.\frac{\partial p}{\partial \psi}\right|_z . \tag{A.14}$$

This equation is called the Grad-Shafranov equation (Grad and Rubin 1958 ; Shafranov 1966). In the finite difference representation, Eq. (A.14) is written as,

$$\frac{\psi_{i+1,j} - 2\psi_{i,j} + \psi_{i-1,j}}{(\Delta x)^2} + \frac{\psi_{i,j+1} - 2\psi_{i,j} + \psi_{i,j-1}}{(\Delta y)^2} = \mu_m \frac{p_{i+1,j} - p_{i-1,j}}{\psi_{i+1,j} - \psi_{i-1,j}}. \tag{A.15}$$

This equation is discretized on a rectangular grid and solved using the libraries available in MUDPACK[*]. The iterative procedure for computing the magnetostatic equilibrium configuration proceeds as follows:

1. A magnetic configuration is initially specified. A thin flux tube is modelled by assuming that the temperature inside the flux tube and the ambient medium are equal. Then the internal and external pressures are related using the pressure balance condition given by Eq. (2.17). Specifying the internal pressure and the magnetic strength at the bottom boundary and the pressure scale height a flux tube embedded in a plane parallel atmosphere is constructed.

2. Using Eq (A.8), the gas pressure inside the entire domain is calculated

3. The current density is calculated from the pressure using Eq. (A.13)

4. The new magnetic field configuration with appropriate boundary condition is calculated from the current density using the Grad-Shafranov equation (Eq. (A.15)). With the new ψ, starting with 2 once again the gas pressure is computed starting a new iteration until the solution converges such that the difference between ψ_{new} and ψ_{old} is less than some specified value.

---

[*] `http://www.cisl.ucar.edu/css/software/mudpack/`

APPENDIX B

NUMERICAL SOLUTION OF THE MHD EQUATIONS

The MHD equations in conservation form for an inviscid adiabatic fluid can be written in general as,

$$\frac{\partial U}{\partial t} + \frac{\partial F}{\partial x} + \frac{\partial G}{\partial z} = S \tag{B.1}$$

where,

$$U = \begin{Bmatrix} \rho \\ \rho v v_x \\ \rho v_z \\ \rho s \\ B_x \\ B_z \end{Bmatrix}, \quad F = \begin{Bmatrix} \rho v_x \\ \rho v_x^2 + p + \frac{1}{2\mu}(B_z^2 - B_x^2) \\ \rho v_x v_z - \frac{1}{\mu} B_x B_z \\ v \rho s \\ 0 \\ v_x B_x - v_z B_x \end{Bmatrix},$$

$$G = \begin{Bmatrix} \rho v_z \\ \rho v_x v_x - \frac{1}{\mu} B_x B_z \\ \rho v_z^2 + p + \frac{1}{2\mu}(B_x^2 - B_z^2) \\ v_z \rho s \\ v_z B_x - v_x B_z \\ 0 \end{Bmatrix} \quad \text{and} \quad S = \begin{Bmatrix} 0 \\ 0 \\ -\rho g \\ 0 \\ 0 \\ 0 \end{Bmatrix}$$

The integration of Eq. (B.1) is carried out using a explicit finite difference method based on the Flux Corrected Transport (FCT) scheme (see Oran & Boris 1987). The equation is discretized on a equidistant grid and the values of $\rho, \rho v_x, \rho v_z, \rho$s are prescribed at the cell-center and the magnetic field components, B$_x$ and B$_z$ are prescribed at the cell-interfaces. The sketch of the grid is shown in Fig. B.1.

In the finite difference representation, Eq. (B.1) can be written as,

$$\frac{U_{i,j}^{n+1} - U_{i,j}^{n}}{\Delta t} = -\frac{F_{i+\frac{1}{2},j} - F_{i-\frac{1}{2},j}}{\Delta x} - \frac{G_{i,j+\frac{1}{2}} - G_{i,j-\frac{1}{2}}}{\Delta x} + S. \tag{B.2}$$

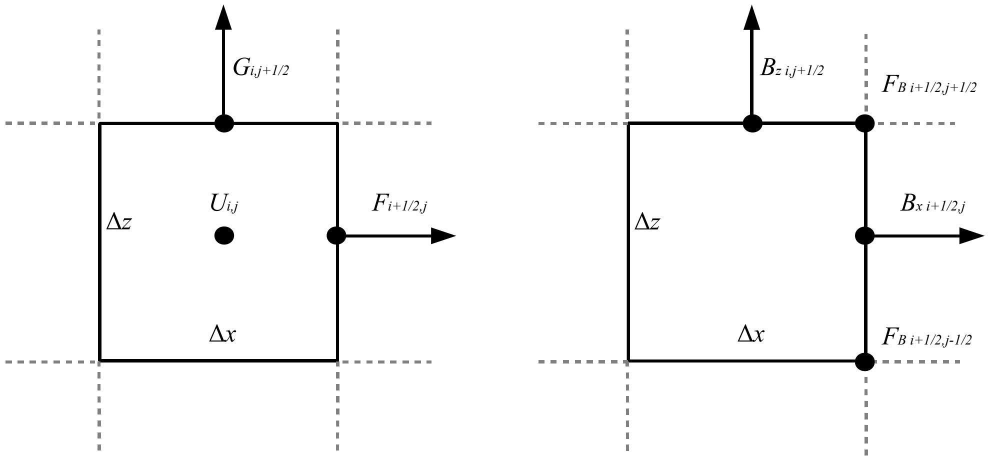

Figure B.1: Sketch of the computational grid

Each grid point in space and time is identified by the indices, i,j and n, where, i is the running index in the x direction, j is the running index in the z direction and n is the index in the time-marching direction, t.

Rearranging the Eq. (B.2), the time marching solution for U, in the *explicit* form can be written as,

$$U^{n+1}_{i,j} = U^{n}_{i,j} - \frac{\Delta t}{\Delta x}\left[F_{i+\frac{1}{2},j} - F_{i-\frac{1}{2},j}\right] - \frac{\Delta t}{\Delta z}\left[G_{i,j+\frac{1}{2}} - G_{i,j-\frac{1}{2}}\right] + S\,\Delta t. \tag{B.3}$$

Equation (B.3) gives the new solution of U at all grid points at time, $t = (n+1)\Delta t$ from the known values of U,F,G and S at time $t = n\Delta t$. In case of the induction equation (Eq. B.1), the solution for the field components can be written as,

$$B^{n+1}_{x\ i+\frac{1}{2},j} = B^{n}_{x\ i+\frac{1}{2},j} - \frac{\Delta t}{\Delta z}\left[G^{B}_{i+\frac{1}{2},j+\frac{1}{2}} - G^{B}_{i+\frac{1}{2},j-\frac{1}{2}}\right], \tag{B.4}$$

and

$$B^{n+1}_{z\ i,j+\frac{1}{2}} = B^{n}_{z\ i,j+\frac{1}{2}} - \frac{\Delta t}{\Delta z}\left[F^{B}_{i+\frac{1}{2},j+\frac{1}{2}} - F^{B}_{i-\frac{1}{2},j+\frac{1}{2}}\right]. \tag{B.5}$$

The numerical fluxes, F and G are computed using the Flux Corrected Transport scheme described below.

FLUX CORRECTED TRANSPORT SCHEME

Flux Corrected Transport (FCT) scheme is an explicit, Eulerian, second-order finite difference scheme for solving conservation equations developed by Boris (1971) (Boris & Book 1976; Boris 1976). FCT method handles steep gradients and shocks very well by adjusting the fluxes going in and out of the computational cells, such a way that, any non-physical maxima or minima introduced by the numerical algorithm is circumvented. The algorithm proceeds in two stages as follows:

TRANSPORT STAGE: The transportive fluxes at cell interfaces, $F^T_{i+1/2,j}$ and $G^T_{i,j+1/2}$ are calculated using the Eq. (B.1). A strong diffusive flux is added to the transportive flux

$$F^{TD}_{i+\frac{1}{2},j} = F^{T}_{i+\frac{1}{2},j} - \nu_{x\ i+\frac{1}{2},j}\left[U_{i+1,j} - U_{i-1,j}\right] \tag{B.6}$$

$$G^{TD}_{i,j+\frac{1}{2}} = G^{T}_{i,j+\frac{1}{2}} - \nu_{z\ i,j+\frac{1}{2}}\left[U_{i,j+1} - U_{i,j-1}\right] \tag{B.7}$$

with ν, the diffusion coefficient, defined as,

$$\nu_{x\ i+\frac{1}{2},j} = \frac{1}{6} + \frac{1}{3}\epsilon^2_{x\ i+\frac{1}{2},j} \quad \text{and} \quad \nu_{z\ i,j+\frac{1}{2}} = \frac{1}{6} + \frac{1}{3}\epsilon^2_{z\ i,j+\frac{1}{2}} \tag{B.8}$$

where ϵ is the Courant number defined as,

$$\epsilon_{x\ i+\frac{1}{2},j} = v_{x\ i+\frac{1}{2},j}\frac{\Delta t}{\Delta x} \quad \text{and} \quad \epsilon_{z\ i,j+\frac{1}{2}} = v_{z\ i,j+\frac{1}{2}}\frac{\Delta t}{\Delta z} \tag{B.9}$$

An intermediate solution is calculated using the diffusive fluxes, F^{TD} and G^{TD} as,

$$\tilde{U}^n_{i,j} = U^n_{i,j} - \frac{\Delta t}{\Delta x}\left[F^{TD}_{i+\frac{1}{2},j} - F^{TD}_{i-\frac{1}{2},j}\right] - \frac{\Delta t}{\Delta z}\left[G^{TD}_{i,j+\frac{1}{2}} - G^{TD}_{i,j-\frac{1}{2}}\right] + S\,\Delta t. \tag{B.10}$$

ANTIDIFFUSIVE STAGE: Defining an antidiffusive flux as,

$$F^{A}_{i+\frac{1}{2},j} = \eta_{x\ i+\frac{1}{2},j}\left[\tilde{U}_{i+1,j} - \tilde{U}_{i-1,j}\right] \tag{B.11}$$

$$G^{A}_{i,j-\frac{1}{2}} = \eta_{z\ i,j+\frac{1}{2}}\left[\tilde{U}_{i,j+1} - \tilde{U}_{i,j-1}\right] \tag{B.12}$$

where η, the antidiffusive coefficients are defined as,

$$\eta_{x\ i+\frac{1}{2},j} = \frac{1}{6} - \frac{1}{6}\epsilon^2_{x\ i+\frac{1}{2},j} \quad \text{and} \quad \eta_{z\ i,j+\frac{1}{2}} = \frac{1}{6} - \frac{1}{6}\epsilon^2_{z\ i,j+\frac{1}{2}} \tag{B.13}$$

A *clipping factor*, C is used to limit the antidiffusive flux, so that the scheme does not produce any local maxima or minima in the solution. The limited antidiffusive flux is then given as,

$$\begin{aligned} F^C_{i+\frac{1}{2},j} &= C_{i+\frac{1}{2},j} F^A_{i+\frac{1}{2},j} \qquad 0 \leq C_{i+\frac{1}{2},j} \leq 1 \\ G^C_{i,j-\frac{1}{2}} &= C_{i,j-\frac{1}{2}} G^A_{i,j-\frac{1}{2}} \qquad 0 \leq C_{i,j-\frac{1}{2}} \leq 1 \end{aligned}$$

The clipping factor C is computed according to the algorithm described in Zalesak (1979) The final solution is calculated from the limited antidiffusive fluxes, F^C and G^C as,

$$U^{n+1}_{i,j} = \tilde{U}^n_{i,j} - \frac{\Delta t}{\Delta x} \left[F^C_{i+\frac{1}{2},j} - F^C_{i-\frac{1}{2},j} \right] - \frac{\Delta t}{\Delta z} \left[G^C_{i,j+\frac{1}{2}} - G^C_{i,j-\frac{1}{2}} \right] + S\,\Delta t. \tag{B.14}$$

Appendix C

Description of the Movies

The movie files[†] of the simulation described in Chapters 3, 4 and 5 are located in `movies/` folder in the accompanying CD-ROM. The movies are produced from sequence of images which shows the physical quantity at each instant of time. Temperature perturbations, velocities and the energy fluxes are shown on a grid that spans the entire horizontal and vertical domain. The colours are linearly (logarithmically in the case of energy fluxes) scaled between minimum and maximum values with the adjacent colour-bar showing the colour map used. The thin black curves are the magnetic field lines and the white curve (black curve in the case of energy fluxes) represents the contour of $\beta = 1$. The number at the top right corner displays the elapsed time in seconds. The full list of movies available are described below.

Potential field case

Given below are a list of movies that show various quantities in a potential field configuration after initiation of a periodic horizontal motion of the lower boundary with an amplitude of 750 m s^{-1} and a period of P=24 s. The velocity field is represented by arrows.

a) `Movie-3.01a_Potential_dT.avi` : Temperature perturbations (ΔT).
b) `Movie-3.01b_Potential_dT.avi` : ΔT and velocity field.
c) `Movie-3.02_Potential_Vs.avi` : field aligned component of velocity.
d) `Movie-3.03_Potential_Vn.avi` : normal component of velocity.
e) `Movie-4.13_Potential_Acoustic.avi` : Acoustic fluxes.
f) `Movie-4.14_Potential_Poynting.avi` : Poynting fluxes.

Magnetohydrostatic flux tube: Moderate field case

The following list of movies are for a magnetohydrostatic flux sheet of moderate field

---

[†] **Note on formats:** The movies are encoded using MJPEG codec. Unix/Mac users will be able to view it on MPlayer (on Unix) and Quicktime (Mac) and Windows users can view it on Windows Media Player without any additional codec. A higher quality version of the movies, encoded using LJPEG codec, are located in `movies/high` folder.

strength after the initiation of a impulsive excitation in the lower boundary with an amplitude of 750 m s^{-1} and a period of P=24 s.

a) `Movie-3.04a_Moderate_dT.avi` : ΔT
b) `Movie-3.04b_Moderate_dT.avi` : ΔT and velocity field
c) `Movie-3.05_Moderate_Vs.avi` : Field aligned component of velocity
d) `Movie-3.06_Moderate_Vn.avi` : Perpendicular component of velocity
e) `Movie-4.15_Moderate_Acoustic.avi` : Acoustic fluxes
f) `Movie-4.16_Moderate_Poynting.avi` : Poynting fluxes

Magnetohydrostatic flux tube: Strong field case

The following list are for a magnetohydrostatic flux sheet of strong field strength after the initiation of a impulsive excitation in the lower boundary with an amplitude of 750 m s^{-1} and a period of P=24 s.

a) `Movie-3.07a_Strong_dT.avi` : ΔT
b) `Movie-3.07b_Strong_dT.avi` : ΔT and velocity field
c) `Movie-3.08_Strong_Vs.avi` : Parallel component of velocity
d) `Movie-3.09_Strong_Vn.avi` : Perpendicular component of velocity
e) `Movie-4.17_Strong_Acoustic.avi` : Acoustic fluxes
f) `Movie-4.18_Strong_Poynting.avi` : Poynting fluxes

Horizontal excitation with two pulses:

The following movie shows the temperature perturbations in a magnetohydrostatic flux sheet of strong field strength after the initiation of a horizontal displacement of the bottom boundary for a duration of two periods (V_{max}=750 m s^{-1} and P=24 s) after which the motion is stopped.

a) `Movie-3.10_Two_pulses_dT.avi` : ΔT

Horizontal excitation over a wider range:

The following movies show the temperature perturbations of a flux sheet with strong field strength after the initiation of a horizontal excitation over a height of 150 km (Narrow case) and 300 km (wide case).

a) `Movie-3.11a_Narrow_dT.avi` : ΔT
b) `Movie-3.11b_Narrow_dT.avi` : ΔT and velocity field
c) `Movie-3.12a_Wide_dT.avi` : ΔT
d) `Movie-3.12b_Wide_dT.avi` : ΔT and velocity field

Stokes analysis: Moderate field case

The following movies shows the evolution of Stokes *V* profiles of four Fe I emerging from a LOS situated on the left and right side of a flux sheet with moderate field strength after the initiation of horizontal impulsive excitation in the bottom layer with an amplitude of 5 km s^{-1} and a period of P=24 s. The elapsed time is displayed on the top right side. The amplitude asymmetry (δa) and area asymmetry (δA) at each instant is given on the top left side.

a) `Movie-5.19a_Moderate_5250_Left.avi` : Fe I 5250.2 Å on the left side
b) `Movie-5.19b_Moderate_5247_Left.avi` : Fe I 5247.06 Å ”
c) `Movie-5.19c_Moderate_6301_Left.avi` : Fe I 6301.5 Å ”
d) `Movie-5.19d_Moderate_6302_Left.avi` : Fe I 6302.5 Å ”
e) `Movie-5.20a_Moderate_5250_Right.avi` : Fe I λ 5250.2 Å on the right side
f) `Movie-5.20b_Moderate_5247_Right.avi` : Fe I 5247.06 Å ”
g) `Movie-5.20c_Moderate_6301_Right.avi` : Fe I 6301.5 Å ”
h) `Movie-5.20d_Moderate_6302_Right.avi` : Fe I 6302.5 Å ”
i) `Movie-5.21_Moderate_dT.avi` : ΔT

Stokes analysis: Strong field case:

Shows the evolution of Evolution of Stokes V profiles of four Fe I emerging from a LOS situated on the left and right side of a flux sheet with strong field strength after the initiation of horizontal impulsive excitation in the bottom layer.

a) `Movie-5.22a_Strong_5250_Left.avi` : Fe I 5250.2 Å on the left side
b) `Movie-5.22b_Strong_5247_Left.avi` : Fe I 5247.06 Å ”
c) `Movie-5.22c_Strong_6301_Left.avi` : Fe I 6301.5 Å ”
d) `Movie-5.22d_Strong_6302_Left.avi` : Fe I 6302.5 Å ”
e) `Movie-5.23a_Strong_5250_Right.avi` : Fe I 5250.2 Å on the right side
f) `Movie-5.23b_Strong_5247_Right.avi` : Fe I 5247.06 Å ”
g) `Movie-5.23c_Strong_6301_Right.avi` : Fe I 6301.5 Å ”
h) `Movie-5.23d_Strong_6302_Right.avi` : Fe I 6302.5 Å ”
i) `Movie-5.24_Strong_dT.avi` : ΔT

REFERENCES

Ahmad, Q. R., Allen, R. C., Andersen, T. C., et al. 2002, Direct evidence for neutrino flavor transformation from neutral-current interactions in the Sudbury neutrino observatory, Physical Review Letters, 89

Alfvén, H. 1947, Magneto hydrodynamic waves, and the heatinhg of the solar corona, MNRAS, 107, 211

Alfven, H. 1950, Cosmical electrodynamics

Auer, L. H. & Heasley, J. N. 1978, The origin of broad-band circular polarization in sunspots, A&A, 64, 67

Babcock, H. W. & Babcock, H. D. 1958, Photospheric magnetic fields, in IAU Symposium, Vol. 6, Electromagnetic Phenomena in Cosmical Physics, ed. B. Lehnert, 239

Bahcall, J. N., Gonzalez-Garcia, M. C., & Peña-Garay, C. 2003, Does the Sun shine by pp or CNO fusion reactions?, Physical Review Letters, 90

Bellot Rubio, L. R., Rodríguez Hidalgo, I., Collados, M., Khomenko, E., & Ruiz Cobo, B. 2001, Observation of convective collapse and upward-moving shocks in the quiet sun, ApJ, 560, 1010

Berger, T. E., Rouppe van der Voort, L. H. M., Löfdahl, M. G., et al. 2004, Solar magnetic elements at 0.1 arcsec resolution. General appearance and magnetic structure, A&A, 428, 613

Berger, T. E. & Title, A. M. 1996, On the dynamics of small-scale solar magnetic elements, ApJ, 463, 365

Berger, T. E. & Title, A. M. 2001, On the relation of G-Band bright points to the photospheric magnetic field, ApJ, 553, 449

Biermann, L. 1948, Über die Ursache der chromosphärischen Turbulenz und des UV-Exzesses der Sonnenstrahlung, Zeitschrift fur Astrophysik, 25, 161

Bogdan, T. J., Carlsson, M., Hansteen, V. H., et al. 2003, Waves in the magnetized solar atmosphere. II. Waves from localized sources in magnetic flux concentrations, ApJ, 599, 626

Boris, J. 1971, A Fluid Transport Algorithm that Works., Technical reports of Naval Research Lab

Boris, J. 1976, Flux-Corrected Transport Modules for Solving Generalized Continuity Equations., Meth. Comput. Phys., 16, 85

Boris, J. & Book, D. 1976, Solution of continuity equations by the method of flux-corrected transport

Bray, R. J. & Loughhead, R. E. 1974, The solar chromosphere (The International Astrophysics Series, London: Chapman and Hall, 1974)

Cally, P. S. 2005, Local magnetohelioseismology of active regions, MNRAS, 358, 353

Cally, P. S. 2007, What to look for in the seismology of solar active regions, Astronomische Nachrichten, 328, 286

Carlsson, M. & Stein, R. F. 1997, Formation of solar Calcium H and K bright grains, ApJ, 481, 500

Carlsson, M. & Stein, R. F. 2002, Wave processes in the solar upper atmosphere, in ESA Special Publication, Vol. 505, SOLMAG 2002. Proceedings of the Magnetic Coupling of the Solar Atmosphere Euroconference, ed. H. Sawaya-Lacoste, 293–300

Charbonneau, P., Christensen-Dalsgaard, J., Henning, R., et al. 1999, Helioseismic constraints on the structure of the solar tachocline, ApJ, 527, 445

Cheung, M. C. M., Schüssler, M., & Moreno-Insertis, F. 2007, Magnetic flux emergence in granular convection: radiative MHD simulations and observational signatures, A&A, 467, 703

Couvidat, S., García, R. A., Turck-Chièze, S., et al. 2003, The rotation of the deep solar ayers, ApJ, 597, L77

Cranmer, S. R. & van Ballegooijen, A. A. 2005, On the generation, propagation, and reflection of Alfvén waves from the solar photosphere to the distant heliosphere, ApJS, 156, 265

Danilovic, S., Schüssler, M., & Solanki, S. K. 2009, Magnetic field intensification: comparison of 3D MHD simulations with Hinode/SP results, ArXiv e-prints

De Pontieu, B., Hansteen, V. H., Rouppe van der Voort, L., van Noort, M., & Carlsson, M. 2007, High-Resolution observations and modeling of dynamic fibrils, ApJ, 655, 624

Defouw, R. J. 1976, Wave propagation along a magnetic tube, ApJ, 209, 266

Devore, C. R. 1991, Flux-corrected transport techniques for multidimensional compressible magnetohydrodynamics, Journal of Computational Physics, 92, 142

Dikpati, M. & Gilman, P. A. 2009, Flux-transport solar dynamos, Space Science Reviews, 144, 67

Dunn, R. B. & Zirker, J. B. 1973, The Solar Filigree, Sol. Phys., 33, 281

Ferriz-Mas, A., Schuessler, M., & Anton, V. 1989, Dynamics of magnetic flux concentrations - The second-order thin flux tube approximation, A&A, 210, 425

Finsterle, W., Jefferies, S. M., Cacciani, A., Rapex, P., & McIntosh, S. W. 2004, Helioseismic mapping of the magnetic canopy in the solar chromosphere, ApJ, 613, L185

Fischer, C. E., de Wijn, A. G., Centeno, R., Lites, B. W., & Keller, C. U. 2009, Statistics of convective collapse events in the photosphere and chromosphere observed with the Hinode SOT, A&A, 504, 583

Fossum, A. & Carlsson, M. 2005, High-frequency acoustic waves are not sufficient to heat the solar chromosphere, Nature, 435, 919

Gadun, A. S., Solanki, S. K., Sheminova, V. A., & Ploner, S. R. O. 2001, A formation mechanism of magnetic elements in regions of mixed polarity, Sol. Phys., 203, 1

Gaizauskas, V. 1985, Observations of the fine structure of the chromosphere, in Chromospheric Diagnostics and Modelling, ed. B. W. Lites, 25–49

Galloway, D. J. & Proctor, M. R. E. 1983, The kinematics of hexagonal magnetoconvection, Geophysical and Astrophysical Fluid Dynamics, 24, 109

Galloway, D. J., Proctor, M. R. E., & Weiss, N. O. 1977, Formation of intense magnetic fields near the surface of the sun, Nature, 266, 686

Galloway, D. J. & Weiss, N. O. 1981, Convection and magnetic fields in stars, ApJ, 243, 945

Grossmann-Doerth, U. 1994, Height of formation of solar photospheric spectral lines, A&A, 285, 1012

Grossmann-Doerth, U., Keller, C. U., & Schuessler, M. 1996, Observations of the quiet Sun's magnetic field., A&A, 315, 610

Grossmann-Doerth, U., Larsson, B., & Solanki, S. K. 1988a, Contribution and response functions for Stokes line profiles formed in a magnetic field, A&A, 204, 266

Grossmann-Doerth, U., Schuessler, M., & Solanki, S. K. 1988b, Unshifted, asymmetric Stokes V-profiles - Possible solution of a riddle, A&A, 206, L37

Grossmann-Doerth, U., Schuessler, M., & Solanki, S. K. 1989, Stokes V asymmetry and shift of spectral lines, A&A, 221, 338

Grossmann-Doerth, U., Schuessler, M., & Steiner, O. 1998, Convective intensification of solar surface magnetic fields: results of numerical experiments, A&A, 337, 928

Gurtovenko, E., Ratnikova, V., & de Jager, C. 1974, On the average optical depth of formation of weak Fraunhofer lines, Sol. Phys., 37, 43

Hale, G. E. & Nicholson, S. B. 1938, Magnetic observations of sunspots, 1917-1924

Hansteen, V. H., De Pontieu, B., Rouppe van der Voort, L., van Noort, M., & Carlsson, M. 2006, Dynamic fibrils are driven by magnetoacoustic shocks, ApJ, 647, L73

Hasan, S. S. 1983, Time-dependent convective collapse of flux tubes, in IAU Symposium, Vol. 102, Solar and Stellar Magnetic Fields: Origins and Coronal Effects, ed. J. O. Stenflo, 73–76

Hasan, S. S. 1984a, Convective collapse and overstable oscillations in solar flux tubes, in ESA Special Publication, Vol. 220, ESA Special Publication, ed. T. D. Guyenne & J. J. Hunt, 227–228

Hasan, S. S. 1984b, Convective instability in a solar flux tube. I - Nonlinear calculations for an adiabatic inviscid fluid, ApJ, 285, 851

Hasan, S. S. 1985, Convective instability in a solar flux tube. II - Nonlinear calculations with horizontal radiative heat transport and finite viscosity, A&A, 143, 39

Hasan, S. S. 1986, Oscillatory motions in intense flux tubes, MNRAS, 219, 357

Hasan, S. S. 1988, Energy transport in intense flux tubes on the sun. I - Equilibrium atmosphere, ApJ, 332, 499

Hasan, S. S. & Kalkofen, W. 1999, Excitation of oscillations in photospheric flux tubes through buffeting by external granules, ApJ, 519, 899

Hasan, S. S., Kalkofen, W., & van Ballegooijen, A. A. 2000, Excitation of oscillations in the magnetic network on the Sun, ApJ, 535, L67

Hasan, S. S., Kalkofen, W., van Ballegooijen, A. A., & Ulmschneider, P. 2003, Kink and longitudinal oscillations in the magnetic network on the Sun: Nonlinear effects and mode transformation, ApJ, 585, 1138

Hasan, S. S. & van Ballegooijen, A. A. 2008, Dynamics of the solar magnetic network. II. Heating the magnetized chromosphere, ApJ, 680, 1542

Hasan, S. S., van Ballegooijen, A. A., Kalkofen, W., & Steiner, O. 2005, Dynamics of the solar magnetic network: Two-dimensional MHD simulations, ApJ, 631, 1270

Hasan, S. S., Vigeesh, G., & van Ballegooijen, A. A. 2006, Wave propagation in the magnetic network on the sun, in IAU Symposium, Vol. 233, Solar Activity and its Magnetic Origin, ed. V. Bothmer & A. A. Hady, 116–117

Howard, R. 1959, Observations of solar magnitic fields., ApJ, 130, 193

Howe, R. 2009, Solar interior rotation and its variation, Living Reviews in Solar Physics, 6, 1

Hurlburt, N. E., Toomre, J., & Massaguer, J. M. 1984, Two-dimensional compressible convection extending over multiple scale heights, ApJ, 282, 557

Jefferies, S. M., McIntosh, S. W., Armstrong, J. D., et al. 2006, Magnetoacoustic portals and the basal heating of the solar chromosphere, ApJ, 648, L151

Judge, P. G., Carlsson, M., & Stein, R. F. 2003, On the origin of the basal emission from stellar atmospheres: Analysis of solar C II Lines, ApJ, 597, 1158

Khomenko, E. & Collados, M. 2007, On the Stokes V amplitude ratio as an indicator of the field strength in the solar internetwork, ApJ, 659, 1726

Khomenko, E., Collados, M., & Felipe, T. 2008, Nonlinear numerical simulations of magneto-acoustic wave propagation in small-scale flux tubes, Sol. Phys., 251, 589

Kulsrud, R. M. 1955, Effect of magnetic fields on generation of noise by isotropic turbulence., ApJ, 121, 461

Landi Degl'Innocenti, E. & Landi Degl'Innocenti, M. 1977, Response functions for magnetic lines, A&A, 56, 111

Leighton, R. B. 1959, Observations of solar magnetic fields in plage regions., ApJ, 130, 366

Leighton, R. B., Noyes, R. W., & Simon, G. W. 1962, Velocity fields in the solar atmosphere. I. Preliminary report., ApJ, 135, 474

Lighthill, M. F. 1967, Predictions on the velocity field coming from acoustic noise and a generalized turbulence in a layer overlying a convectively unstable atmospheric region, in IAU Symposium, Vol. 28, Aerodynamic Phenomena in Stellar Atmospheres, ed. R. N. Thomas, 429

Lighthill, M. J. 1952, On sound generated aerodynamically. I. General theory, Royal Society of London Proceedings Series A, 211, 564

Lites, B. W., Kubo, M., Socas-Navarro, H., et al. 2008, The horizontal magnetic flux of the quiet-sun internetwork as observed with the Hinode spectro-polarimeter, ApJ, 672, 1237

Magain, P. 1986, Contribution functions and the depths of formation of spectral lines, A&A, 163, 135

Meyer, F., Schmidt, H. U., Simon, G. W., & Weiss, N. O. 1979, Buoyant magnetic flux tubes in supergranules, A&A, 76, 35

Michalitsanos, A. G. 1973, The five minute period oscillation in magnetically active regions, Sol. Phys., 30, 47

Muller, R. 1983, The dynamical behavior of facular points in the quiet photosphere, Sol. Phys., 85, 113

Muller, R. 1985, The fine structure of the quiet sun, Sol. Phys., 100, 237

Muller, R., Hulot, J. C., & Roudier, T. 1989, Perturbation of the granular pattern by the presence of magnetic flux tubes, Sol. Phys., 119, 229

Musielak, Z. E., Rosner, R., Stein, R. F., & Ulmschneider, P. 1994, On sound generation by turbulent convection: A new look at old results, ApJ, 423, 474

Musman, S. & Rust, D. M. 1970, Vertical velocities and horizontal wave propagation in the solar photosphere, Sol. Phys., 13, 261

Nagata, S., Tsuneta, S., Suematsu, Y., et al. 2008, Formation of solar magnetic flux tubes with kilogauss field strength induced by convective instability, ApJ, 677, L145

Narain, U. & Ulmschneider, P. 1990, Chromospheric and coronal heating mechanisms, Space Science Reviews, 54, 377

Narain, U. & Ulmschneider, P. 1996, Chromospheric and coronal heating mechanisms II, Space Science Reviews, 75, 453

Nave, G., Johansson, S., Learner, R. C. M., Thorne, A. P., & Brault, J. W. 1994, A new multiplet table for Fe I, ApJS, 94, 221

Nisenson, P., van Ballegooijen, A. A., de Wijn, A. G., & Sütterlin, P. 2003, Motions of isolated *G*-Band bright points in the solar photosphere, ApJ, 587, 458

Nordlund, A. 1983, Numerical 3-D simulations of the collapse of photospheric flux tubes, in IAU Symposium, Vol. 102, Solar and Stellar Magnetic Fields: Origins and Coronal Effects, ed. J. O. Stenflo, 79–83

Nordlund, . 1986, 3-D Model calculations, in Small Scale Magnetic Flux Concentrations in the Solar Photosphere, ed. W. Deinzer, M. Knölker, & H. H. Voigt, 83

Nordlund, . & Stein, R. F. 1989, Simulating magnetoconvection, in NATO ASIC Proc. 263: Solar and Stellar Granulation, ed. R. J. Rutten & G. Severino, 453

Oran, E. S. & Boris, J. P. 1987, Numerical simulation of reactive flow, NASA STI/Recon Technical Report A, 88, 44860

Osterbrock, D. E. 1961, The heating of the solar chromosphere, plages, and corona by magnetohydrodynamic waves., ApJ, 134, 347

Parker, E. N. 1963, Kinematical hydromagnetic theory and its application to the low solar photosphere., ApJ, 138, 552

Parker, E. N. 1964, A mechanism for magnetic enhancement of sound-wave generation and the dynamical origin of spicules., ApJ, 140, 1170

Parker, E. N. 1978, Hydraulic concentration of magnetic fields in the solar photosphere. VI - Adiabatic cooling and concentration in downdrafts, ApJ, 221, 368

Pietarila, A., Socas-Navarro, H., Bogdan, T., Carlsson, M., & Stein, R. F. 2006, Simulation of quiet-sun waves in the Ca II infrared triplet, ApJ, 640, 1142

Pizzo, V. J. 1986, Numerical solution of the magnetostatic equations for thick flux tubes, with application to sunspots, pores, and related structures, ApJ, 302, 785

Priest, E. R. 1982

Proctor, M. R. E. & Weiss, N. O. 1982, Magnetoconvection, Reports on Progress in Physics, 45, 1317

Rachkovsky, D. 1962, Magneto-optical effects in spectral lines of sunspots, Izv. Krymsk. Astrofiz. Observ, 27, 148

Rajaguru, S. P. & Hasan, S. S. 2000, Radiative transfer effects and the dynamics of small-scale magnetic structures on the sun, ApJ, 544, 522

Roberts, B. & Webb, A. R. 1978, Vertical motions in an intense magnetic flux tube, Sol. Phys., 56, 5

Roberts, W. O. 1945, A preliminary report on chromospheric spicules of extremely short lifetime., ApJ, 101, 136

Rosenthal, C. S., Bogdan, T. J., Carlsson, M., et al. 2002, Waves in the magnetized solar atmosphere. I. Basic processes and internetwork oscillations, ApJ, 564, 508

Rutten, R. J. & Uitenbroek, H. 1991, CA II H(2v) and K(2v) cell grains, Sol. Phys., 134, 15

Schaffenberger, W., Wedemeyer-Böhm, S., Steiner, O., & Freytag, B. 2005, Magnetohydrodynamic simulation from the convection zone to the chromosphere, in ESA Special Publication, Vol. 596, Chromospheric and Coronal Magnetic Fields, ed. D. E. Innes, A. Lagg, & S. A. Solanki

Schrijver, C. J. 1995, Basal heating in the atmospheres of cool stars, A&A Rev., 6, 181

Schwarzschild, M. 1948, On noise arising from the solar granulation., ApJ, 107, 1

Sheeley, Jr., N. R. 1966, Measurements of solar magnetic fields, ApJ, 144, 723

Sheeley, Jr., N. R. 1967, Observations of small-scale solar magnetic fields, Sol. Phys., 1, 171

Sheminova, V. A. & Gadun, A. S. 2000, Evolution of Solar Magnetic Tubes from Observations of Stokes Parameters, Astronomy Reports, 44, 701

Sigwarth, M. 2000, Dynamics of solar magnetic fields – A spectroscopic investigation, in Reviews in Modern Astronomy, Vol. 13, Reviews in Modern Astronomy, ed. R. E. Schielicke, 45

Sigwarth, M., Balasubramaniam, K. S., Knölker, M., & Schmidt, W. 1999, Dynamics of solar magnetic elements, A&A, 349, 941

Simon, G. W., Weiss, N. O., & Nye, A. H. 1983, Simple models for magnetic flux tubes, Sol. Phys., 87, 65

Socas-Navarro, H., Borrero, J. M., Asensio Ramos, A., et al. 2008, Multiline spectropolarimetry of the quiet Sun at 5250 and 6302 , ApJ, 674, 596

Solanki, S. K. 1993, Smallscale solar magnetic fields - an overview, Space Science Reviews, 63, 1

Solanki, S. K. & Pahlke, K. D. 1988, Can stationary velocity fields explain the Stokes V asymmetry observed in solar magnetic elements?, A&A, 201, 143

Solanki, S. K. & Stenflo, J. O. 1984, Properties of solar magnetic fluxtubes as revealed by Fe I lines, A&A, 140, 185

Spiegel, E. A. & Zahn, J. 1992, The solar tachocline, A&A, 265, 106

Spruit, H. C. & Zweibel, E. G. 1979, Convective instability of thin flux tubes, Sol. Phys., 62, 15

Staude, J. 1972, On the mean depth of line formation in a magnetic field, Sol. Phys., 24, 255

Stein, R. F. 1967, Generation of acoustic and gravity waves by turbulence in an isothermal stratified atmosphere, Sol. Phys., 2, 385

Stein, R. F. 1968, Waves in the solar atmosphere. I. The acoustic energy flux., ApJ, 154, 297

Stein, R. F. & Leibacher, J. 1974, Waves in the solar atmosphere, ARA&A, 12, 407

Steiner, O. 1999, Flux Tube Dynamics, in Astronomical Society of the Pacific Conference Series, Vol. 184, Third Advances in Solar Physics Euroconference: Magnetic Fields and Oscillations, ed. B. Schmieder, A. Hofmann, & J. Staude, 38–54

Steiner, O. 2000, The formation of asymmetric Stokes V profiles in the presence of a magnetopause, Sol. Phys., 196, 245

Steiner, O., Grossmann-Doerth, U., Knoelker, M., & Schuessler, M. 1998, Dynamical interaction of solar magnetic elements and granular convection: Results of a numerical simulation, ApJ, 495, 468

Steiner, O., Knölker, M., & Schüssler, M. 1994, Dynamic interaction of convection with magnetic flux sheets: first results of a new MHD code, in Solar Surface Magnetism, ed. R. J. Rutten & C. J. Schrijver, 441

Steiner, O. & Pizzo, V. J. 1989, A parametric survey of model solar fluxtubes, A&A, 211, 447

Steiner, O., Pneuman, G. W., & Stenflo, J. O. 1986, Numerical models for solar magnetic fluxtubes, A&A, 170, 126

Steiner, O., Vigeesh, G., Krieger, L., et al. 2007, First local helioseismic experiments with CO^{5}BOLD, Astronomische Nachrichten, 328, 323

Stenflo, J. O. 1973, Magnetic-field structure of the photospheric network, Sol. Phys., 32, 41

Stenflo, J. O. 1994, Solar magnetic fields: Polarized radiation diagnostics

Stenflo, J. O. & Harvey, J. W. 1985, Dependence of the properties of magnetic fluxtubes on area factor or amount of flux, Sol. Phys., 95, 99

Stenflo, J. O., Solanki, S., Harvey, J. W., & Brault, J. W. 1984, Diagnostics of solar magnetic fluxtubes using a Fourier transform spectrometer, A&A, 131, 333

Suematsu, Y. 1990, Influence of photospheric 5-minute oscillations on the formation of chromospheric fine structures, in Lecture Notes in Physics, Berlin Springer Verlag, Vol. 367, Progress of Seismology of the Sun and Stars, ed. Y. Osaki & H. Shibahashi, 211–214

Takeuchi, A. 1993, The nonlinear evolution of a convective instability in a solar magnetic flux tube, PASJ, 45, 811

Takeuchi, A. 1995, On the convective stability of solar photospheric flux tubes, PASJ, 47, 331

Thomas, R. N. 1948, Superthermic phenomena in stellar atmospheres. I. Spicules and the solar chromosphere., ApJ, 108, 130

Title, A. M., Tarbell, T. D., & Topka, K. P. 1987, On the relation between magnetic field structures and granulation, ApJ, 317, 892

Tritschler, A., Schmidt, W., Uitenbroek, H., & Wedemeyer-Böhm, S. 2007, On the fine structure of the quiet solar Ca II K atmosphere, A&A, 462, 303

Tsuneta, S., Ichimoto, K., Katsukawa, Y., et al. 2008, The Solar Optical Telescope for the hinode mission: An overview, Sol. Phys., 249, 167

Ulmschneider, P., Rammacher, W., Musielak, Z. E., & Kalkofen, W. 2005, On the validity of acoustically heated chromosphere models, ApJ, 631, L155

Unno, W. 1956, Line formation of a normal Zeeman triplet, PASJ, 8, 108

Unno, W. & Ando, H. 1979, Instability of a thin magnetic tube in the solar atmosphere, Geophysical and Astrophysical Fluid Dynamics, 12, 107

Venkatakrishnan, P. 1983, Nonlinear development of convective instability within slender flux tubes. I - Adiabatic flow, Journal of Astrophysics and Astronomy, 4, 135

Vernazza, J. E., Avrett, E. H., & Loeser, R. 1981, Structure of the solar chromosphere. III - Models of the EUV brightness components of the quiet-sun, ApJS, 45, 635

Vigeesh, G., Hasan, S. S., & Steiner, O. 2009, Wave propagation and energy transport in the magnetic network of the Sun, A&A, 508, 951

Vögler, A., Shelyag, S., Schüssler, M., et al. 2005, Simulations of magneto-convection in the solar photosphere. Equations, methods, and results of the MURaM code, A&A, 429, 335

Webb, A. R. & Roberts, B. 1978, Vertical motions in an intense magnetic flux tube. II - Convective instability, Sol. Phys., 59, 249

Webb, A. R. & Roberts, B. 1980a, Vertical motions in an intense magnetic flux tube - Part Five - Radiative relaxation in a stratified medium, Sol. Phys., 68, 87

Webb, A. R. & Roberts, B. 1980b, Vertical motions in an intense magnetic flux tube. IV - Radiative relaxation in a uniform medium., Sol. Phys., 68, 71

Wedemeyer-Böhm, S., Lagg, A., & Nordlund, . 2009, Coupling from the photosphere to the chromosphere and the corona, Space Science Reviews, 144, 317

Wittmann, A. 1974, Computation and observation of Zeeman multiplet polarization in Fraunhofer lines. II: computation of Stokes parameter profiles, Sol. Phys., 35, 11

Zalesak, S. 1979, Fully multidimensional flux-corrected transport algorithms for fluids, Journal of Computational Physics, 31, 335

Zwaan, C. 1987, Elements and patterns in the solar magnetic field, ARA&A, 25, 83